NMR Study
in
the Low-Dimensional Quantum Spin System

January 1998

Shinji MATSUMOTO

OSAKA UNIVERSITY
GRADUATE SCHOOL OF ENGINEERING SCIENCE
DEPARTMENT OF PHYSICAL SCIENCE
DIVISION OF MATERIALS PHYSICS

A B S T R A C T

NMR/NQR measurements on hole-doped two-leg spin-ladder compounds of $LaCuO_{2.5}$ and $Sr_{14}Cu_{24}O_{41}$ have been performed in order to clarify the magnetic properties and the effects of the carrier-doping. Cu NMR experiments have revealed that the ground state of $LaCuO_{2.5}$ is not in the spin liquid state with a spin gap in disagreement with the suggestion from the susceptibility measurement. Alternatively, it has been shown that a magnetic ordering takes place below T_N ~110 K. The magnetic interaction among the ladders in $LaCuO_{2.5}$, which is not frustrated, has been pointed out to lead to the magnetically ordered state. On the other hand, comprehensive Cu NMR/NQR measurements have been performed on the single crystals of $Sr_{14}Cu_{24}O_{41}$ and $Sr_{13.75}Y_{0.25}Cu_{24}O_{41}$ containing CuO_2 chain and Cu_2O_3 two-leg ladder by separating the Cu NMR/NQR spectra between the Cu chain and ladder sites. In these compounds, that holes are inherently doped plays an important role to disturb the quantum coherence in the singlet ground state in the two-leg ladder. In the two-leg spin-ladder, there exists a spin gap of about 500K which is larger than in $SrCu_2O_3$. It has been found that the magnetic field induces a staggered magnetization(SM) in $Sr_{14}Cu_{24}O_{41}$ below ~100K. The origin of the staggered moments is suggested to be attributed to unpaired holes. A striking finding in this work is that the size of the SM is not largely distributed as in Zn doping which acts as a spin defect. We have proposed that an extended character of unpaired hole-state and/or collective charge excitations turn out spin defects. Spin defects are supposed to extend in the ladder and SM induced by magnetic field are averaged out with rather uniform size of SM. It was uncovered that the quantum coherence in the singlet ground states in the two-leg spin-ladder system is dramatically perturbed by the presence of either localized or extended holes and by switching on the inter-ladder interaction. NMR/NQR measurements revealed the existence of the spin gap of 100~140K in the CuO_2 which had been suggested by the magnetic susceptibility measurement. The unique dimerization model in the CuO_2 chain with nearly 90° Cu-O-Cu bond angle has been proposed in this work.

Contents

Chapter 1

GENERAL INTRODUCTION

1.1 Theoretical Predictions

The discovery of copper-oxide high-T_c superconductors [1] has aroused much interest in the low dimensional S=1/2 antiferromagnetic(AF) system since the superconductivity is considered to occur in the lightly hole-doped two dimensional (2D) square lattice of CuO_2 plane. A square lattice has a magnetically ordered ground state and a true long-range order is destroyed by doping holes slightly. In the one dimensional(1D) S=1/2 AF Heisenberg chain, the quantum effects overwhelm the long-range order but the ground state shows the long-range Resonating Valence Bonding(RVB [2]) state with an inverse power-law decay in the spin-spin correlation function. What happens in the intermediate system between 1D and 2D systems ? An answer was first given by numerical calculations which found that the crossover from chain to square lattice was far from smooth [3, 4]. In such quasi-1D system that AF Heisenberg chains are coupled with one next to the other to form ladders of increasing width, ladders with an even number of chains have a spin liquid ground state because of their short-range spin correlation decayed exponentially and then a finite spin gap is produced with its magnitude reduced progressively with an increase of chains [4, 5, 6]. By contrast, ladders made from an odd number of chains display magnetic properties similar to a single chain, i.e. gapless spin excitation with a power-law decay of spin-spin correlations.

For AF Heisenberg exchange interactions between nearest-neighbor(nn) spins, the only case discussed here, the spin Hamiltonian of n-leg ladder is

$$\mathcal{H} = J\sum_{\langle i,j\rangle}\mathbf{S}_i\cdot\mathbf{S}_j + J'\sum_{\langle i,k\rangle}\mathbf{S}_i\cdot\mathbf{S}_k, \tag{1.1}$$

where $J, J' > 0$ for AF coupling [7]. The first sum is over distinct nn spin pairs in each chains and second is distinct nn spin pairs in adjacent chains. The spin exchange coupling constant is J within a leg and J' within a rung. The magnetic susceptibility, $\chi(T)$, calculated with Monte Carlo techniques on m-leg ladders with J=J' on clusters of $m\times 100$ sites [8] is shown in Fig.1.1.1(a). For even-leg ladders, $\chi(T)$ shows at low temperature the exponential suppression caused by spin gap, whereas the odd-leg ladders extrapolate to a finite value as $T\rightarrow 0$. It is found that the crossover from chains to square lattices is far from smooth. The spin gap Δ_{spin}, which is obtained numerically, for the two-leg ladder is plotted against J/J' in Fig.1.1.1(b) [8].

More interestingly, holes doped into ladders with even number chains are predicted to pair [3, 9] and possibly superconduct. A clear contrast between even and odd ladders is again predicted upon doping.

1.2 Experimental Results in the Even- and Odd-Leg Ladders

As a matter of fact, the presence of a spin gap was confirmed experimentally in such two-leg ladder compounds as $(VO)_2P_2O_7$ [10] and $SrCu_2O_3$ [1, 2]. By contrast, the three-leg ladder exhibited long-range development of the spin correlation upon lowering temperature and as a result the long-range order emerged around 60 K due to the weak interladder interaction and/or the interlayer coupling [3, 13].

Schematic drawings of ladder structures in $SrCu_2O_3$ and $Sr_2Cu_3O_5$ are shown in Fig.1.2.1 [1]. The solid circles indicate Cu^{2+} ions with a S=1/2 spin. O^{2-} ions exist at

the corners of the squares drawn with solid lines. Since Cu-O-Cu chains running along a-axis have a bond angle of 180°, Cu spins couple antiferromagnetically each other. Cu-O-Cu chains are coupled antiferromagnetically each other. Ladders are separated from each other because the inter-ladder interactions must be much weak due to the spin frustration [4].

The experimental results of the magnetic susceptibility, $\chi(T)$, in $SrCu_2O_3$ and $Sr_2Cu_3O_5$ showed excellent agreements with the theoretical predictions [1]. $\chi(T)$ in (a) $SrCu_2O_3$ and (b) $Sr_2Cu_3O_5$ are shown in Fig.1.2.2 [1]. The magnetic susceptibility after subtraction of the low-temperature Curie component from the raw data, χ_s, is indicated with solid circles. In the two-leg ladder compound of $SrCu_2O_3$, χ_s shows the exponential suppression at low temperature in consistent with the numerical calculated result. The spin gap, Δ, is estimated to be 420K [1]. Furthermore, in the three-leg ladder compound of $Sr_2Cu_3O_5$, χ_s settles down to a finite value as $T \rightarrow 0$K, while the magnetic order emerges around 60K.

1.3 Aim of This Study

Because of the difficulty of the carrier-doping, unfortunately, it has not succeeded yet in $(VO)_2P_2O_7$ and $SrCu_2O_3$. Two-leg spin-ladder $La_{1-x}Sr_xCuO_{2.5}$ and $Sr_{14}Cu_{24}O_{41}$ are possible to be hole-doped.

NMR/NQR measurements have been performed to clarify the magnetic properties and the effects of the carrier-doping.

REFERENCES

[1] J.G.Bednorz and K.A.Müller; Z.Phys.B **64** (1986) 188.

[2] P.W.Anderson; Science. **235** (1987) 1196.

[3] E.Dagotto, J.Riera and D.Scalpino; Phys.Rev.B **45** (1992) 5744.

[4] T.M.Rice, S.Gopalan and M.Siegrist; Europhys.Lett. **23** (1993) 445.

[5] R.M.Noack, SR.White and D.J.Scalpino; Phys.Rev.Lett. **73** (1994) 882.

[6] S.R.White, R.M.Noack and D.J.Scalpino; Phys.Rev.Lett. **73** (1994) 886.

[7] D.C.Jhonston; Phys.Rev.B **54** (1996) 13009.

[8] E.Dagotto and T.M.Rice; Science **271** (1996) 618.

[9] N.Sigrist, T.M.Rice and F.C.Zhang; Phys.Rev.B **49** (1994) 12058.

[10] R.S.Eccleston, T.Barnes, J.Brody and J.W.Johnson; Phys.Rev.Lett. **73** (1994) 2626.

[11] M.Azuma, Z.Hiroi, M.Takano, K.Ishida and Y.Kitaoka; Phys.Rev.Lett. **73** (1994) 3463.

[12] K.Ishida, Y.Kitaoka, K.Asayama, M.Azuma, Z.Hiroi and M.Takano;
J.Phys.Soc.Jpn. **63** (1994) 3222.

[13] K.Kojima, A.Keren, G.M.Luke, B.Nachumi, W.D.Wu, Y.J.Uemura, M.Azuma and M.Takano;
Phys.Rev.Lett. **74**(1994) 2812.

[14] K.Ishida, Y.Kitaoka, Y.Tokunaga, S.Matsumoto, K.Asayama, M.Azuma, Z.Hiroi and M.Takano;
Phys.Rev.B **53** (1996) 2827.

(a)

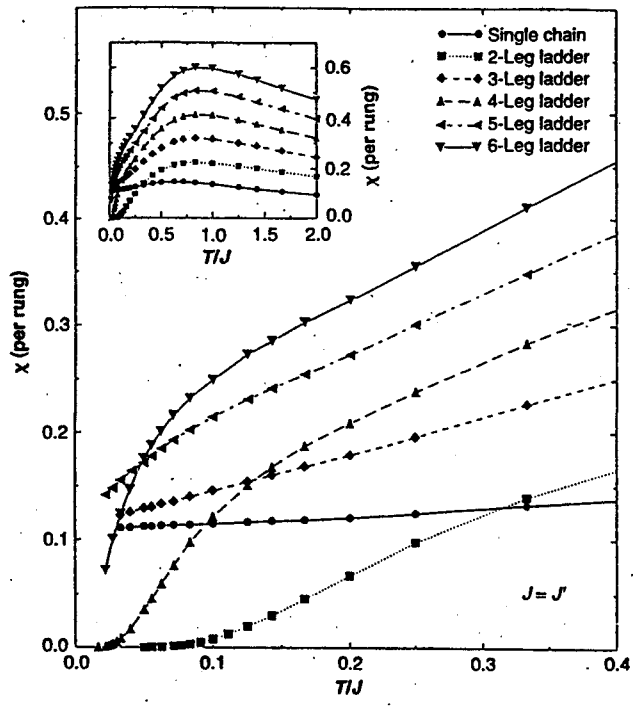

(b)

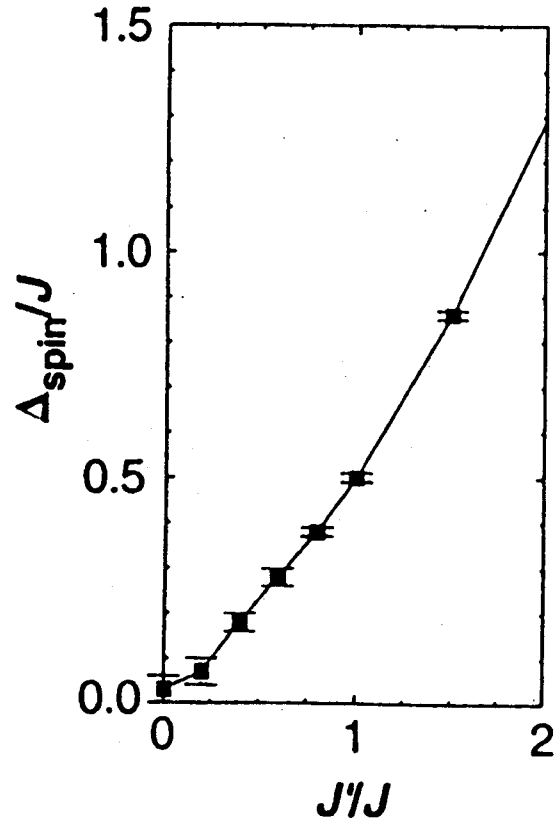

Fig.1.1.1 (a) The magnetic susceptibility, $\chi(T)$, calculated with Monte Carlo techniques on m-leg ladders with J=J'. (b) Spin gap versus J/J' for the two-leg ladder[8].

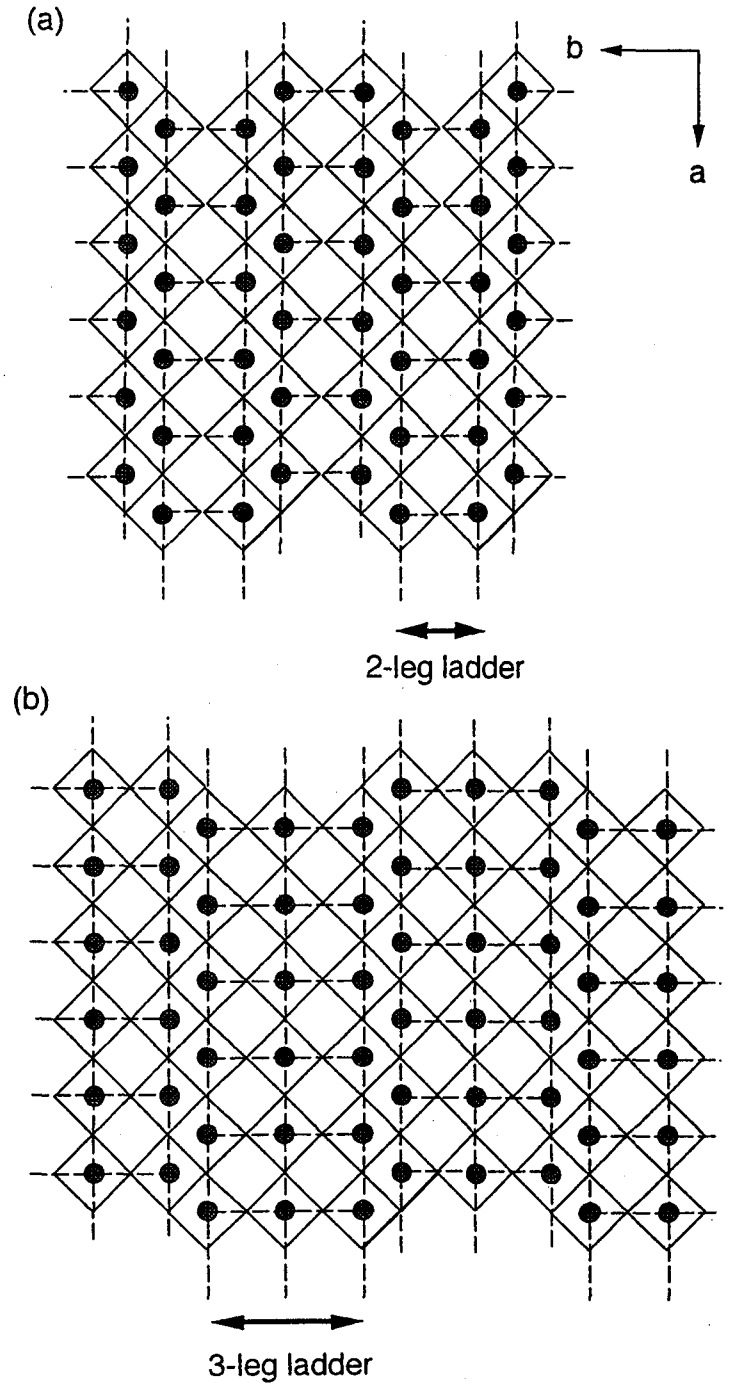

Fig.1.2.1 Schematic drawings of (a) $SrCu_2O_3$ with two-leg ladders and (b) $Sr_2Cu_3O_5$ with tree-leg ladders[11].

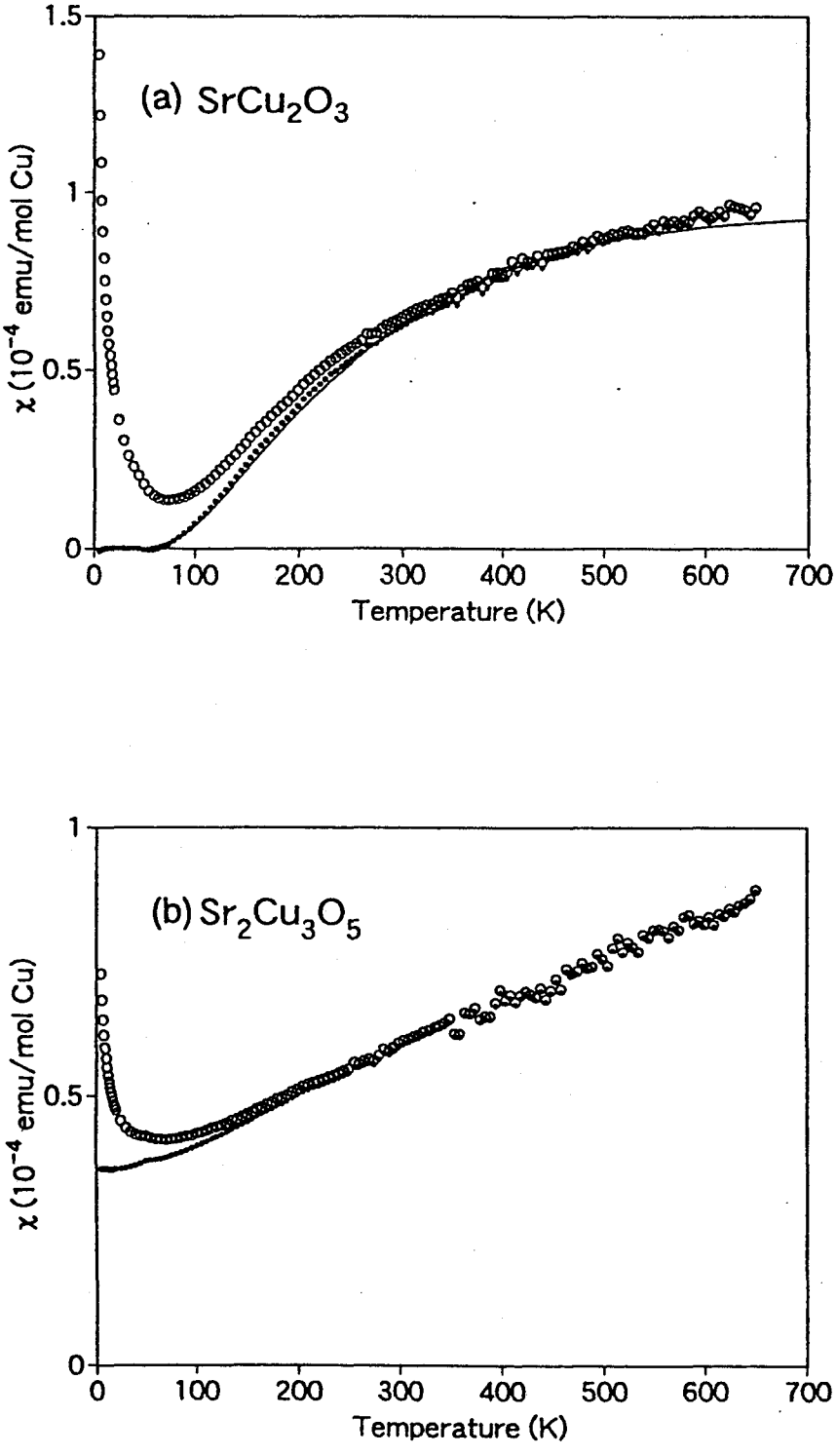

Fig.1.2.2 The experimental results of the magnetic susceptibility, $\chi(T)$, in (a) $SrCu_2O_3$ and (b) $Sr_2Cu_3O_5$[11]. Solid circles indicate the susceptibility after subtraction of the low-temperature Curie component from the raw data.

Chapter 2

NUCLEAR MAGNETIC RESONANCE

The experimental technique of Nuclear Magnetic Resonance(NMR) has made a great contribution to the progress of the solid state physics and chemistry. Especially, it is a powerful tool for the investigation on the magnetism. The purpose of this chapter is to introduce the important informations obtained from the NMR measurements and detail aspects.

2.1 Effective Nuclear Spin Hamiltonian

The Hamiltonian of a nuclear spin at the i-th sites, $\mathbf{I}^i$, can be written as [1, 2]

$$\mathcal{H} = -\gamma_n \hbar \mathbf{I}^i \cdot \mathbf{H}_0 + \sum_j \mathbf{s}^j \cdot \mathbf{A}^{ij} \cdot \mathbf{I}^i + 2\gamma_e \gamma_n \hbar^2 \langle r^{-3} \rangle \ell^i \cdot \mathbf{I}^i + \sum_{\alpha\beta} V^i_{\alpha\beta} Q^i_{\alpha\beta}. \tag{2.1}$$

The first term is the Zeeman interaction due to the external magnetic field, $\mathbf{H}_0$. γ_n is the nuclear gyromagnetic ratio. The second term is the magnetic hyperfine interaction with electron spins where $\mathbf{s}^j$ and $\mathbf{A}^{ij}$ are the spin moment at the j-th sites and the hyperfine coupling tensor between nuclear spins and electron spins, respectively. The third term is the magnetic hyperfine interaction with the non-s-electron orbital moments ℓ where γ_e and r are the electron gyromagnetic ratio and the distance between nuclear spins and electron spins, and causes the anisotropic hyperfine interaction. The last term is the nuclear quadrupole interaction between the electric field gradient(EFG) at the nuclear position $V_{\alpha\beta} = \partial^2 V / \partial x_\alpha \partial x_\beta (x_\alpha(\alpha{=}1,2,3){=}x, y, z)$ and the nuclear quadrupole moments $Q_{\alpha\beta} = \{eQ/6I(2I-1)\}\{3/2(I_\alpha I_\beta + I_\beta I_\alpha) - \delta_{\alpha\beta} I^2\}$.

2.1.1 magnetic hyperfine interactions

Magnetic hyperfine interactions between nuclei and electrons are described below.
(1) *the Fermi contact interaction*
The interaction between the nuclear spin and the s-electron spin is expressed as

$$\frac{8\pi}{3} g_e \gamma_e \gamma_n \hbar^2 \mathbf{s} \cdot \mathbf{I} \delta(\mathbf{r}), \tag{2.2}$$

where g_e is the g-factor of a electron spin.
(2) *the magnetic dipole-dipole interaction*
The magnetic dipole-dipole interaction between the nuclear spin and the non-s-electron spin is expressed as

$$-g_e \frac{\gamma_e \gamma_n \hbar^2}{r^3} \left\{ \mathbf{s} \cdot \mathbf{I} - 3 \frac{(\mathbf{s} \cdot \mathbf{r})(\mathbf{I} \cdot \mathbf{r})}{r^2} \right\}. \tag{2.3}$$

(3) *the core-polarization interaction*
This is the indirect interaction between the nuclear spin and the non-s-electron spin mediated by inner core s-electron spin polarization. The non-s-electron spin modifies the spacial distribution of s-electrons in the inner closed shell due to the exchange interaction between non-s-electron spins and s-electron ones. In result, the Fermi contact interaction(1) is derived indirectly by the non-s-electron spin. And it is expressed as

$$\frac{8\pi}{3} g_e \gamma_e \gamma_n \hbar^2 \sum_k \{ |\psi_k{}^\uparrow(0)|^2 - |\psi_k{}^\downarrow(0)|^2 \} \mathbf{s} \cdot \mathbf{I}, \tag{2.4}$$

where $\psi_k{}^{\uparrow\downarrow}(r)$ is the s-electron wave function with the up- or the down-spin of the k-th electron in the closed shell.

All the magnetic hyperfine interactions described above and the transferred hyperfine interaction from magnetic spins are given by the following expression as

$$\sum_j \mathbf{s}^j \cdot \mathbf{A}^{ij} \cdot \mathbf{I}^i. \tag{2.5}$$

2.1.2 electronic interaction

In addition to the magnetic interactions, there exists the electronic interaction of nuclear quadrupole coupling between the nuclear quadrupole moments and the EFG. Taking the new rectangular coordinates of (X, Y, Z) showing in Fig.2.1.1 correspond to the axes of EFG tensor to satisfy the relation of $|V_{ZZ}| \geq |V_{XX}| \geq |V_{YY}|$, $V_{\alpha\beta} = 0$ and

$$\begin{aligned} \sum_{\alpha\beta} V^i_{\alpha\beta} Q^i_{\alpha\beta} &= \frac{eQ}{4I(2I-1)} \{V_{ZZ}(3{I_Z}^2 - I^2) + (V_{XX} - V_{YY})({I_X}^2 - {I_Y}^2)\} \\ &= \frac{e^2qQ}{4I(2I-1)} \{3{I_Z}^2 - I^2 + \eta({I_X}^2 - {I_Y}^2)\}, \end{aligned} \tag{2.6}$$

where

$$\begin{aligned} eq &\equiv V_{ZZ} \\ \eta &\equiv \frac{(\frac{\partial^2 V}{\partial X^2} - \frac{\partial^2 V}{\partial Y^2})}{\frac{\partial^2 V}{\partial Z^2}}. \end{aligned}$$

2.2 Knight Shift

The Hamiltonian (2.1) is decomposed into the static(time averaged) and the fluctuating parts. The static part is expressed as,

$$\mathcal{H}_{st} = -\gamma_n \hbar \mathbf{I}^i \cdot \mathbf{H}_0 + \sum_j \langle \mathbf{s}^j \rangle \cdot \mathbf{A}^{ij} \cdot \mathbf{I}^i + 2\gamma_e \gamma_n \hbar^2 \langle r^{-3} \rangle \langle \ell^i \rangle \cdot \mathbf{I}^i + \sum_{\alpha\beta} \langle V^i_{\alpha\beta} \rangle Q^i_{\alpha\beta}. \tag{2.7}$$

The above Hamiltonian is modified for $\mathbf{H}_0 \parallel$ z-axis.

$$\begin{aligned} \mathcal{H}_{st} &= -\gamma_n \hbar I^i_z H_0 \Big(1 - \sum_j \frac{\langle s^j_z \rangle A^{ij}_{zz}}{\gamma_n \hbar H_0} - \frac{2\gamma_e \hbar \langle r^{-3} \rangle \langle \ell^i_z \rangle}{H_0}\Big) + \sum_{\alpha\beta} \langle V^i_{\alpha\beta} \rangle Q^i_{\alpha\beta} \\ &= -\gamma_n \hbar I^i_z H_0 (1 - K_{z,s} - K_{z.orb}) + \sum_{\alpha\beta} \langle V^i_{\alpha\beta} \rangle Q^i_{\alpha\beta}, \end{aligned} \tag{2.8}$$

where $K_{z,s}$ and $K_{z,orb}$ are the Knight shift of the spin and orbital parts, respectively. The Knight shift is proportional to the static magnetic susceptibility, i.e.

$$K_{z,s} = \sum_j \frac{\langle s^j_z \rangle A^{ij}_{zz}}{\gamma_n \hbar H_0} = \sum_j \frac{A^{ij}_{zz}}{N g_e \gamma_e \gamma_n \hbar^2} \chi_{z,s} \tag{2.9}$$

$$K_{z,orb} = \frac{2\gamma_e \hbar \langle r^{-3} \rangle \langle \ell^i_z \rangle}{H_0} = 2\frac{\langle r^{-3} \rangle}{N} \chi_{z,orb}, \tag{2.10}$$

where N, $\chi_{z,s}$ and $\chi_{z.orb}$ are the Avogadro's number, the static spin and the orbital(Van Vleck) susceptibility per mole, respectively. Considering the hyperfine magnetic field due to the electron spin and the orbital moments per one Bohr-magneton(μ_B), H^s_{hf} and H^{orb}_{hf}, the Knight shift is expressed as

$$K_s = \frac{H^s_{hf}}{N\mu_B}\chi_s \tag{2.11}$$

$$K_{orb} = \frac{H^{orb}_{hf}}{N\mu_B}\chi_{orb}. \tag{2.12}$$

The hyperfine field is estimated by the Knight shift vs susceptibility(K vs χ) plot with implicit parameter of temperature.

2.3 NMR/NQR Spectrum

2.3.1 NMR spectrum

We assume the quadrupole coupling is weak compared to the magnetic interaction. In this case we can consider that the nuclear spins are quantized along the z-axis parallel to the applied magnetic field. We can treat the quadrupole coupling by the perturbation theory. The result proceeded to the second order is described below.

The Hamiltonian (2.1) is modified in the coordination of (X, Y, Z) showing in Fig.2.1.1 as [3]

$$\begin{aligned}\mathcal{H} = & - h\nu_0 \mathbf{I}\cdot\mathbf{e}_0 \\ & - h\nu_0(K_X I_X e_X + K_Y I_Y e_Y + K_Z I_Z e_Z) \\ & + \frac{1}{6}\nu_Q\left\{3{I_Z}^2 - I(I+1) + \frac{1}{2}\eta({I_+}^2 + {I_-}^2)\right\}\end{aligned} \tag{2.13}$$

$$\begin{aligned}\mathbf{e}_0 &= (e_X, e_Y, e_Z) = \mathbf{H}_0/|\mathbf{H}_0| \\ \nu_0 &= \frac{\gamma_n H_0}{2\pi} \\ \nu_Q &= \frac{3e^2qQ}{2I(2I-1)h},\end{aligned}$$

where ν_0, ν_Q and K are the Larmor frequency, the nuclear quadrupole frequency, and the Knight shift, respectively.

The resonance frequency between $I_z = m$ and $I_z = m-1$, ν_m, is expressed as

$$\begin{aligned}\nu_m(\theta,\phi) &= \nu_0(1+K_{iso}) \\ &+ \frac{1}{2}\nu_0\{K_1(3\cos\theta - 1) - K_2\sin^2\theta\cos 2\phi\} \\ &+ \frac{1}{2}\nu_Q\left(m - \frac{1}{2}\right)\{(-3\cos^2\theta + 1) - \eta\sin^2\theta\cos 2\phi\} \\ &+ \frac{{\nu_Q}^2}{32\nu_{ZM}}\sin^2\theta(g_C\cos^2\theta - g_B)\end{aligned}$$

$$- \frac{\eta {\nu_Q}^2}{48\nu_{ZM}} \sin^2\theta(g_C\cos^2\theta + g_B)\cos 2\phi$$
$$+ \frac{\eta^2 {\nu_Q}^2}{72\nu_{ZM}}\left\{g_A - (g_A + g_B)\cos^2\theta - \frac{1}{4}g_C \sin^4\theta \cos^2 2\phi\right\}, \quad (2.14)$$

where

$$\begin{aligned}
\nu_{ZM} &= \nu_0\left[(1 + K_{iso}) + \frac{1}{2}\{K_1(3\cos^2 - 1) - K_2\sin^2\theta\cos 2\phi\}\right] \\
K_{iso} &= \frac{K_X + K_Y + K_Z}{3} \\
K_1 &= \frac{2K_Z - K_X - K_Y}{3} \\
K_2 &= K_Y - K_X \\
g_A &= 24m(m-1) + 9 - 4I(I+1) \\
g_B &= 6m(m-1) + 3 - 2I(I+1) \\
g_C &= 4g_A + g_B.
\end{aligned}$$

The interval of the resonance frequency between the two satellite lines in the first order is expressed as

$$\nu_m(\theta,\phi) - \nu_{-m+1}(\theta,\phi) = \nu_Q\left(m - \frac{1}{2}\right)(-3\cos^2\theta + 1 - \eta\sin^2\theta\cos 2\phi). \quad (2.15)$$

2.3.2 NQR spectrum

Diagonalizing the static nuclear quadrupole Hamiltonian

$$\mathcal{H}_Q = \sum_{\alpha\beta}\langle V^i{}_{\alpha\beta}\rangle Q^i{}_{\alpha\beta} = \frac{e^2\langle q\rangle Q}{4I(2I-1)}\{3{I_Z}^2 - I^2 + \eta({I_X}^2 - {I_Y}^2)\}, \quad (2.16)$$

the eigen energy, E_m, is obtained, where the nuclear spins are quantized along the Z-axis. We consider the case of I=3/2. The doubly degenerated eigen energy (Kramers doublet) for $I_Z = m$ is obtained as

$$E(\pm 3/2) = \frac{e^2\langle q\rangle Q}{12}\sqrt{3(3+\eta)} \quad (2.17)$$

$$E(\pm 1/2) = -\frac{e^2\langle q\rangle Q}{12}\sqrt{3(3+\eta)}. \quad (2.18)$$

The NQR frequency, ν_{NQR}, is given as

$$\nu_{NQR} = \frac{e^2\langle q\rangle Q}{6}\sqrt{3(3+\eta^2)} = \nu_Q\sqrt{1 + \frac{\eta^2}{3}}. \quad (2.19)$$

2.4 Nuclear Spin-Lattice Relaxation Time (T_1)

The time-dependent fluctuation of the local magnetic field at the nuclear spin causes the nuclear spin-lattice relaxation. The spin-lattice interaction between the nuclear spin and the fluctuating magnetic field, δH_{loc}, is expressed as

$$\mathcal{H}_{fl} = -\gamma_n\hbar\mathbf{I}\cdot\delta\mathbf{H}_{loc}. \quad (2.20)$$

The expression of the spin-lattice relaxation time, T_1, is obtained by treating this interaction as the perturbation Hamiltonian.

We consider the applied magnetic field $\mathbf{H}_0$ is parallel to the z-axis and express the transition probability per unit time between $I_z = m$ and $I_z = m' = m \pm 1$ as $W_{m,m'}$. T_1-rate is defined as

$$\frac{1}{T_1} = \frac{2W_{m,m'}}{(I-m)(I+m+1)}. \tag{2.21}$$

$1/T_1$-rate is generally expressed as [4, 5]

$$\frac{1}{T_1} = \frac{{\gamma_n}^2}{2}\int_{-\infty}^{\infty} dt e^{i\omega_0 t}\langle\{\delta H_{loc}^{+}(t)\delta H_{loc}^{-}(0)\}\rangle, \tag{2.22}$$

where ω_0 is the nuclear magnetic resonance frequency and

$$\begin{aligned} \omega_0 &= \gamma_n|H_0 + \langle H_{loc,z}\rangle| \\ \delta H_{loc}^{\pm} &= \delta H_{loc,x} \pm i\delta H_{loc,y} \\ \{AB\} &= (AB+BA)/2. \end{aligned}$$

The fluctuating local magnetic field is expressed as

$$\delta\mathbf{H}_{loc} = -\sum_j \frac{\mathbf{A}^{ij}\delta\mathbf{s}^j}{\gamma_n\hbar}. \tag{2.23}$$

It is clear in eq.(2.22) that the spin-lattice relaxation is caused by the fluctuation of the local magnetic field perpendicular to the quantized axis.

T_1 is measured by the saturation recovery method. The recovery function of the nuclear spin magnetization was examined by Narath [6] and MacLaughlin et al. [7]. The transition probability per unit time between $I_z = m$ and $I_z = m'$ due to the spin-lattice interaction is expressed as

$$W_{m,m'} = W[|\langle m'|I^+|m\rangle|^2 + |\langle m'|I^-|m\rangle|^2]. \tag{2.24}$$

We consider the population of the m-th state at a time t, $N_m(t)$, and adjacent states is equal at t=0. The relative deviation from equilibrium, $n_m(t)$, is given as

$$n_m(t) = \frac{N_m(t) - N_m^0}{\sum_m N_m^0}, \tag{2.25}$$

where N_m^0 is the population of the m-th state at equilibrium (t=∞). And we define the quantity which is proportional to the magnetization of adjacent pairs of nuclear spin levels, $a_m(t)$, as

$$a_m(t) = n_m(t) - n_{m-1}(t). \tag{2.26}$$

We consider the recovery function in the case of I=3/2.

For m=1/2(the center line)

$$\begin{aligned} a_{1/2}(t) \sim R_{NMR}(t) &= \frac{M(\infty) - M(t)}{M(\infty)} \\ &= 0.1exp(-2Wt) + 0.9exp(-12Wt) \\ &= 0.1exp\Big(-\frac{t}{T_1}\Big) + 0.9exp\Big(-6\frac{t}{T_1}\Big). \end{aligned} \tag{2.27}$$

For m=3/2,−1/2(the satellite lines)

$$\begin{aligned} a_{3/2,-1/2}(t) \sim R_{NMR}(t) &= 0.1exp(-2Wt) + 0.5exp(-6Wt) + 0.4exp(-12Wt) \\ &= 0.1exp\Big(-\frac{t}{T_1}\Big) + 0.5exp\Big(-3\frac{t}{T_1}\Big) + 0.4exp\Big(-6\frac{t}{T_1}\Big). \end{aligned} \quad (2.28)$$

On the other hand, the recovery function in NQR measurements in the case of I=3/2 is expressed as

$$R_{NQR}(t) = exp(-6Wt) = exp\Big(-3\frac{t}{T_1}\Big). \quad (2.29)$$

2.5 Nuclear Spin-Spin Relaxation Time (T_2)

The interaction[1] between nuclear spins is expressed as

$$\mathcal{H}_{II} = \sum_j I_z^i \cdot a_{ij} I_z^j, \quad (2.30)$$

where a_{ij} is the nuclear spin-spin coupling constant. The gaussian spin-spin relaxation rate is expressed as [8]

$$\Big(\frac{1}{T_{2G}}\Big)^2 = \frac{p}{8\hbar^2}\sum_{j\neq i}(a_{ij})^2, \quad (2.31)$$

where p is the natural abundance of a nuclide. The nuclear spin-spin interaction is decomposed into the direct interaction (the classical magnetic dipole-dipole interaction) and the indirect interaction mediated by the electron system. The nuclear spin-spin coupling constant is described as

$$a_{ij} = (a_{ij})_{dip} + (a_{ij})_{ind}, \quad (2.32)$$

where the first term is the direct interaction and the second term is indirect one.

The nuclear spin-echo intensity at a time 2τ is expressed as

$$I(2\tau) = I(0)\Big\{-\frac{1}{2}\Big(\frac{2\tau}{T_{2G}}\Big)^2 - \frac{2\tau}{T_{2L}}\Big\}, \quad (2.33)$$

where τ is the interval between the first $\pi/2$-pulse and the second π-pulse as shown in Fig.2.4.1, and T_{2L} is the spin-spin relaxation time due to the T_1 process.

2.6 Apparatus

Spin-echo measurements were carried out by using the conventional phase-coherent pulsed NMR spectrometer. The block diagram of the typical apparatus is shown in Fig.2.6.1.

In Fig.2.6.2, the NMR/NQR probes are shown in the frequency range of (a) 1∼50MHz and (b) 50∼200MHz.

The solenoid type superconducting magnet(12T at 4.2K) was used in NMR measurements.

R E F E R E N C E S

[1] Charles P. Slichter; PRINCIPLES OF MAGNETIC RESONANCE

[2] A.Abragam; THE PRINCIPLES OF NUCLEAR MAGNETISM

[3] H.Nakamura; Dr. thesis in Osaka University.

[4] T.Moriya; Prog.Theor.Phys. **16** (1956) 23

[5] T.Moriya; J.Phys.Soc.Jpn. **18** (1963) 516

[6] A.Narath; Phys.Rev. **162** (1967) 162

[7] D.E.MacLaughlin, J.D.Williamson and J.Butterworth; Physd.Rev.B **4** (1971) 60

[8] C.H.Pennington and C.P.Slicter; Phys.Rev.Lett. **66** (1991) 381

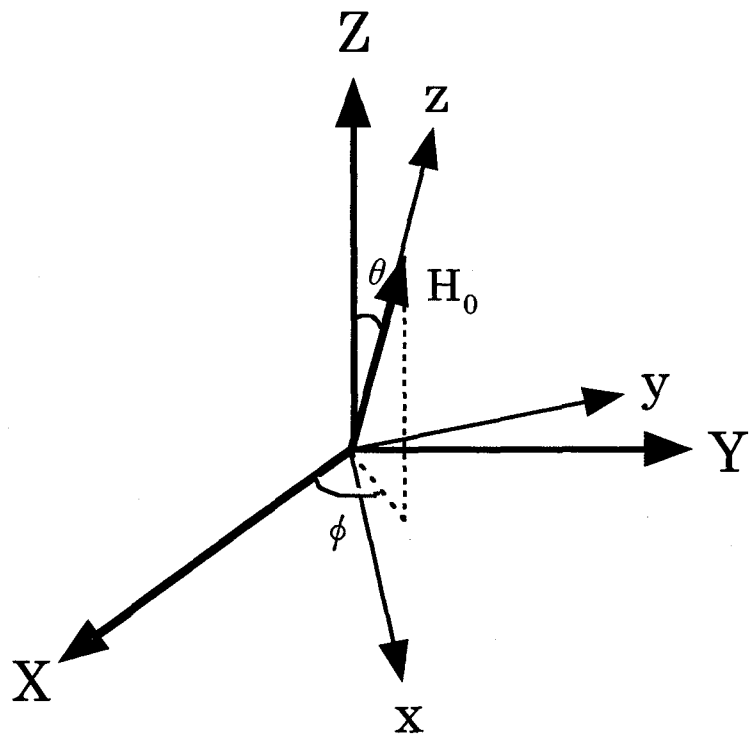

Fig.2.1.1 New rectangular coordinates (X,Y,Z).

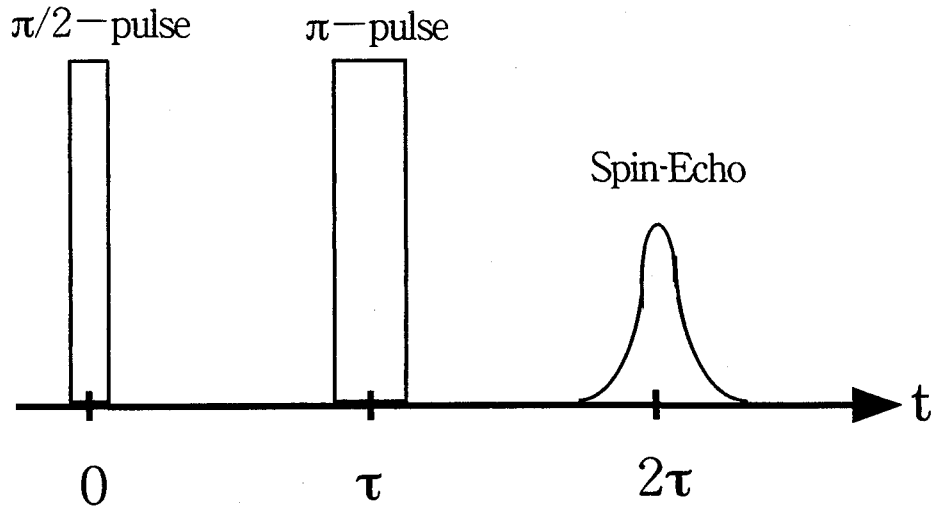

Fig.2.4.1 Spin-Echo formation following $\pi/2-$pulse and $\pi-$one.

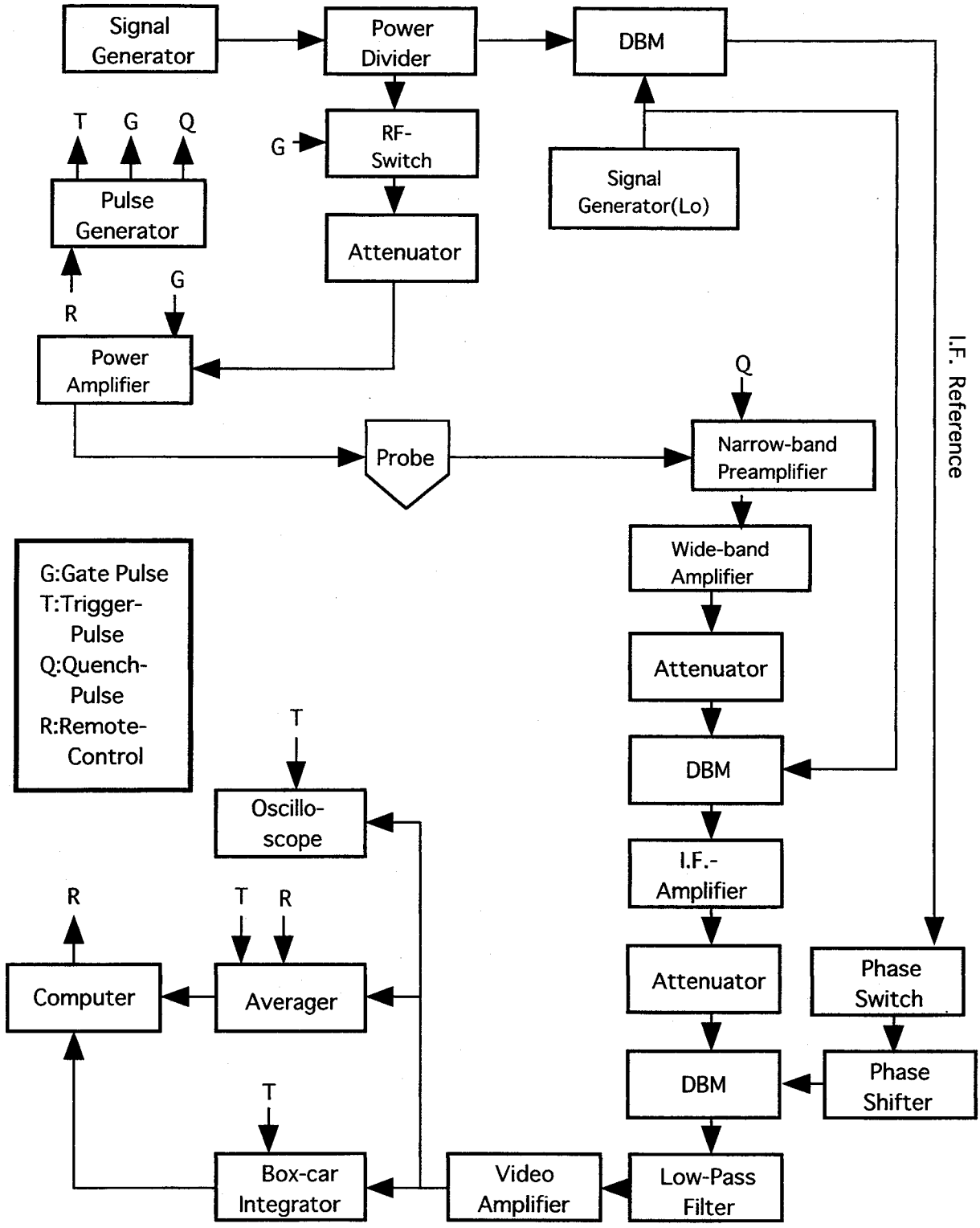

Fig.2.6.1 Block diagram of the phase-coherent pulsed NMR/NQR spectrometer.

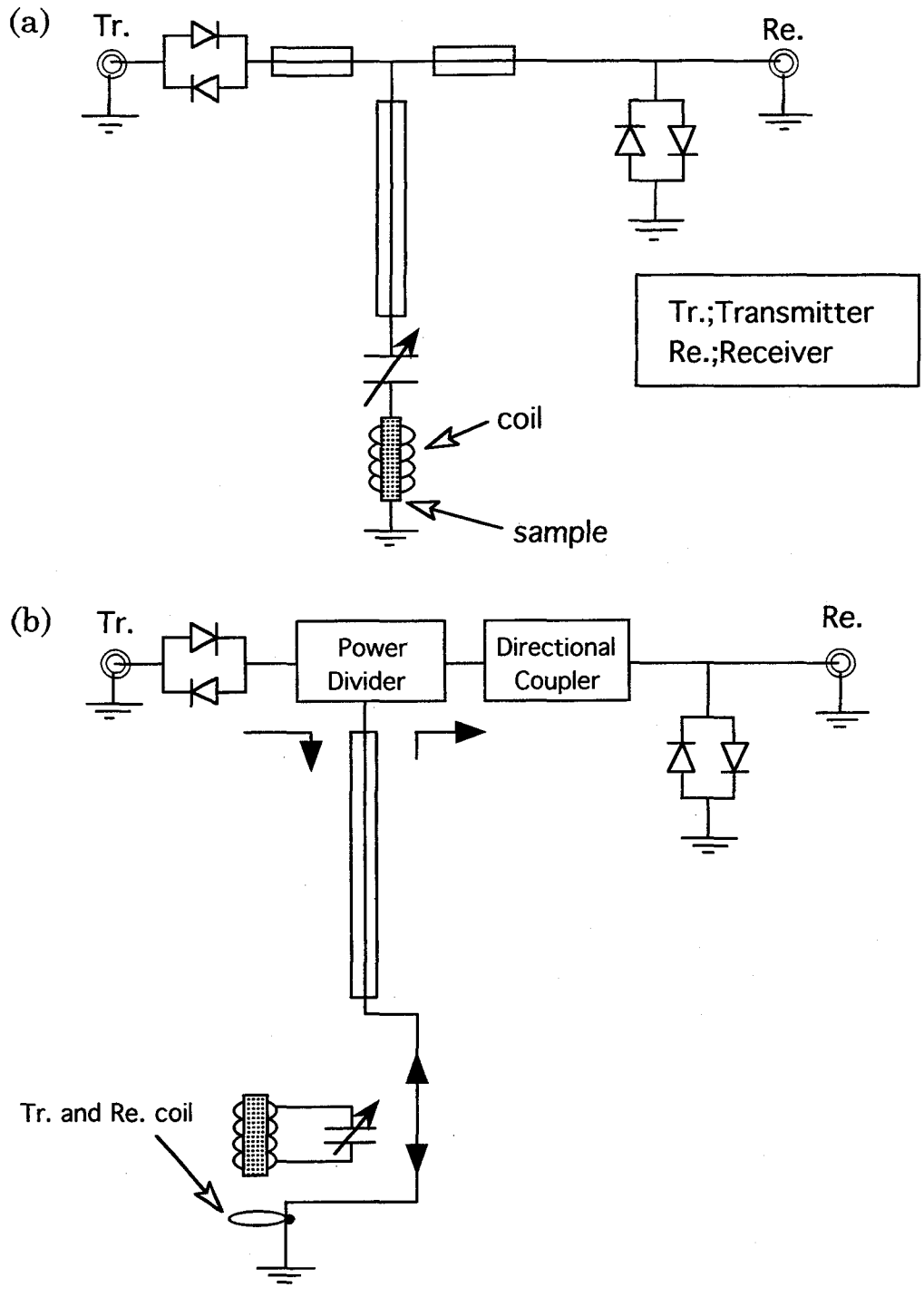

Fig.2.6.2 Probes for NMR/NQR measurements in the frequency range of (a) 1~50MHz and (b) 50~200MHz.

Chapter 3

$LaCuO_{2.5}$

$LaCuO_{2.5}$ is one of new compounds with even-leg ladder structure. Hiroi and Takano have been first synthesized it under high pressure and performed the resistivity and magnetic susceptibility measurements [1]. They have suggested the existence of spin gap in $LaCuO_{2.5}$ from the magnetic susceptibility measurements. The resistivity decreases drastically with substitution of Sr^{2+} for La^{3+} and shows metallic behavior in $La_{0.8}Sr_{0.2}CuO_{2.5}$. Although the superconductivity has never emerged above 1.4K, the carrier(hole) doping into the two-leg ladder system has first been succeeded in $La_{1-x}Sr_xCuO_{2.5}$. In spite of the suggestion of the existence of the spin gap from the magnetic susceptibility measurements, the results in NMR measurements denied it but revealed the long range magnetic ordering [2]. In this chapter the magnetic properties in $La_{1-x}Sr_xCuO_{2.5}$ will be discussed in comparison with those in $SrCu_2O_3$.

3.1 Introduction for $LaCuO_{2.5}$

3.1.1 crystal structure

$La_2Cu_2O_5(LaCuO_{2.5})$ was first synthesized in ambient pressure by Cava et al. [3]. Powdered material was sealed in gold capsules and treated at $900°C$ and under 6GPa for 30 min by using a cubic-anvil-type high pressure apparatus [1]. The products were characterized by means of powder X-ray diffraction(XRD) and electron diffraction(ED). The XRD patterns completely changed after the high-pressure treatment for $x \leq 0.20$ in $La_{1-x}Sr_xCuO_{2.5}$, implying that a structural transformation occurred at high pressure, while for $x = 0.25$ and 0.35 the ambient-pressure structure remained intact. Both the XRD and ED patterns indicate the $CaMO_{2.5}$ structure for $0 \leq x \leq 0.20$, which is one of the prototypes of anion-deficient perovskites [4]; orthorhombic, $a \approx \sqrt{2}a_p$, $b \approx 2\sqrt{2}a_p$, $c \approx a_p$(a_p is lattice parameter of the primitive perovskite structure), space group *Pbam*. The lattice constants are a=5.5482Å, b=10.5295Å and c=3.8801Å, respectively [1].

The dense structure of $LaCuO_{2.5}$ determined by a Rietveld analysis of the powder XRD pattern [5] is illustrated in Fig.3.1.1. Remarkably, the Cu-O sublattice assumes the character of a two-leg ladder along the c-axis in Fig.3.1.1, where only Cu-O bonds shorter than 2Å are shown with solid lines. Owing to a strong Jahn-Teller effect, the Cu-O distance within the ladder is short, ~1.95Å, whereas the Cu-O_{apex} distance is long, 2.29Å. This imbalanced Cu-O configuration leads us to consider that unpaired electrons are confined in the intra-ladder Cu $d_{x^2-y^2}$-O $2p_\sigma$ orbitals and that, therefore, strong antiferromagnetic interactions of order of 10^3K would occur only within the ladders. Inter-ladder interactions will further be weakened as a result of the approximate orthogonality(~68.5°) between adjacent ladders, because electron transfer between mutually orthogonal orbitals are prohibited by symmetry. It may be assumed that each ladder is nearly isolated from the others and provides a quasi-one dimensional electron system.

The systematic replacement of La by Sr can be seen in the continuous variation in the lattice parameters. The Cu-Cu distance along the leg(rung) changes from 3.880Å(3.930Å) for x=0 to 3.865Å(3.890Å) for x=0.20.

3.1.2 resistivity and magnetic susceptibility

A drastic insulator to metal transition has been observed with replacing La by Sr, i.e. doping holes, in the resistivity measurements as shown in Fig.3.1.2 [1]. Non-doped $LaCuO_{2.5}$ is almost insulative, while hole doping systematically decreases resistivity by several orders of magnitude, and finally a metallic behavior down to 5K is seen for x=0.20. The hole-doping into the two-leg ladder system is first succeeded in $La_{1-x}Sr_xCuO_{2.5}$. The magnitude of resistivity for x=0.20 is nearly the same as that in the normal state of superconductor $La_{1.8}Sr_{0.2}CuO_4$. However, no indication of a superconducting transition has been seen for any doping level examined [1].

The temperature dependence of the magnetic susceptibility, χ, in $La_{1-x}Sr_xCuO_{2.5}$ [1] is shown in Fig.3.1.3. In $LaCuO_{2.5}$, χ decreases gradually with decreasing temperature to a minimum around 90K, which is followed by a Curie-like increase at lower temperature. The experimental result was fitted by the following equation [1]

$$\chi = \chi_0 + \frac{C}{T-\Theta} + \alpha\frac{1}{\sqrt{T}}exp\left(-\frac{\Delta}{T}\right), \tag{3.1}$$

where χ_0 is a temperature independent term, and second term is a Curie-Weiss contribution ascribed to impurities and/or Cu^{2+} ions made by crystal imperfections. The last term represents the bulk spin susceptibility expected for a two-leg S=1/2 Heisenberg antiferromagnetic ladder, where α is a constant factor and Δ is the magnitude of the spin gap [11]. The result of fitting was very good as shown in Fig.3.1.3. The obtained values are χ_0=3.8(2)$\times10^{-6}$ emu/mol, C=1.42(1)$\times10^{-3}$ emu/mol, Θ=−5.0(1)K, α=4.11(3)$\times10^{-3}$ and Δ=474(3)K [1]. All these values are very similar to those reported in $SrCu_2O_3$ [1]. The doping dependence of magnetic susceptibility is also shown in Fig.3.1.3. The magnitude increases with doping, and, at the same time, the characteristic decrease for x=0 due to the presence of spin gap seems to fade away gradually. The magnitude of the spin gap is calculated to be 406K(x=0.025) and 364K(x=0.05), which is rather insensitive to doping.

3.2 Experimental Results

In this section, the Cu NMR study is reported in order to clarify the magnetic property in the two-leg ladder compound $LaCuO_{2.5}$ and the Sr-doped compounds, $La_{1-x}Sr_xCuO_{2.5}$ with x=0.025 and 0.05. From the present experiment, it is, however, shown that the parent compound $LaCuO_{2.5}$ is unexpectedly not in the spin liquid ground state with the spin gap, but instead in a magnetically ordered state at low-temperature below ∼110 K, which is sensitive to Sr(holes)-doping, suppressed by substituting Sr for La by 5%. The same polycrystalline samples were used for the NMR measurement as in the previous work, where the detailed procedures to prepare the sample were reported [1].

The Cu NMR measurements have been made in the T-range of 4.2-300 K at a constant frequency of 125.1 MHz. The NMR spectrum was obtained by sweeping magnetic field generated by a superconducting magnet (12 T at 4.2 K). The nuclear spin-lattice relaxation time, T_1, was measured by the saturation recovery method with a single T_1 component.

T_1 was estimated by using the theoretical function of eq.(2.27) for a center line. The spin-echo exponential decay rate, $1/T_2$ was obtained by plotting the spin-echo intensity $I(2\tau)$ as function of time duration, τ between the first and second rf pulses following

$$I(2\tau) = I(0)\exp\left(-\frac{2\tau}{T_2}\right). \tag{3.2}$$

3.2.1 NMR spectrum

The Cu center line NMR spectrum for the powdered polycrystalline sample of $LaCuO_{2.5}$ at T=170K and f=125.1MHz is shown in Fig.3.2.1. Fig.3.2.2 indicates the T-variation of the ^{63}Cu NMR spectrum, which arises from the $(1/2 \leftrightarrow -1/2)$ transition split into two peaks by the second-order electric-quadrupole effect with the nuclear quadrupole frequency, $\nu_Q = 20$ MHz. With decreasing temperature, the spectrum does not shift at all, but starts to broaden and its integrated intensity multiplied by temperature is progressively reduced below around 150 K as indicated in the inset of Fig.3.2.2. As displayed in Fig.3.2.7, since $1/T_2$ is largely enhanced below 150 K, its intensity is evaluated from an extrapolation to τ=0 for the spin-echo decay curve. Nevertheless, the number of Cu sites whose NMR signal is observed is significantly reduced upon cooling. This is considered because spin-spin correlations and/or a short-range order begin to markedly develop towards a possible magnetic transition temperature, making difficult to observe the NMR signal partially. As a result the NMR signal disappears near$\sim$117 K.

In order to obtain further evidences for the magnetic anomaly at low temperature, we have carried out the Cu NMR experiment on the Sr doped compounds $La_{1-x}Sr_xCuO_{2.5}$ with x=0.025 and 0.05. Whereas the temperature below which the Cu-NMR signal disappears is decreased from $\sim$117 K for $LaCuO_{2.5}$ to $\sim$50 K for x=0.025 as indicated in Fig.3.2.3, the Cu NMR signal for x=0.05 is observable down to 4.2 K. As seen in Fig.3.2.3, the NMR spectrum for x=0.025with a two-peak structure at higher temperatures becomes progressively broader with decreasing temperature and then vanishes below $\sim$50K. Although the NMR signal for x=0.05 is observable at 4.2 K, the spectrum is distributed over a broader field range and its integrated intensity multiplied by temperature is significantly reduced upon cooling. The temperature dependent broadening of the Cu NMR spectrum does not follow the Curie law observed in the susceptibility measurement and hence cannot be interpreted only by the dipole fields induced by extrinsic impurity spins and/or intrinsic Cu^{2+} spins produced by Sr doping, i.e. the magnetic inhomogeneity caused by the paramagnetic spins. The NMR intensities in the undoped and 2% Sr doped $LaCuO_{2.5}$ disappear sharply below around 117 and 50 K, respectively, whereas that in 5% Sr doped compound is gradually wiped out upon cooling as shown in Fig.3.2.4, which may be related to the development of short-range magnetic order associated with the inhomogeneous distribution of Sr content. A spin glass like disordered magnetic phase may produce distributed internal fields at Cu nuclei so that the Cu NMR spectrum is wiped out. The latter possibility reminds the spin glass phase existing in the concentration range of $x = 0.02 - 0.05$ for the 2D square lattice system, $La_{2-x}Sr_xCuO_4$. It is apparent that the magnetic anomaly observed in $LaCuO_{2.5}$ is significantly suppressed and a paramagnetic ground state tends to be stabilized by introducing Sr or holes, although some magnetic inhomogeneity remains largely.

3.2.2 nuclear spin-lattice relaxation rate

Correspondingly to these anomalies of the NMR spectrum and $1/T_2$, the temperature dependence of $^{63}(1/T_1)$ in $LaCuO_{2.5}$ does not bear resemblance at all to the typical spin gap behavior observed in $SrCu_2O_3$ [2] indicated together in Fig.3.2.5. $^{63}(1/T_1)$ decreases down to 230 K being in a process to seemingly form a spin gap like state, but it tends to be constant and begins to be enhanced below ~150 K. From a sharp increase of $1/T_1$ below 150 K, one may remind that a critical behavior of $1/T_1$ near the Néel temperature, T_N is described by the formula of $1/T_1 \sim 1/\sqrt{(T-T_N)}$ [9]. Accordingly, although the data are not so enough for a precise determination of T_N, such a fit to the data below 150 K allows us to give a rough estimation of T_N being around 110 K as indicated by solid line in Fig.3.2.5. The μSR experiment on $LaCuO_{2.5}$ has also confirmed a sharp magnetic transition below around 120 K [10] being consistent with the Cu-NMR results. It is evident that $LaCuO_{2.5}$ is not in the singlet spin liquid state, but instead a magnetic ordering occurs below around ~110 K.

In striking contrast to $LaCuO_{2.5}$, $^{63}(1/T_1)$ for $SrCu_2O_3$ revealed an exponential decrease close to 100 K as shown in the inset in Fig.3.2.5, although dominated at low temperatures by spin fluctuations caused by small amount of $Sr_2Cu_3O_5$ presenting as impurity phases [1, 2]. Furthermore, the Cu NMR spectrum in $SrCu_2O_3$ was observable at low temperatures. These results gave firm evidences that $SrCu_2O_3$ is in the short-range resonating valence bond (RVB) ground state where the spin correlation decays exponentially. In spite of the superficial similarity of the susceptibility between $LaCuO_{2.5}$ and $SrCu_2O_3$, it is considered that the antiferromagnetic interladder interaction in $LaCuO_{2.5}$, which are not frustrated, makes a spin liquid state unstable in contrast to the case of $SrCu_2O_3$.

3.3 Discussion

The 3D magnetic ordering in $LaCuO_{2.5}$ reveals that the inter-ladder coupling is rather large but not frustrated such as in $Sr_{14}Cu_{24}O_{41}$. The intra-ladder interactions indicated with solid lines and the inter-ladder interactions with dashed ones are shown in Fig.3.3.1 (a) for $LaCuO_{2.5}$ and (b) for $SrCu_2O_3$. In $LaCuO_{2.5}$, Cu-O bonds lead to a strong AF interaction of order 10^3 K for the intra-ladder 180° Cu($3d_{x^2-y^2}$)-O($2p_\sigma$)-Cu($3d_{x^2-y^2}$) bonds such as that in $SrCu_2O_3$ indicated in Fig.3.3.1(b), but to a weak interaction for the inter-ladder 152.2° Cu-O_{apex}-Cu bonds. In contrast to this complicated coupling among ladders in $LaCuO_{2.5}$, each ladder in $SrCu_2O_3$ is coupled through the 90° Cu-O-Cu bond at the interface between ladders as indicated by dash line in Fig.3.3.1(b) and hence the interaction across the interface between ladders must be ferromagnetic [1]. Furthermore, the shearing causes spin frustration due to the symmetry at the interface (see dash line in Fig.3.3.1(b)). This may be one of the reasons why the experimental value of spin gap ($\Delta = 450 \sim 650$K) in $SrCu_2O_3$ [1, 2] is in agreement with the theoretical prediction calculated to be about $J/2$~650K on the assumptions that the inter-ladder interaction is ignored and J is nearly the same as 1300 K for the linear Cu-O-Cu bond in the square lattice [11, 12]. Consequently, this difference of inter-ladder interaction turns out to lead to a contrast.

Normand and Rice have recently shown that the inter-ladder exchange constant, J', in $LaCuO_{2.5}$ is not so small with a value of ~$0.2J$ where J is the intra-ladder exchange constant and pointed out a possibility of the magnetic ordering because of the system being

close to the quantum critical point [13]. On the other hand, Troyer et al. have obtained the critical ratio of the inter-ladder interaction to the intra-ladder one of $J'/J \sim 0.11$ and derived the temperature dependence of the uniform susceptibility as $\chi = aT^2$ [14].

Mizokawa et al. have confirmed the inter-ladder interactions to be ferromagnetic by the cluster-model of photoemission spectra and subsequent Hartree-Fock band-structure calculation [15].

3.4 Conclusion

In conclusion, the present Cu NMR experiments have revealed that the ground state of $LaCuO_{2.5}$ is not in the spin liquid state with a spin gap in disagreement with the previous suggestion from the susceptibility measurement [1]. Alternatively, it has been shown that a magnetic ordering takes place below $T_N \sim 110$ K as evidenced by the large increase of $1/T_1$ and the divergent behavior of $1/T_2$ leading to the disappearance of the Cu-NMR signal. The recent μSR experiment has observed the magnetic transition below around 120 K [10] consistent with the result of the NMR measurement. Furthermore, NMR measurements have clarified that T_N is strongly reduced upon doping and the paramagnetic state is stabilized by substituting Sr for La by 5%. The present NMR experiments have found a contrast of the ground state between the two-leg ladder compounds, $SrCu_2O_3$ and $LaCuO_{2.5}$. The magnetic interaction among the ladders in $LaCuO_{2.5}$, which is not frustrated, has been pointed out to lead to the magnetically ordered state. This statement may be supported by the recent theoretical analysis that the system is close to the quantum critical point due to not so small inter-ladder exchange interaction with a value of $\sim 0.2J$ [13] or $\sim 0.11J$ [14]. No sign of superconductivity in the Sr-doped $LaCuO_{2.5}$ compound may be partially responsible for the lack of a spin gap in the parent compound $LaCuO_{2.5}$.

R E F E R E N C E S

[1] Z. Hiroi and M. Takano; Nature **377** (1995) 41.

[2] S.Matsumoto, Y.Kitaoka, K.Ishida, K.Asayama, Z.Hiroi, N.Kobayashi and M.Takano; Phys.Rev.B **53** (1996) R11942.

[3] R.J.Cava et al.; Physica C **177** (1991) 115.

[4] K.R.Poeppelmeier, M.E.Leonowicz and J.M.Longo; J.Solid state Chem. **44** (1982) 1415.

[5] F.Izumi in *The Rietveld Method*(ed. R.A.Young) (Oxford Univ. Express, Oxford,1993)

[6] M.Troyer, H.Tsunetsugu and D.Würts; Pys.Rev.B **50** (1994) 13515.

[7] M.Azuma, Z.Hiroi, M.Takano, K.Ishida and Y.Kitaoka; Phys.Rev.Lett. **73** (1994) 3463.

[8] K.Ishida, Y.Kitaoka, K.Asayama, M.Azuma, Z.Hiroi and M.Takano; J.Phys.Soc.Jpn. **63** (1994) 3222.

[9] T.Moriya; Prog.Theor.Phys. **28** (1962) 371

[10] R.Kadono, H.Okajima, A.Yamashita, K.Ishii, T.Yokoo, J.Akimitau, N.Kobayashi, Z.Hiroi, M.Takano and K.Nagamine; Phys.Rev.B **54** (1996) R9628.

[11] E.Dagotto, J.Riera and D.J.Scalpino; Phys.Rev.B **45** (1992) 5744.

[12] T.M.Rice, S.Gopalan and M.Siegrist; Europhys.Lett. **23** (1993) 445.

[13] B.Normand and T.M.Rice; Phys.Rev.B **54** (1996) 7180.

[14] M.Troyer, M.E.Zhitomirsky and K.Ueda; Phys.Rev.B **55** (1997) R6117.

[15] T.Mizokawa, K.Ootomo, T.Konishi, A.Fujimori, Z.Hiroi, N.Kobayashi and M.Takano;Phys.Rev.B **55** (1997) R13373.

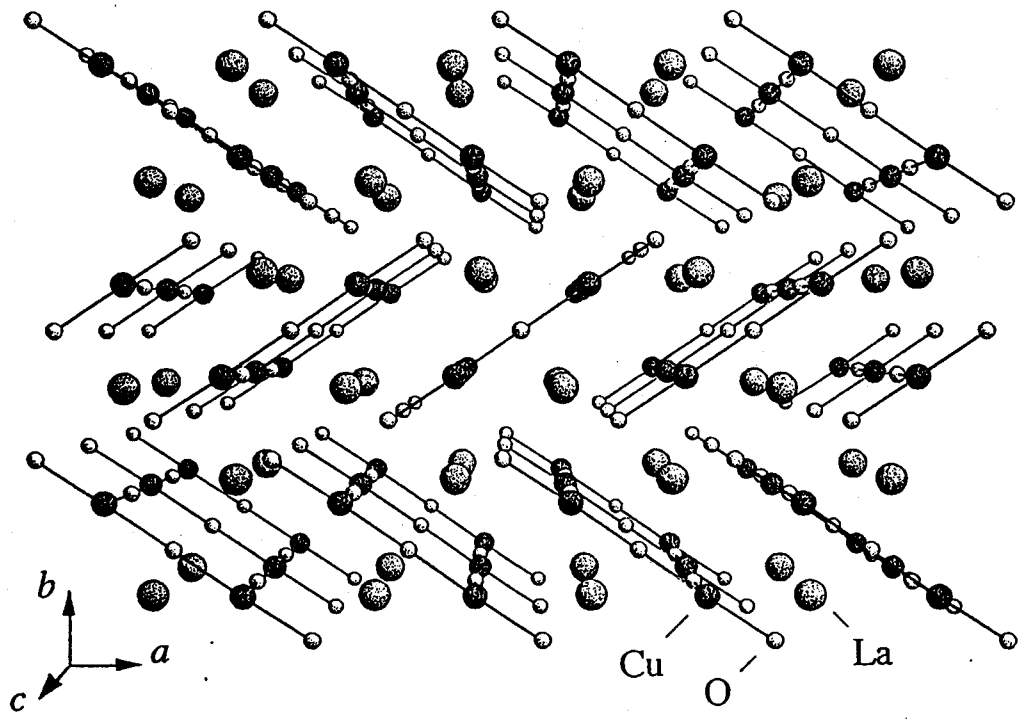

Fig.3.1.1 Perspective view of the crystal structure of $LaCuO_{2.5}$ prepared at high pressure showing the geometrical arrangement of the Cu-O ladders. The coordinate system on the lower left specifies the crystallographic directions[1].

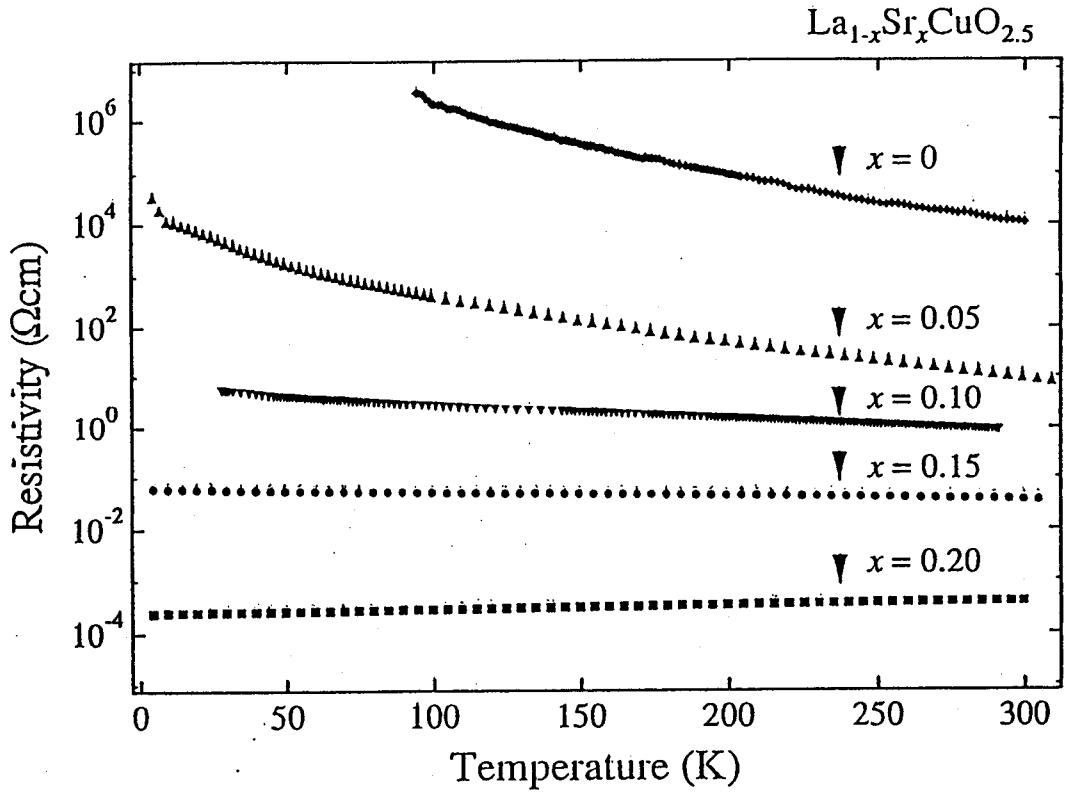

Fig.3.1.2 A series of resistivity versus temperature curves which were measured by a standard four probe method[1].

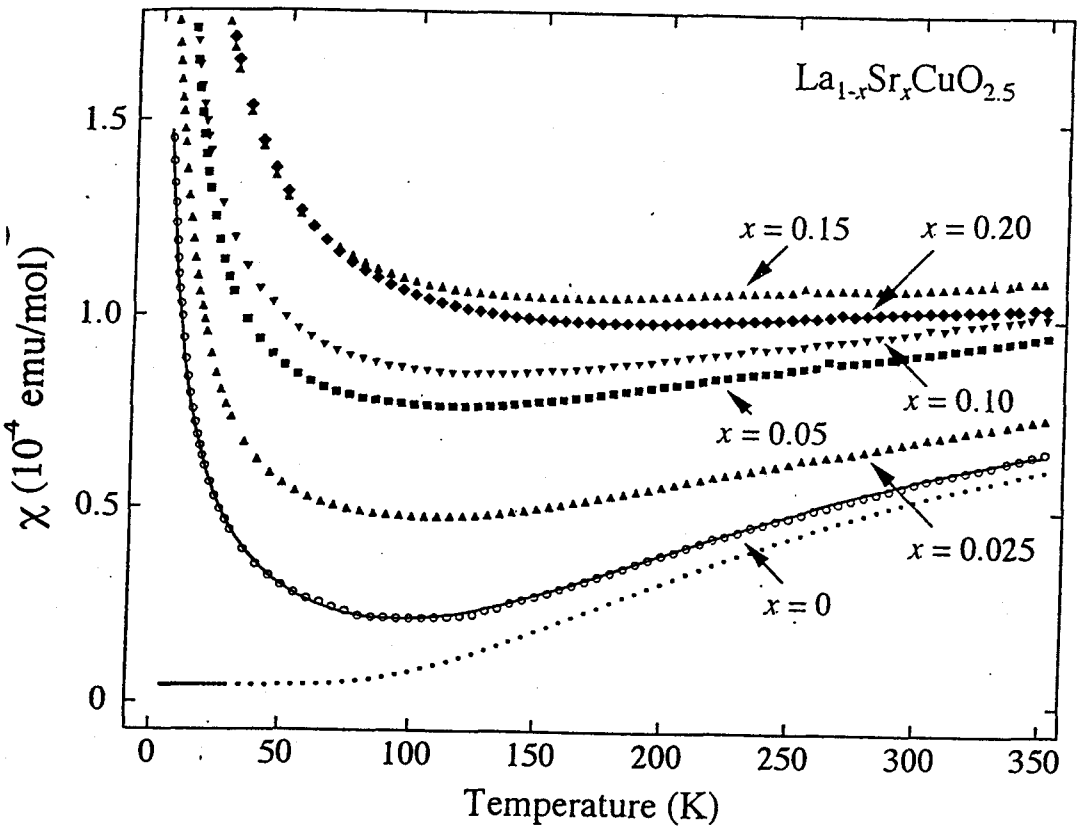

Fig.3.1.3 Temperature dependence of magnetic susceptibility χ measured with a SQUID magnetometer at an applied magnetic field of 1T on heating after zero-field cooling. The data for x=0 is well fitted by the equation in the text as represented by the solid line. The lowest dotted line is the data for x=0 after subtraction of the Curie component[1].

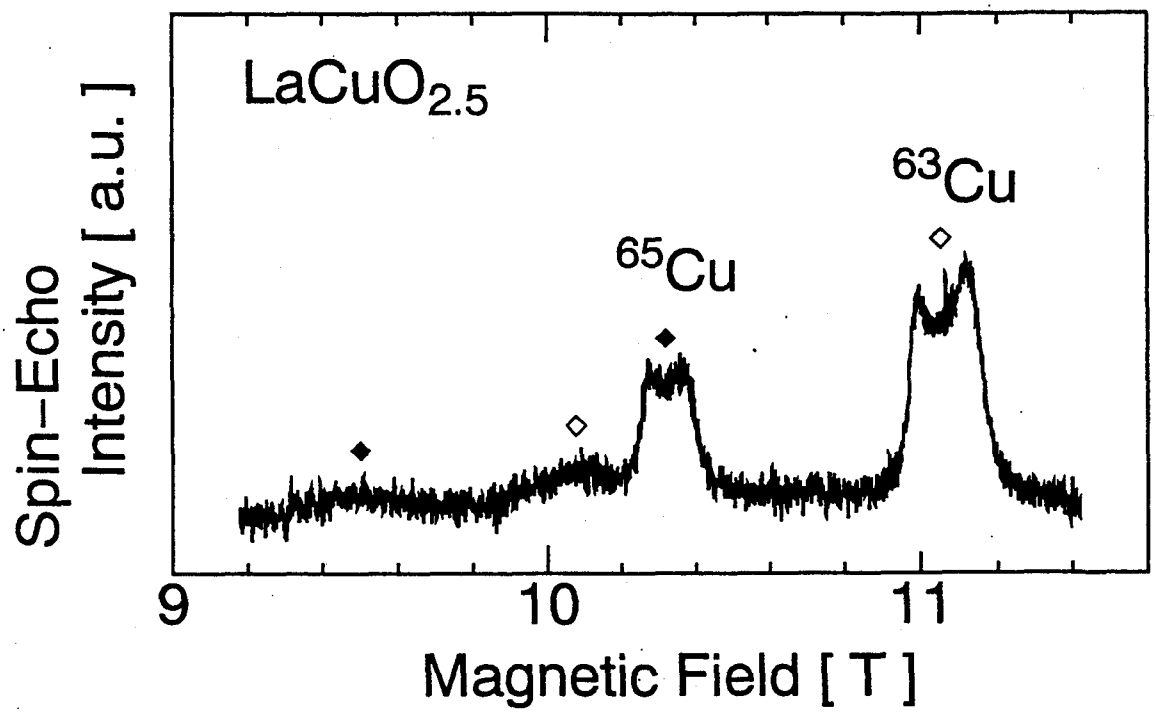

Fig.3.2.1 Cu NMR spectrum in the polycrystalline powdered sample of $LaCuO_{2.5}$ at T=170K and f=125.1MHz.

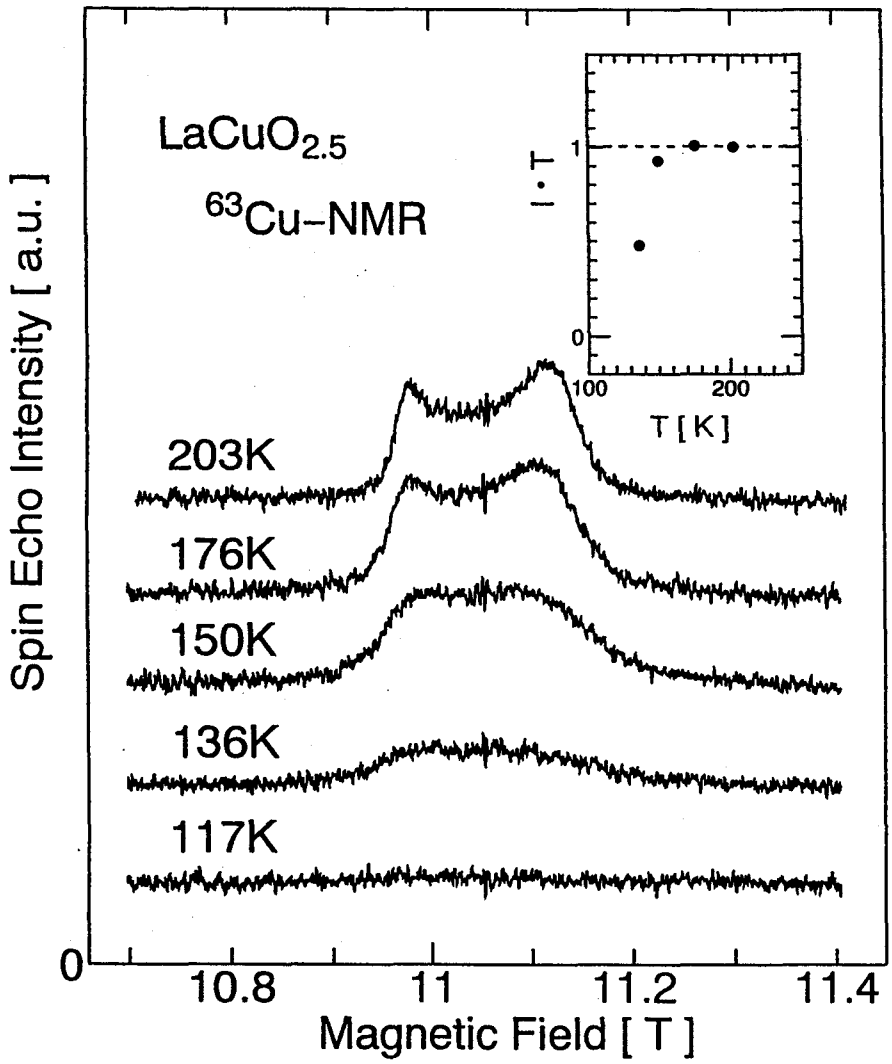

Fig.3.2.2 Temperature variation of ^{63}Cu NMR spectrum in $LaCuO_{2.5}$ at 125.1MHz. Inset indicates the temperature dependence of integrated Cu NMR intensity multiplied by temperature.

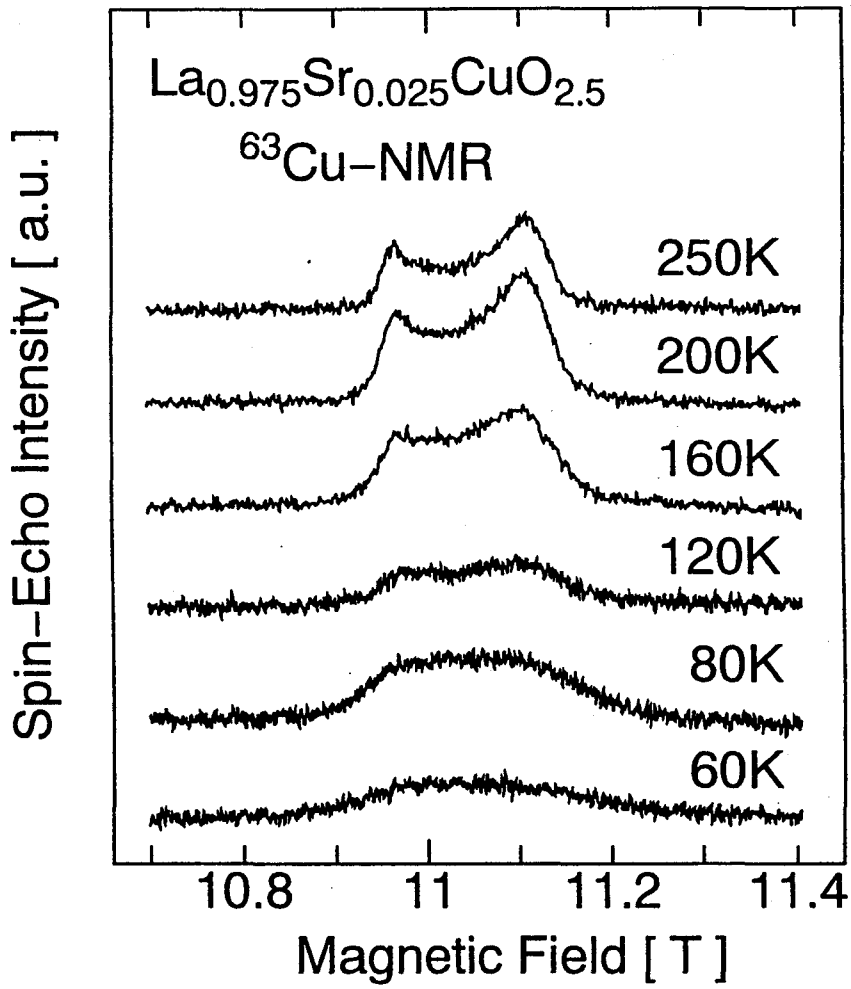

Fig.3.2.3 Temperature variation of ^{63}Cu NMR spectrum in $La_{0.975}Sr_{0.025}CuO_{2.5}$. The NMR signal is observable down to ~50K in contrast to the undoped $LaCuO_{2.5}$.

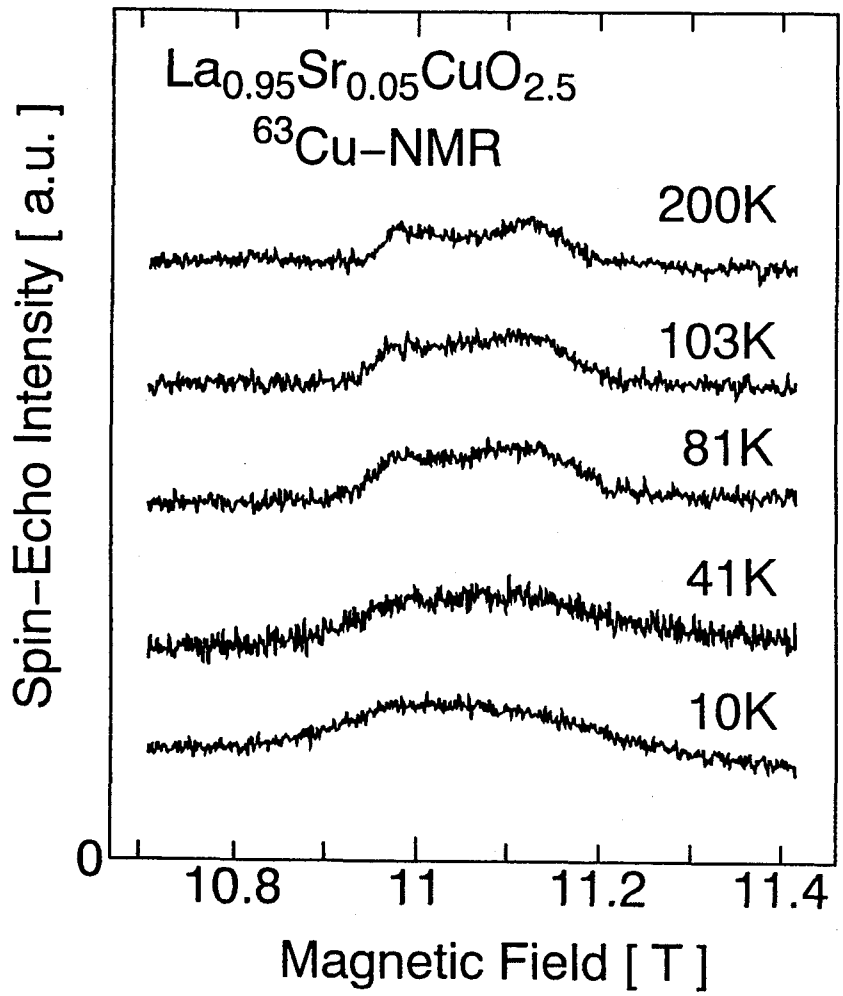

Fig.3.2.4 Temperature variation of ^{63}Cu NMR spectrum in $La_{0.95}Sr_{0.05}CuO_{2.5}$. The NMR signal is observable down to 4.2K.

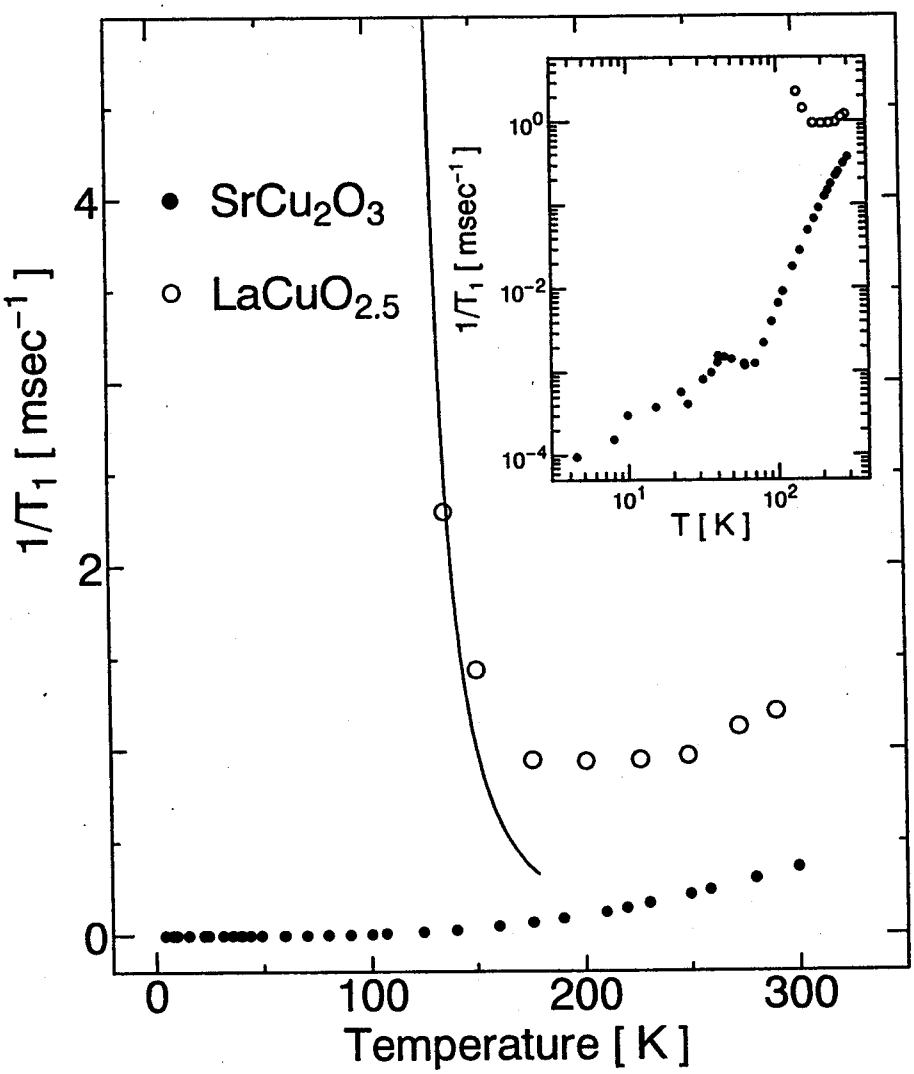

Fig.3.2.5 Temperature dependence of $^{63}(1/T_1)$ for $LaCuO_{2.5}$ and $SrCu_2O_3$[8]. The inset indicates plots in logarithmic scales. The solid line is a fit of data below 150K to $1/T_1 \sim \sqrt{T - T_N}$ with $T_N \sim 110$K.

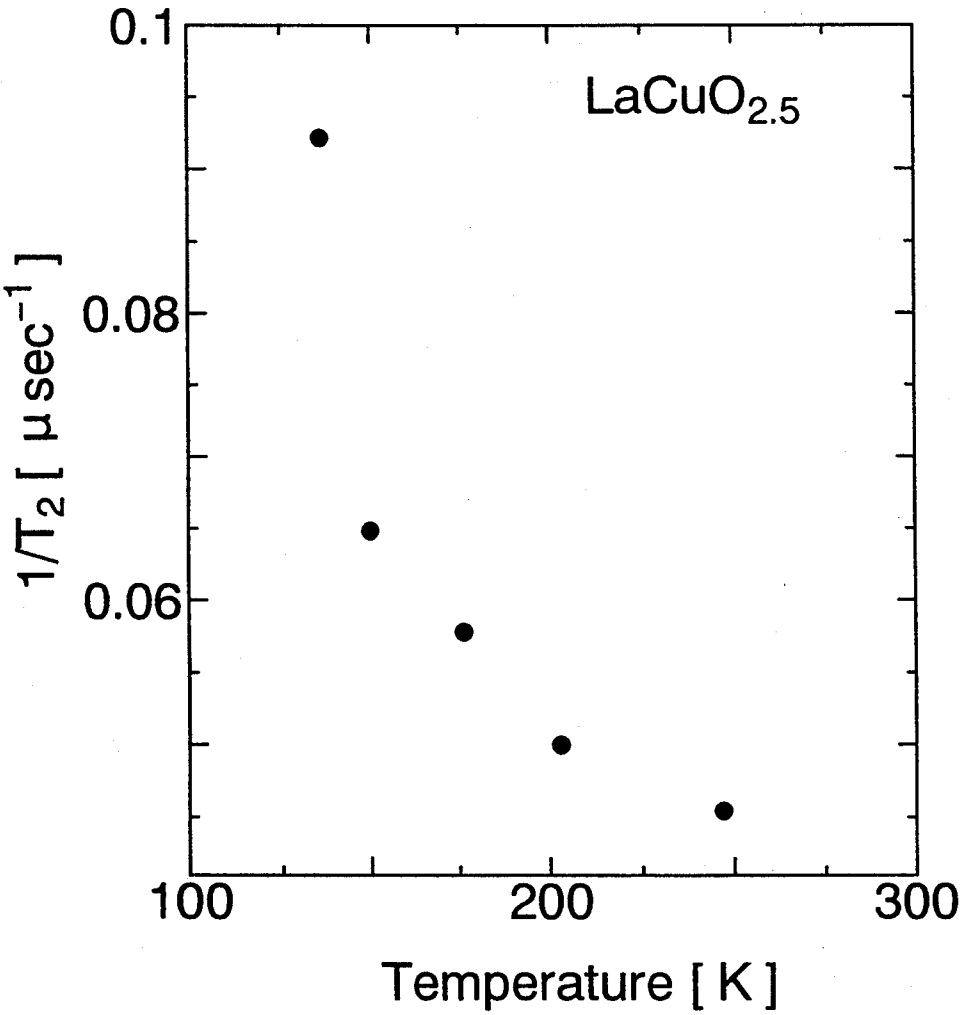

Fig.3.2.6 Temperature dependence of the exponential spin-spin relaxation rate, $1/T_2$, in $LaCuO_{2.5}$.

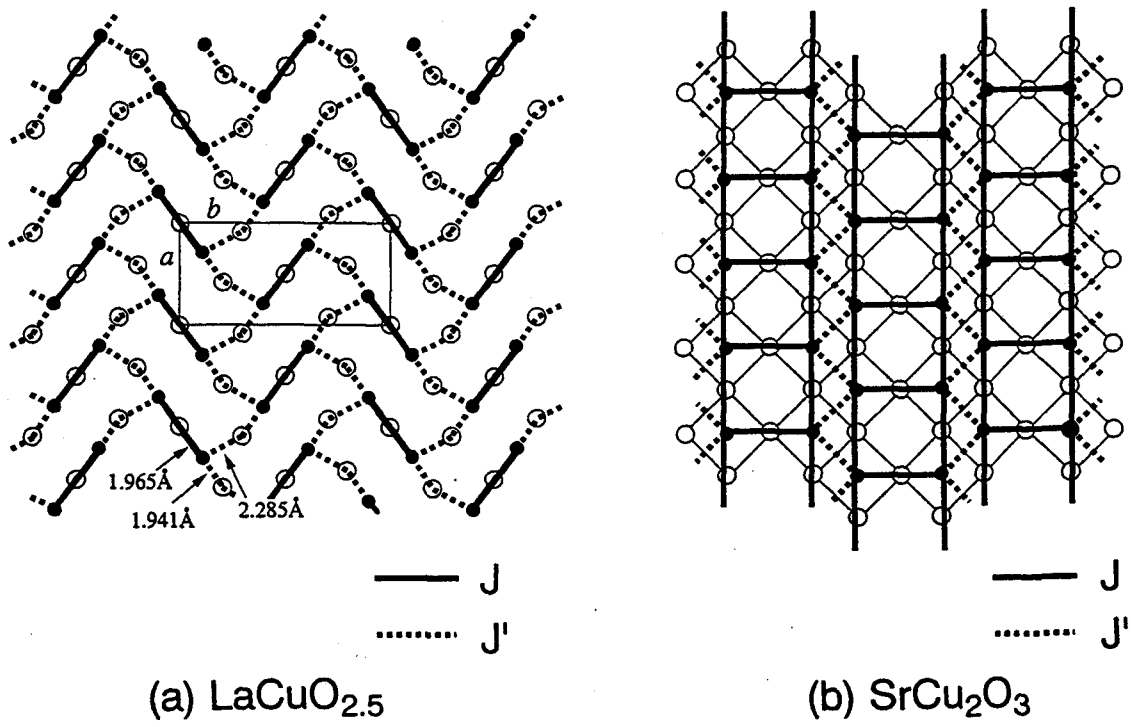

Fig.3.3.1 (a) Perspective view of structure of $LaCuO_{2.5}$ projected to the a-b plane in which La coordination is omitted and two-leg ladders are along the c axis. (b) Structure of $SrCu_2O_3$ projected to the a-b plane in which Sr layers are stacked along the c-axis and two-leg ladders are running along the b-axis.

Chapter 4

$Sr_{14}Cu_{24}O_{41}$

$Sr_{14}Cu_{24}O_{41}$ comprises two unique quasi-one-dimensional structures of the Cu_2O_3 two-leg ladder lattice and the CuO_2 zigzag chain. The ladder structure is expected to have a large spin gap of 420K$\sim$700K as confirmed in $SrCu_2O_3$ [1, 2]. Existence of the spin gap is suggested in the CuO_2 chain by the magnetic susceptibility measurements [4, 5]. The ladder- and chain-Cu NMR/NQR measurements have been performed on single crystals of $Sr_{14}Cu_{24}O_{41}$ and $Sr_{13.75}Y_{0.25}Cu_{24}O_{41}$(Y(0.25)), which were grown by the traveling-solvent floating-zone method and confirmed by the X-ray Laue method [6, 5]. In $Sr_{14}Cu_{24}O_{41}$, there found a significant sample dependence in the experimental results. Two single crystals of $Sr_{14}Cu_{24}O_{41}$ were investigated. The possibility of oxygen nonstoichiometry or cation deficiencies must be considered. Hereafter, the author calls two $Sr_{14}Cu_{24}O_{41}$ samples Sr14-A and Sr14-B.

4.1 Introduction for $Sr_{14}Cu_{24}O_{41}$

4.1.1 crystal structure

The crystal structure of $Sr_{14}Cu_{24}O_{41}$ was reported by McCarron et al. [7] and Siegrist et al. [8]. This compound with the orthorhombic symmetry comprises (b) a 1D-CuO_2 chain, (c) a Sr layer and (d) a two-leg Cu_2O_3 ladder layer as illustrated in Fig.4.1.1. Each layer is alternately stacked along the b-axis with spacing of $\sim$1.6Å. The two-leg ladder structure similar to that in $SrCu_2O_3$ is constructed in the Cu_2O_3 layers.

The space group and lattice constants of orthorhombic two subcells and universal cell obtained by McCarron et al. [7] are described below.

cell	space group	a[Å]	b[Å]	c[Å]
CuO_2	$Amma$	11.456	13.361	2.749
$Sr_2Cu_2O_3$	$Fmmm$	11.462	13.376	3.931
$Sr_{14}Cu_{24}O_{41}$	$Pcc2$	11.469	13.368	27.501

The lattice constants a and b are similar in both subcells, but c along the leg is different. The relation of the lattice constant along the c-axis is $10\times c_{chain}\simeq 7\times c_{ladder}$, where c_{chain} and c_{ladder} are the lattice constant along the c-axis in the CuO_2 subcell and $Sr_2Cu_2O_3$ subcell, respectively.

4.1.2 resistivity and magnetic susceptibility

As shown in Fig.4.1.2 [4], the temperature dependence of the resistivity for $Sr_{14}Cu_{24}O_{41}$ exhibits insulating behavior, while there exist six holes per unit cell due to excess oxygen. The resistivity decreases with substitution of Ca^{2+} for Sr^{+2} [9], but increases with Ba^{2+} or Y^{3+}. The superconducting transition at 12K under high pressure of 3GPa in $Sr_{0.4}Ca_{13.6}Cu_{24}O_{41.84}$ was discovered by Uehara et al. [10].

The T-dependence of the magnetic susceptibility on the single crystal of $Sr_{14}Cu_{24}O_{41}$ for each direction is shown in Fig.4.1.3(a) [6]. We can find a broad peak around 80K for each direction. The magnetic susceptibility obtained by subtraction of the Curie-Weiss contribution along the a-axis is shown in Fig.4.1.3(b). The contribution to the magnetic

susceptibility from the Cu_2O_3 two-leg ladder system can be neglected below 300K because of the large spin gap. A broad peak is attributed to the contribution from the CuO_2 chain. Matsuda and Katsumata [5] have studied the magnetic susceptibility in detailed and extracted the magnetic susceptibility originating from the CuO_2 chain, χ_{chain}. From an analyses by the dimer model of

$$\chi_D = \frac{N g_e \mu_B^2}{k_B T} \cdot \frac{1}{3 + exp(\Delta/T)}, \tag{4.1}$$

the spin gap is estimated to be Δ=133K in CuO_2 chain .

4.2 Experimental Results in the Cu_2O_3 Two-leg Ladder Site

4.2.1 NMR/NQR spectrum

NMR spectrum is obtained by sweeping the applied magnetic field at a fixed frequency. The Cu-NMR spectra in Sr14-A and Sr14-B are shown in Fig.4.2.1. The NMR spectrum for H||b-axis at T=30K and f=83.1MHz in Sr14-A is shown in Fig.4.2.1(A). Two sets of ladder- and chain-Cu NMR spectra are splitted by the nuclear quadrupole interaction. Arrows mark the chain-Cu NMR spectra due to the twins in the single crystal Sr14-A which will be described in **4.2.2**. The quadrupole frequency (ν_Q) is a clue to discriminate between the ladder- and the chain-Cu signals, because the ladder-Cu must have a similar ν_Q to $SrCu_2O_3$ [2]. NMR spectra in Sr14-B for (B1) H||b-axis, (B2) H||a-axis and (B3) H||c-axis are shown in Fig.4.2.1. Using eq.(2.15) with θ=0, the nuclear quadrupole tensor components for the ladder-site ^{65}Cu in Sr4-B are estimated to be $^{65}\nu_a$=-2.4MHz(60K), $^{65}\nu_b$=12.4MHz(20K) and $^{65}\nu_c$=-10.2MHz(60K), respectively.

Cu-NQR spectra are obtained by tracing the amplitude of the spin-echo intensity against the frequency in zero magnetic field. A single peak NQR spectrum at 200K splits into multiple peaks at 4.2K as shown in Fig.4.2.2. An appearance of multiple peaks in NQR means that electron field gradient(EFG) at each Cu site is not uniform due to the localization of inherent holes in the two-leg ladder system.

4.2.2 splitting and broadening of the NMR spectrum

The T-variation of the ladder-^{63}Cu center line NMR spectrum for H||b-axis in Sr14-A is shown in Fig.4.2.3, where H_{resII} is defined in **4.2.3**. There is no significant change in the T-range of 20-290K. In contrast, a drastic change is observed in Sr14-B. The T-variation of the ladder-^{63}Cu center line NMR spectrum in Sr14-B is shown in Fig.4.2.4 for (a) H||b-axis, (b) H||a-axis and (c) H||c-axis. There is no significant difference of the line shape between Sr14-A and Sr14-B above 100K. The NMR spectrum in Sr14-B starts to split into two and broaden below100K. The low and the high peaks are defined as H_{res1} and H_{res2}, respectively. In Fig.4.2.4, the spectrum is plotted against H-(H_{res1}+H_{res2})/2. Because the NMR spectrum below 20K for H||b-axis is masked by the chain-^{63}Cu signal, the higher field part in the NMR spectrum below 20K is omitted in Fig.4.2.4(a). The spectra below 100K for H||a-axis and H||c-axis are shown in Fig.4.2.4(b) and Fig.4.2.4(c), respectively.

The T-dependence of the ladder-^{63}Cu resonance field at f=125.1MHz, H_{res}, is plotted in Fig.4.2.5. The ladder-^{63}Cu NMR spectrum of the center line at 60K is shown in the inset in

Fig.4.2.5, where the up and the down triangle correspond to H_{res2} and H_{res1}, respectively. The experimental results above 100K are well fitted by a solid curve expressed as

$$H_{res}(T) = H_{res}(0) + A\frac{1}{\sqrt{T}}exp\left(-\frac{\Delta}{T}\right), \tag{4.2}$$

where A and Δ are a fitting parameter and the magnitude of the spin gap, respectively. The above equation is obtained from the following equation derived by Troyer et al [11].

$$\chi_s \sim \frac{1}{\sqrt{T}}exp\left(-\frac{\Delta}{T}\right). \tag{4.3}$$

The T-dependence of the ladder-^{63}Cu full-width at the half-maximum(FWHM) for H||b-axis in Sr14-B is shown in Fig.4.2.6 as compared with that in Sr14-A. FWHM increases with decreasing temperature below 100K in Sr14-B. The inverse of $(FWHM)_b$ exhibits the Curie-Weiss like T-dependence as shown in the inset in Fig.4.2.6, while the slope changes around 15K. The T-dependence of FWHM for H||a-axis (open square), H||b-axis (solid circle) and for H||c-axis (solid diamond) are shown in Fig.4.2.7. The magnitude of FWHM for H||a- and c-axis are similar, but that for H||b-axis is larger than others. In the inset of Fig.4.2.7, $(FWHM)_b$ is plotted against $(FWHM)_a$ or $(FWHM)_c$ with implicit parameter of temperature. It is found that $(FWHM)_b$ is proportional to $(FWHM)_a$ and $(FWHM)_c$. The ratio of $(FWHM)_b$ to $(FWHM)_a$ and $(FWHM)_c$ are estimated to be 2.6±0.2 and 2.1±0.2, respectively.

The T-dependence of $(H_{res2}-H_{res1})/2=\Delta H/2$ for H||a-axis (open square), H||b-axis (solid circle) and for H||c-axis (solid diamond) are shown in Fig.4.2.8. The magnitude of $\Delta H/2$ for H||a- and c-axis are similar, but that for H||b-axis is larger than others. It is found that $(\Delta H/2)_b$ is proportional to $(\Delta H/2)_a$ and $(\Delta H/2)_c$. In the inset of Fig.4.2.8, $(\Delta H/2)_b$ is plotted against $(\Delta H/2)_a$ or $(\Delta H/2)_c$ with implicit parameter of temperature. The ratio of $(\Delta H/2)_b$ to $(\Delta H/2)_a$ and $(\Delta H/2)_c$ are estimated to be 3.6±0.2 and 3.4±0.1, respectively.

The shift of the center line is affected by the Knight shift and the second order quadrupole effect. It is expressed by eq.(2.14) for ^{63}Cu with θ=0 as

$$\frac{\omega - {}^{63}\gamma_n H_{res}}{{}^{63}\gamma_n H_{res}} = K_z + \frac{\eta^2 \nu_Q^2}{12(1+K_z)({}^{63}\gamma_n H_{res})^2}, \tag{4.4}$$

where K_z is the Knight shift along the magnetic field. Thus the second order quadrupole shift is subtracted by extrapolating $1/({}^{63}\gamma_n H_{res})^2$ to zero in $(\omega - {}^{63}\gamma_n H_{res})/{}^{63}\gamma_n H_{res}$ vs $1/({}^{63}\gamma_n H_{res})^2$ plot for H_{res1} and H_{res2} at 40K and 60K in Sr14-B. The extrapolation of H_{res} reveals that the splitting of spectrum is not due to the second order quadrupole effect. $\Delta H/2$ increases with increasing magnetic field.

The magnetic field dependence of $(\Delta H/2)_b$ at 30K (solid square), 40K (open circle) and 60K (solid circle) are shown in Fig.4.2.10. $(\Delta H/2)_b$ decreases with decreasing magnetic field. It is concluded that $\Delta H/2$ is not caused by the internal magnetic field due to the antiferromagnetic ordering, but induced by the magnetic field. The T-dependence of the threshold magnetic field obtained by fitting $(\Delta H/2)_b$ with linear function is shown in Fig.4.2.10(b). The $\Delta H/2$ vs FWHM plots with implicit parameter of temperature for H||b- and c-axis are shown in Fig.4.2.11(a) and Fig.4.2.11(b), respectively. In the T-range between 15K and 100K, $\Delta H/2$ is proportional to FWHM. This fact reveals that the increase of $\Delta H/2$ and FWHM may be attributed to the same origin.

As shown in Fig.4.2.12, the increase of ΔH/2 and FWHM for H||b-axis are found below 100K in Y(0.25) where Y^{3+} is substituted for Sr^{2+} in Sr14-B. The T-dependence of $(\Delta H/2)_b$ in Y(0.25) (open diamond) is compared with that in Sr14-B (solid circle) in Fig.4.2.13. In spite of substituting a small amount of Y^{3+}, $(\Delta H/2)_b$ in Y(0.25) decreases drastically than that in Sr14-B. The T-dependence of $(FWHM)_b$ in Y(0.25) (open diamond) as compared with those in Sr14-A (open circle) and Sr14-B (solid circle) is shown in Fig.4.2.14. In contrast with $(\Delta H/2)_b$, there found no remarkable difference between the T-dependence of $(FWHM)_b$ in Y(0.25) and that in Sr14-B.

4.2.3 Knight shift

The frequency variation of the ladder-^{63}Cu center line NMR spectrum at 200K in Sr14-A is shown in Fig.4.2.15. It is evident in Fig.4.2.15(a) at f=77.1MHz that two signals are overlapping with each other. Each signal is expressed by a gaussian curve with the dashed line and labeled as I or II. The lineshape is well fitted by a solid curve which is composed of gaussian curves of the signal I and II. Knight shift and FWHM are obtained from the signal I. The shift of the signal II arises from the twin of the single crystal Sr14-A which is described in **4.2.1**. The signal II is affected by the second order quadrupole effect. It is found in eq.(4.4) that the second order quadrupole effect can be eliminated by extrapolating $1/(^{63}\gamma_n H_{res})^2$ to zero in $(\omega - {}^{63}\gamma_n H_{res})/{}^{63}\gamma_n H_{res}$ vs $1/(^{63}\gamma_n H_{res})^2$ plot in Fig.4.2.16. The resonance frequency dependence of the signal I and the signal II for H||b-axis at 200K are indicated with solid and open circles, respectively. The slope is always positive as far as using the approximation expressed in eq.(4.4). Although the negative slope is a puzzle, it is too complex to solve the eq.(2.14). $(\omega - {}^{63}\gamma_n H_{res})/{}^{63}\gamma_n H_{res}$ against $1/(^{63}\gamma_n H_{res})^2$ for H||a-axis at 130K is plotted with solid or open squares. And $(\omega - {}^{63}\gamma_n H_{res}{}^{63})/\gamma_n H_{res}$ against $1/(^{63}\gamma_n H_{res})^2$ for H||c-axis at 130K is plotted with solid diamonds.

The T-dependence of the ladder-^{63}Cu Knight shift K_a for H||a-axis (open square), K_b for H||b-axis (solid circle) and K_c for H||c-axis (solid diamond) are shown in Fig.4.2.17(a). K_a and K_c are similar, while K_b is larger. The orbital (Van Vleck) part of the Knight shift, K_{orb}, and the hyperfine coupling constant cause this anisotropy. We can regard the spin part of the Knight shift, K_s, at 0K as zero for the spin singlet ground state. ${}^{63}K_{a.orb}$, ${}^{63}K_{b,orb}$ and ${}^{63}K_{c,orb}$ are assumed to be 0.27%, 0.30% and 1.34%, respectively. ${}^{63}K_{a,orb}$ and ${}^{63}K_{c,orb}$ against ${}^{63}K_{b,orb}$ with implicit parameter of temperature are plotted in the inset of Fig.4.2.17(a). The ratio of ${}^{63}K_b/{}^{63}K_a$ and ${}^{63}K_b/{}^{63}K_c$ are estimated to be -1.95 and -2.00, respectively. The spin part, ${}^{63}K_{b,s}(T)$=${}^{63}K_b(T)$-${}^{63}K_{b.orb}$, is shown in Fig.4.2.17(b). $-{}^{63}K_{b,s}(T)$ is well fitted by the following equation derived by Troyer et al. [11]

$$K_s \sim \chi_s \sim \frac{1}{\sqrt{T}} exp\left(-\frac{\Delta}{T}\right) \tag{4.5}$$

with Δ_A=550±30K. The magnitude of the spin gap is larger than that in $SrCu_2O_3$ [1, 2]. $K_{\alpha,s}(\alpha = a, b, c)$, is expressed as

$$\begin{aligned} K_{\alpha,s} &= \sum_j \frac{A_\alpha^{ij}}{N g_e \gamma_e \gamma_n \hbar^2} \chi_{\alpha,s} \\ &= \sum_j \sum_{\mathbf{q}} \frac{A_\alpha^{ij}(\mathbf{q}) e^{i\mathbf{q}\cdot\mathbf{r}_j}}{N g_e \gamma_e \gamma_n \hbar^2} \chi_{\alpha,s}, \end{aligned} \tag{4.6}$$

where $\mathbf{q}$ and $A_\alpha^{ij}(\mathbf{q})$ are the wave vector and the Fourier component of the hyperfine coupling constant, respectively. By assuming the supertransferred hyperfine interaction with the adjacent Cu spins, the hyperfine coupling constant, $A_\alpha(\mathbf{q})$, is expressed with the anisotropic on-site hyperfine coupling constant, A_α, and the isotropic supertransferred hyperfine coupling one, B, as [12]

$$A_\alpha(\mathbf{q}) = A_\alpha + 2B^c \cos q_c c + B^a \cos q_a a, \tag{4.7}$$

where a and c are the Cu-Cu distance along the a- and c-axis, respectively. The hyperfine coupling constant at $\mathbf{q}$=(0,0) is expressed as

$$A_\alpha(0) = A_\alpha + 2B^c + B^a \tag{4.8}$$

Since the spin magnetic susceptibility is isotropic, the anisotropy of K_s depends on that of the hyperfine coupling constant. $K_{b,s}$ is connected with $K_\alpha(\alpha$=a and $c)$ as [12]

$$\begin{aligned} K_b(T) &= K_{b,s} + K_{b,orb} \\ &= \frac{A_b(0)}{N g_e \gamma_e \gamma_n \hbar^2} \chi_s + K_{b,orb} \\ &= \frac{A_b(0)}{A_\alpha(0)} (K_\alpha(T) - K_{\alpha,orb}) + K_{b,orb}. \end{aligned} \tag{4.9}$$

$A_b(0)/A_a(0) \simeq A_b(0)/A_c(0) \simeq -2$ is obtained.

The T-dependence of $K_{b,s}$ in Sr14-A (open circle), Sr14-B (solid circle) and Y(0.25) (open diamond) are shown in Fig.4.2.18. Since the NMR spectrum begins to split below 100K in Sr14-B and Y(0.25), $-K_{b,s}$ is plotted above 100K. Δ_B=500±40K in Sr14-B and $\Delta_{(Y0.25)}$= 550±30K in Y(0.25) are estimated.

4.2.4 nuclear spin-lattice relaxation rate

The T-dependence of $1/T_1$ in Sr14-A and Sr14-B are shown in Fig4.2.19 in logarithmic scales. Open circles and squares correspond to $1/T_1$ in Sr14-A for H||b-axis, $(1/T_1)_{A,b}$, at f=125.1MHz. Open circles are results which are well fitted by the theoretical recovery function of eq.(2.27) as shown in Fig.4.2.21(a1). On the contrary, open squares was decided tentatively in the range of $R_{NMR}(t)$ between 1 and 0.1 due to the deviation from eq.(2.27) as shown in Fig.4.2.21(a2). $(1/T_1)_{A,b}$ indicated by open squares below 200K is distributed. $(1/T_1)_{B,b}$ in Sr14-B, at f=125.1MHz is plotted in the same manner as that in Sr14-A. Although $(T_1)_{B,b}$ is decided uniquely by the theoretical recovery function eq.(2.27) above 200K (solid circle), but not below 200K (solid square). In NQR measurements, T_1 is obtained uniquely by the eq.(2.27) above 180K (solid diamond) as shown in Fig.4.2.21(b1), but not below180K. T_1-rate in NQR, $(1/T_1)_Q$, is indicated with the short T_1 component (up triangle) and the long one (down triangle) below 180K as fitted in Fig.4.2.21(b2), while the vertical bar is not the error bar but the distribution of $(1/T_1)_Q$.

In the two-leg spin-ladder system, $1/T_1$ shows an activated T-dependence. The magnitude of the spin gap is estimated by the following function [11] as

$$\frac{1}{T_1} \sim exp\left(-\frac{\Delta}{T}\right) \tag{4.10}$$

at $T \ll \Delta$. The magnitude of the spin gap are estimated to be $\Delta_{A,M}$=830K in for Sr14-A in NMR, $\Delta_{B,M}$=1080K for Sr14-B in NMR and $\Delta_{A,Q}$=620K in NQR, respectively. The Arrhenius plots of T_1 against $1/T$ in semi-logarithmic scale are shown in Fig.4.2.20. In general, the nuclear relaxation in the 1D spin-chain and spin-ladder systems with the spin gap occurs dominantly via the two-magnon Raman process, in which a thermally excited magnon $|k, \sigma\rangle$ scatters into a state $|k+q, \sigma'\rangle$ by the hyperfine interaction accompanied by the nuclear spin flop. Although the equal-time antiferromagnetic (AF) spin correlations have a maximum at $\mathbf{q} = (\pi, \pi)$, these fluctuations do not contribute since they have a large energy gap. At low temperatures the main contributions arise from $k_x \sim \pi$ along the chain with requirement of energy conservation law, where $\mathbf{q} \approx (0,0)$ [11]. In such a case, due to the diffusive spin dynamics near $\mathbf{q} \approx (0,0)$, $1/T_1$ was shown to follow the field (resonance frequency) dependence of $H^{-1/2} \sim \omega^{-1/2}$ [13, 14]. Furthermore, in most gapped systems, the spin gap, Δ_{T_1}, deduced from the activation low of $1/T_1$ is by 1.4~1.8 times larger than that from the magnetic susceptibility or the Knight shift, Δ_χ [2, 14, 15, 16, 17]. This fact actually promoted theoretical considerations, which have then predicted to be $\Delta_{T_1} \simeq \sqrt{3}\Delta_\chi$ in the high temperature region [18] and $\Delta_{T_1} = 1.5\Delta_\chi$ even at low temperatures [19].

Takigawa et al. clarified that the EFG fluctuation contributes to the spin-lattice relaxation below 200K [20]. $(1/T_1)_Q$ is given by the spectral density of EFG fluctuations at the NQR frequency ω_0 and expressed by assuming an exponential correlation function as

$$\left(\frac{1}{T_1}\right)_Q = K \frac{2\tau_c}{1+(\omega_0 \tau_c)^2}, \tag{4.11}$$

where $1/\tau_c$ is the inverse correlation time of EFG fluctuations and the constant K is determined by the maximum value of $(1/T_1)_Q$. And they concluded that a broad maximum around 100K of $(1/T_1)_Q$ is due to the temperature variation of $1/\tau_c$. Since the recovery function $R(t)$ is given by the relaxation process due to the magnetic interactions, the experimental recovery curve deviates from the theoretical one below 200K as shown in Fig.4.2.21.

In NMR measurements, $1/T_1$ in Sr14-A and Sr14-B show the steep peak around 15~20K. Although the EFG fluctuations are considered to contribute the nuclear spin lattice relaxation below 200K, the experimental results are fitted by the theoretical recovery function of eq.(2.27). The magnetic interactions contribute the nuclear spin lattice relaxation 15~20K. Furthermore the spin-spin relaxation rate in Sr14-B due to the T_1 process, T_{2L}, derived from the decay of the spin echo intensity shows the steep peak around 15-20K in Fig.4.2.22(a). On the other hand $1/T_{2L}$ in Sr14-A increases gradually with decreasing temperature, while it was not measured below 20K because the ladder spin echo signal overlaps with the chain(+2) one. Judging from the temperature dependence of $1/T_{2L}$ in NQR for Sr14-A, it decreases with decreasing temperature below 20K. Thus $1/T_{2L}$ in the NMR measurement for Sr14-A is supposed to decrease with decreasing temperature below 20K. T_{2L} is obtained by eq.(2.34) with T_{2L} and T_{2G} as the fitting parameters. The decay of the spin echo intensity in Sr14-B at 20K is fitted by a single exponential decay function as shown in Fig.4.2.22(b1). In contrast, the decay in Sr14-A at 20K is fitted by eq.(2.34) as shown in Fig.4.2.22(b2).

4.2.5 Gausian spin-spin relaxation rate

The Gaussian spin-spin relaxation rate in copper oxides is dominated by the indirect nuclear spin coupling through electron excitations [21]. $1/T_{2G}$ is generally derived as [22, 23]

$$\left(\frac{1}{T_{2G}}\right)^2 = \frac{p\gamma_n{}^4\hbar^2}{8\mu_B^2}\left[\sum_q A_\alpha^4(\pi)\chi^2(q) - \left\{\sum_q A_\alpha^2(\pi)\chi(q)\right\}^2\right], \tag{4.12}$$

where $\chi(q) = Re\chi(q,0)$ is the static susceptibility. α is the direction of the magnetic field and p is the natural abundance of the Cu isotope. In $SrCu_2O_3$, $1/T_{2G}$ was reported to exhibit the weak T-dependence followed by the saturation at low temperature [2, 3]. The ladder-^{63}Cu spin echo decay for H||b-axis was measured on the center line at 125.1MHz. The experimental results are fitted by eq.(2.33) with T_{2L} and T_{2G} as the fitting parameters. The T-dependence of $1/T_{2G}$ in Sr14-A is shown in Fig.4.2.23(a). $1/T_{2G}$ increases gradually with decreasing temperature and saturates below 200K. $1/T_{2G}$ in Sr14-B shows the same T-dependence in Sr14-A above 200K. The decay of the spin echo intensity fitted by eq.(2.33) in Sr14-B is shown in Fig.4.2.23(b).

4.3 Experimental Results in the CuO_2 Chain Site

In this section, the results in Cu-NMR/NQR measurements are described. There exist inherent six holes in $Sr_{14}Cu_{24}O_{41}$. And almost all of them are supposed to localize in the CuO_2 chain. It is considered that holes should be doped into the $2p$ orbitals on the four oxygen sites surrounding a Cu site and the spin of the hole forms the Zhang-Rice(ZR) singlet [24] with the central Cu spin. The Cu site forming the ZR singlet is considered to be non-magnetic. In this text, the ZR singlet Cu sites and S=1/2 Cu ones are called as chain(+3) and chain(+2), respectively.

4.3.1 NMR/NQR spectrum

The ladder- and chain(+3)-^{63}Cu center line NMR spectrum for H||b-axis at T=30K and f=125.1MHz in Sr14-A is shown in Fig.4.3.1. The chain(+3)-Cu signal splits in the temperature range between 30K and 180K. The chain(+3)-Cu signal on the higher and the lower magnetic field are named as α and β, respectively as shown in Fig.4.3.1. The T-variation of the chain(+3)-^{63}Cu center line NMR spectrum is shown in Fig.4.3.2.

The T-variation of the chain(+3)-Cu NQR spectrum is shown in Fig.4.3.3. α and β sites are assigned by the experimental results of the spin-lattice relaxation time (T_1) because T_1 is more magnetic in the β-site. The highest frequency α site at 34.15MHz does not shift with increasing temperature and its intensity decreases. It is supposed that the width of the NQR spectrum decreases with decreasing temperature due to the formation of the spin singlet.

The spin echo signal of the chain(+2) signal is also identified by Takigawa et al [20]. The T-dependence of the chain(+2)-^{63}Cu in Sr14-A for H||b-axis is shown in Fig.4.3.4, denoted by an arrow. The chain(+2)-^{63}Cu shifts rapidly with increasing temperature. The spin-echo signal of the chain(+2)-Cu site becomes to be difficult to be detected with increasing temperature. It is invisible above 30K.

4.3.2 Knight shift

The T-dependence of the spin part of the chain-^{63}Cu Knight shift for H$\|$b-axis, $K_{b,s}$, in Sr14-A is shown in Fig.4.3.5. $K_{b,s}(+3\alpha)$ for the chain$(+3\alpha)$-Cu site and $K_{b,s}(+3\beta)$ for the chain$(+3\beta)$-Cu one are expressed with down and up triangles, respectively, in the T-range between 30$\sim$180K, while the chain(+3) signal with the solid diamond in other temperature range. And $K_{b,s}(+2)$ for the chain(+2)-Cu site is expressed with the solid circle. $K_{b,s}(+3\beta)$ is well fitted by the dimer model expressed as [5]

$$K_s \sim \chi_D \sim \frac{1}{T} \cdot \frac{1}{3 + exp(\Delta/T)} \tag{4.13}$$

with the magnitude of the spin gap of Δ=127K. In contrast, $K_{b,s}(+3\alpha)$ decreases gradually with decreasing temperature below 180K and shows the rapid falling into zero below 80K. $K_{b,s}(+2)$ is fitted by eq.(4.3) with Δ=106K below 30K as shown in the inset of Fig.4.3.5.

$K_{b,s}(+3\beta)$ in Sr14-B(solid circle) exhibits the same T-dependence of that in Sr14-A. As far as the experimental results in the chain-Cu site are concerned, there found no significant difference between that in Sr14-A and in Sr14-B.

4.3.3 nuclear spin-lattice relaxation rate

The T-dependence of the NMR spin-lattice relaxation rate of the chain(+3)-^{63}Cu for H$\|$b-axis in Sr14-A is plotted in logarithmic scales as shown in Fig.4.3.7. T_1 was measured on the center line at 125.1MHz. Up and down triangles correspond to the chain(+3,β)- and the chain(+3,α)-^{63}Cu sites, respectively. $1/T_1$ shows an activated T-dependence. The Arrhenius plot of T_1 against $1/T$ is plotted in semi-logarithmic scales as shown in the inset of the Fig.4.3.7. The magnitude of the spin gap is estimated to be Δ=100K in the chain(+3,α) and be Δ=140K in the chain(+3,β) by using the eq.(4.10). Since an estimation is performed in ta narrow T-range, the magnitude of the spin gap in both Cu sites are not so accurate. But the magnitude of the spin gap derived from the $1/T_1$ is supposed to be consistent with that from the Knight shift.

The T-dependence of the NQR $1/T_1$ of the chain(+3)-^{63}Cu is plotted in logarithmic scales as shown in Fig.4.3.8. The Arrhenius plot of T_1 is shown in the inset of Fig.4.3.8. and the magnitude of the spin gap is estimated to be Δ=140K.

4.4 Discussion

4.4.1 magnetic field induced staggered magnetization in the two-leg ladder system

The occurrence of the magnetic field induced uniform staggered magnetization (SM) in the ladder-^{63}Cu NMR spectra in Sr14-B may raise a new problem in the quantum spin systems which have a singlet ground state. A lot of experimental and theoretical studies about the impurity effects on the singlet ground state such as Spin-Peierls, Halden and even-leg ladder systems have been performed. Regnault et al. first observed the coexistence of the antiferromagnetic (AF) long-range ordering and the dimerization in the Spin-Peierls system, $CuGe_{1-y}Si_yO_3$, with very small amount of disorder of y=0.007 by

the neutron scattering measurement [25]. The theoretical explanation for this unexpected feature has been proposed by Fukuyama et al. [26]. They indicate that the stabilization of the singlet ground state due to the quantum coherence is very susceptible to the randomness which results in the appearance of the staggered moments. Azuma et al. observed the long-range AF ordering in the non-magnetic impurity-Zn doped two-leg ladder system of $Sr(Cu_{1-x}Zn_x)_2O_3$ with even only 1% of Zn by the specific heat measurements [27]. The theoretical investigations on the AF ordering in $Sr(Cu_{1-x}Zn_x)_2O_3$ have been performed. Fukuyama et al. suggest that a non-magnetic impurity replacing a spin induces a staggered spin modulation in the S=1/2 AF Heisenberg two-leg ladder system, which has a spin gap if clean [28]. Cu-NMR/NQR measurements have been performed in $Sr(Cu_{1-x}Zn_x)_2O_3$ and $Sr_{1-x}La_xCu_2O_3$ by Ohsugi et al. [29]. They confirmed the existence of the long-range AF ordering from the broadening of Cu-NQR spectrum at 1.4K in 1 and 2% Zn substituted $SrCu_2O_3$. Furthermore, they observed the applied magnetic field induced the SM in La-substituted $SrCu_2O_3$, while the long-range magnetic ordering does not occur above 1.4K.

There are no impurities which cause the SM in Sr14-B, but there exist inherent holes. Most of holes are suggested to exist in the CuO_2 chain. Since only a few percent of non-magnetic impurities disturb the singlet ground state in the two-leg ladder system, holes doped into the two-leg ladder system are considered to induce the SM. Holes are doped into the four oxygen sites surrounding a Cu and form the Zhang-Rice(ZR) singlet with Cu S=1/2 spins. The Cu sites forming the ZR singlet regards as non-magnetic. Spin defects due to the ZR singlet are considered to play same role as the non-magnetic impurity of Zn in $Sr(Cu_{1-x}Zn_x)_2O_3$. The spin singlet ground state in the two-leg ladder system is shown in Fig.4.4.1(a) and the spin formation in the SM due to the defect of the spin in Fig.4.4.1(b) [28]. The SM due to the ZR-singlet in Sr14-B is sketched in Fig.4.4.2(b). Dagotto et al. predict that carriers doped into the two-leg ladder system do not scatter each other but make pairs on rungs not to break the spin singlet [30] as shown in Fig.4.4.2(a). It is supposed that the amount of holes in the two-leg ladder system in Sr14-B to be small and exist alone each other. On the contrary, holes in Sr14-A are supposed to make pairs as shown in Fig.4.4.2(a).

Considering the exponential decay of the SM size with a spin correlation length ξ, it is expressed at ℓ-th Cu site in the chain-A and B running along the c-axis with Cu-Cu distance of c ,respectively, as

$$S_\ell^A = \sum_{L,L'}\Big[(-1)^{L'-\ell}S_0'\{\theta^-(L'-\ell)+\theta^+(-L'+\ell)\}exp\Big\{-\frac{(L'-\ell)c}{\xi}\Big\} + (-1)^{L-\ell}S_0 exp\Big\{-\frac{(L-\ell)c}{\xi}\Big\}\Big] \tag{4.14}$$

$$S_\ell^B = \sum_{L,L'}\Big[(-1)^{L-\ell+1}S_0'\{\theta^-(L-\ell)+\theta^+(-L+\ell)\}exp\Big\{-\frac{(L-\ell)c}{\xi}\Big\} + (-1)^{L'-\ell+1}S_0 exp\Big\{-\frac{(L'-\ell)c}{\xi}\Big\}\Big] \tag{4.15}$$

$$\theta(x) = \begin{cases} 1 & (x>0) \\ 0 & (x\le 0) \end{cases}$$

where L and L' are the site number of unpaired spins and spin defects, respectively. The

shift of Cu at i-th site is expressed with the uniform shift proportional to the uniform susceptibility at and the alternative shift due to the SM via the hyperfine coupling as $K = K_u + K_{alt}$. The alternative part for the chain-A and -B are expressed as

$$(K^A_{alt})_i = (a_{hf}S^A_i + b_{hf}S^A_{i+1} + b_{hf}S^A_{i-1} + b_{hf}S^B_i)/\gamma_n\hbar H_0 \quad (4.16)$$

$$(K^B_{alt})_i = (a_{hf}S^B_i + b_{hf}S^B_{i+1} + b_{hf}S^B_{i-1} + b_{hf}S^A_i)/\gamma_n\hbar H_0. \quad (4.17)$$

The supertransferred hyperfine coupling, b_{hf}, is very small compared with the on site hyperfine coupling, a_{hf}, in the two-leg ladder system [12]. The broadening of a NMR spectrum due to the SM is shown schematically in Fig.4.4.3(a), where arrows indicate the distribution of K_{alt}.

It is difficult to explain the splitting of NMR spectra in Sr14-B by considering the SM due to localized holes, i.e. fixed spin defects. The model for the splitting and broadening of NMR spectra in Sr14-B is proposed schematically in Fig.4.3.3(b). It is remarkable that the SM are induced in rather uniform manner in the two-leg ladder in Sr14-B. It is speculated that the collective motion of holes may average out the SM. For instance, the collective motion of Charge-Density-Wave or the hopping of holes is suggested, since the resistivity is insulating. The increase of the average of spin, $\langle S \rangle$, with decreasing temperature, causes a increase of ΔH/2 below 100K. Since the motion of holes are supposed to be inactive with decreasing temperature, the SM begins to be distributed partially and FWHM increases. T-variation of the population of the staggered moments, $P(S)$, is shown in Fig.4.4.4.

Since Y^{3+} substitution for Sr^{2+} yields the random potential and decreases of the hole content, it is considered that holes easily localize. In Y(0.25), the temperature dependence of FWHM is similar to in Sr14-B but the fact that the ΔH/2 decreases remarkably may support this speculation.

4.4.2 dimerization in the CuO_2 chain

The dimerization in CuO_2 chain is strange because the bonding angle of Cu-O-Cu is nearly 90° for which ferromagnetic spin correlation is expected. Matsuda et al. confirmed that the dimers are formed between spins which are separated by 2 and 4 times the distance between the nearest-neighbor Cu ions [31].

In NMR measurements, it was clarified that there is a considerable difference in the magnetic properties between the chain(+3,α) and the chain(+3,β). Especially, the T-dependence of $-^{63}K_{b,s}$ in both sites as shown in Fig.4.3.5(a) are quite different. The T-dependence of $-^{63}K_{b,s}$(+3,β) below 100K is well explained by the noninteracting dimer model, but that of $-^{63}K_{b,s}$(+3,α) shows a different behavior. It is considered that the transferred hyperfine field from chain(+2)-Cu S=1/2 spins is the main contribution to $^{63}K_{b,s}$(+3) because of S=0 at Cu(+3) sites for the ZR-singlet. $-^{63}K_{b,s}$(+3) in the α-Cu site and the β -Cu one are expressed as

$$-^{63}K_{b,s}(+3,\alpha) = \frac{2B_\alpha}{N\gamma_n\gamma_e\hbar^2}\chi_s \quad (4.18)$$

$$-^{63}K_{b,s}(+3,\beta) = \frac{2B_\beta}{N\gamma_n\gamma_e\hbar^2}\chi_s, \quad (4.19)$$

where $2B_\alpha$ and $2B_\beta$ are the transferred hyperfine coupling constant at the α- and β-Cu sites. The experimental results of $-^{63}K_{b,s}$(+3) suggest that $2B_\alpha$ and $2B_\beta$ depend on

temperature. In spite of increase of χ_s in the temperature range of 80~180K as shown in Fig.4.1.3(b), $-^{63}K_{b,s}(+3,\alpha)$ decreases gradually. And it falls into zero rapidly below 80K with decreasing χ_s. This fact suggests the decreasing of $2B_\alpha$. T-dependence of the hyperfine coupling constants of B_α and B_β divided by B at 200K are shown in Fig.4.3.5(b). It is reasonable that the distance between Cu(+2) and Cu(+3,α) increases with decreasing temperature below 200K but that between Cu(+2) and Cu(+3,β) decreases. Thus the adjacent Cu(+2) shift to the inverse direction each other to approach Cu(+3,β). Matsuda et al. support the possibility of this idea by X-ray diffraction measurements [32]. Since the solid curve fitting $-^{63}K_{b,s}(+3,\beta)$ is obtained by using the experimental results below 100K and the hyperfine coupling constant, $2B_\beta$, is considered to increase below ~200K, a calculation is overestimated in the temperature range of 100~180K.

A ratio of the integrated intensity for the chain(+3,α) to that for chain(+3,β) is obtained to be about 1.2 from the NQR spectrum at 4.2K in Sr14-A. The dimerization model in CuO_2 chain as shown in Fig.4.4.4 is proposed by NMR/NQR measurements, which is consistent with the result of the inelastic neutron scattering measurement [31].

4.5 Conclusion

Comprehensive Cu NMR/NQR measurements have been performed on the single crystals of $Sr_{14}Cu_{24}O_{41}$ and $Sr_{13.75}Y_{0.25}Cu_{24}O_{41}$ containing the CuO_2 chain and the Cu_2O_3 two-leg ladder. By separating the Cu NMR/NQR spectra between the chain-Cu site and the ladder-Cu one. In thesé compounds, that holes are inherently doped plays an important role to disturb the quantum coherence in the singlet ground state in the two-leg ladder and to form dimers in the chain.

In the two-leg ladder, there exists the spin gap of about 500K which is larger than that in $SrCu_2O_3$. It is found that the magnetic field induces a staggered magnetization in Sr14-B below ~100K. The origin of the staggered moments is suggested to be attributed to unpaired holes. Although the antiferromagnetic long range ordering due to spin defects in the two-leg ladder system has been studied experimentally and theoretically, it has been shown in this study that the staggered moments are induced by unpaired holes. It is suggested taht holes do not localize to average out the staggered moments.

Since the peak of the NMR spin-lattice relaxation rate, $1/T_1$, around 15K does not depend on the magnetic field, it is not attributed to the fluctuations of impurity spins. The fluctuations of the staggered moments may cause the peak of $1/T_{2L}$ and $1/T_1$ around 15K because those in Sr14-B are steeper than those in Sr14-A as shown in Fig.4.2.22(a). The collective motion of holes are supposed to become dull with decreasing temperature, and holes may localize around 15K. The critical slowing down of spin-fluctuations is expected to cause the peak of $1/T_{2L}$ and $1/T_1$ around 15K. Although the splitting and broadening in Sr14-A are not observed, the motion of hole-pairs may be localized around 15K. The long-range magnetic ordering at low temperature is not evident. The magnetic moments are reduced due to the spin singlet correlations. The 3D magnetic interaction between ladder layers may be weak because non magnetic CuO_2 layers break off it due to the dimerization and ZR-singlet.

NMR/NQR measurements revealed the existence of the spin gap of 100~140K in the CuO_2 chain which had been suggested by the magnetic susceptibility measurement. The

unique dimerization model in the CuO_2 chain with nearly 90° Cu-O-Cu bond angle was proposed in this work.

REFERENCES

[1] M.Azuma, Z.Hiroi, M.Takano, K.Ishida and Y.Kitaoka; Phys.Rev. Lett.**73** (1994) 3463.

[2] K.Ishida, Y.Kitaoka, K.Asayama, M.Azuma, Z.Hiroi and M.Takano; J. Phys. Soc. Jpn. **63** (1996) 2827.

[3] K.Ishida, Y.Kitaoka, K.Asayama, M.Azuma, Z.Hiroi and M.Takano; Phys.Rev.B **53** (1994) 3222.

[4] M.Kato, H.Chizawa, Y.Koike, T.Noji, and Y.Saito; Physica C **235-240** (1994)1327.

[5] M. Matsuda and K. Katsumata; Phys. Rev. B **53**, (1996) 2201.

[6] M.Uehara et al. unpublished.

[7] E.M.McCarron, M.A.Subramanian, J.C.Calabrese and R.L.Harlow; Mat.Res.Bull. **23** (1988) 1355.

[8] T.Siegrist, L.F.Schneemeyer, S.A.Sunshine, J.V.Waszczak R.S.Roth; Mat.Res.Bull. **23** (1988) 1429.

[9] H.Yamane, Y.Miyazaki and H.Hirai; J.Ceramic Soc.Jpn. **98** (1994) 105.

[10] M.Uehara, T.Nagata, J.Akimitsu, H.Takahashi, N.Mo-ri and K.Kinoshita; J.Phys.Soc.Jpn. **65** (1996) 2764.

[11] M.Troyer, H.Tsunetsugu and D.Würtz; Phys.Rev.B **50** (1994) 13515.

[12] K.Magishi, S.Matsumoto, Y.Kitaoka, K.Ishida, K.Asayama, M.Uehara, T.Nagata and J.Akimitsu; submitted to Phys.Rev.B.

[13] L.van Hove; Phys.Rev. **95** (!954) 1374.

[14] M.Takigawa, T.Asano, Y.Ajiro, M.Mejata and Y.J.Uemura; Phys.Rev.Lett. **76** (1996) 2173.

[15] T.Shimizu, D.E.Maclaughlin, P.C.Hammel, J.D.Thompson and S-W.cheong ;Phys.Rev.B **52** (1995) R9835.

[16] H.Iwase, M.Isobe, Y.Ueda and H Yasuoka; J.Phys.Soc.Jpn. **65** (1996) 2397.

[17] Y.Furukawa, A.Iwai, K.Kumagai and A.Yakubovsky; J.Phys.Soc.Jpn. **65** (1996) 2393.

[18] J.Kishine and H.Fukuyama; J.Phys.Soc.Jpn. **66** (1997) 26.

[19] S.Sachdev and K.Damle; Phys.Rev.Lett. **78** (1997) 943.

[20] M.Takigawa, N.Motoyama, H.Eisaki and S.Uchida; to be published.

[21] C.H.Pennington, D.J.Durand, C.P.Slichter,J.P.Rice, E.D.Bukowski and D.M.Ginberg; Phys.Rev.B **39** (1989) 274: C.H.Pennington and C.P.Slichter; Phys.Rev.Lett. **66** (1991) 381

[22] D.Thelen and D.Pines;Phys.Rev.B. **49** (1994) 3528

[23] M.Takigawa;Phys.Rev.B **49** (1994) 4158

[24] F.C.Zhang and T.M.Rice; Phys.Rev.B **37** (1988) 3759.

[25] L.P.Regnault, J.P.Renard, G.Dhalenne and A.Recolevschi; Europhys.Lett. **32** (1995) 579.

[26] H.Fukuyama, T.Tanimoto, M.Saito;J.Phys.Soc.JPn **65** (1996) 1182.

[27] M.Azuma, Y.Fujishiro, M.Takano, M.Nohara and H.Tkagi.; Phys.Rev.B **55** (1997) R8658

[28] H.Fukuyama, N.Nagaosa, M.Saito and T.Tanimoto.;J.Phys.Soc.Jpn. **65** (1996) 2377.

[29] S.Ohsugi,Y.Kitaoka, K.Asayama, M.Azuma, Y.Fujishiro, Z.Hiroi and M.Takano.; now submitted.

[30] E.Dagotto, J.Riera and D.Scalpino.;Phys.Rev.B **45** (1992) 5744.

[31] M.Matsuda, K.Katsumata, H.Eisaki, N.Motoyama, S.Uchida, S.M.Shapiro and G.Shirane. Phys.Rev.B **54** (1996) 1.

[32] unpublished.

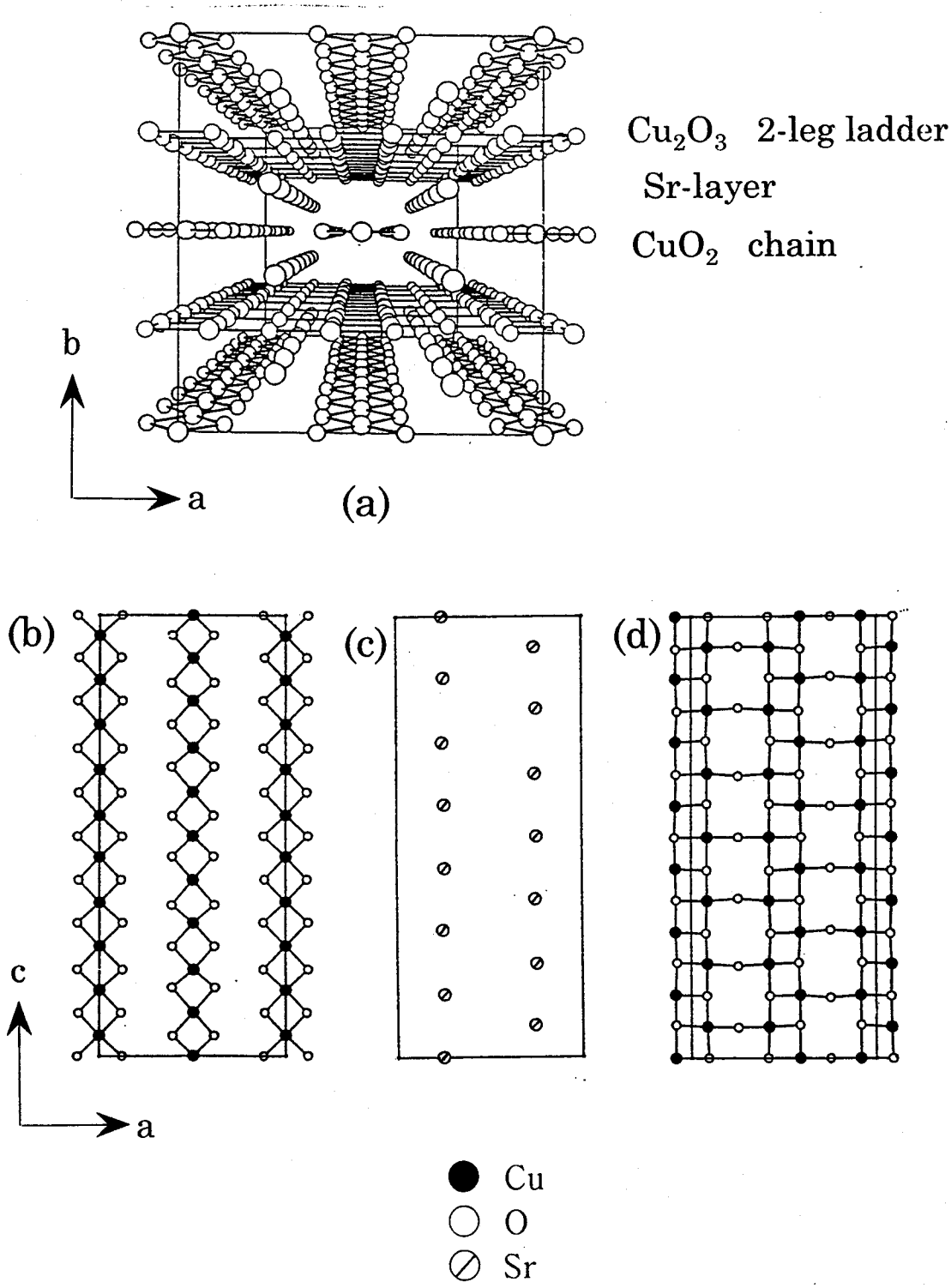

Fig.4.1.1 (a) Composite drawing of the complete $Sr_{14}Cu_{24}O_{41}$ structure[7]. (b) CuO_2 chain. (c) Sr layer. (d) Cu_2O_3 two-leg ladder layer.

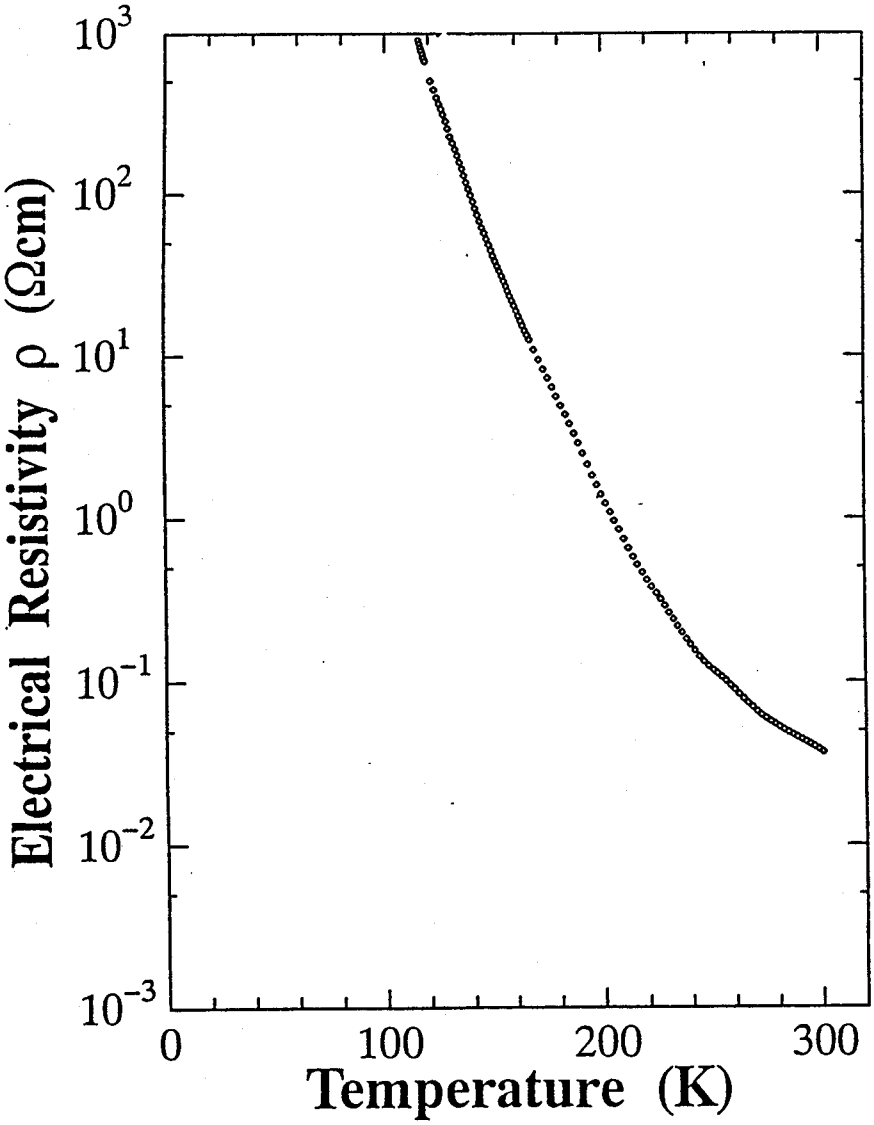

Fig.4.1.2 Temperature dependence of the resitivity in $Sr_{14}Cu_{24}O_{41}$[4].

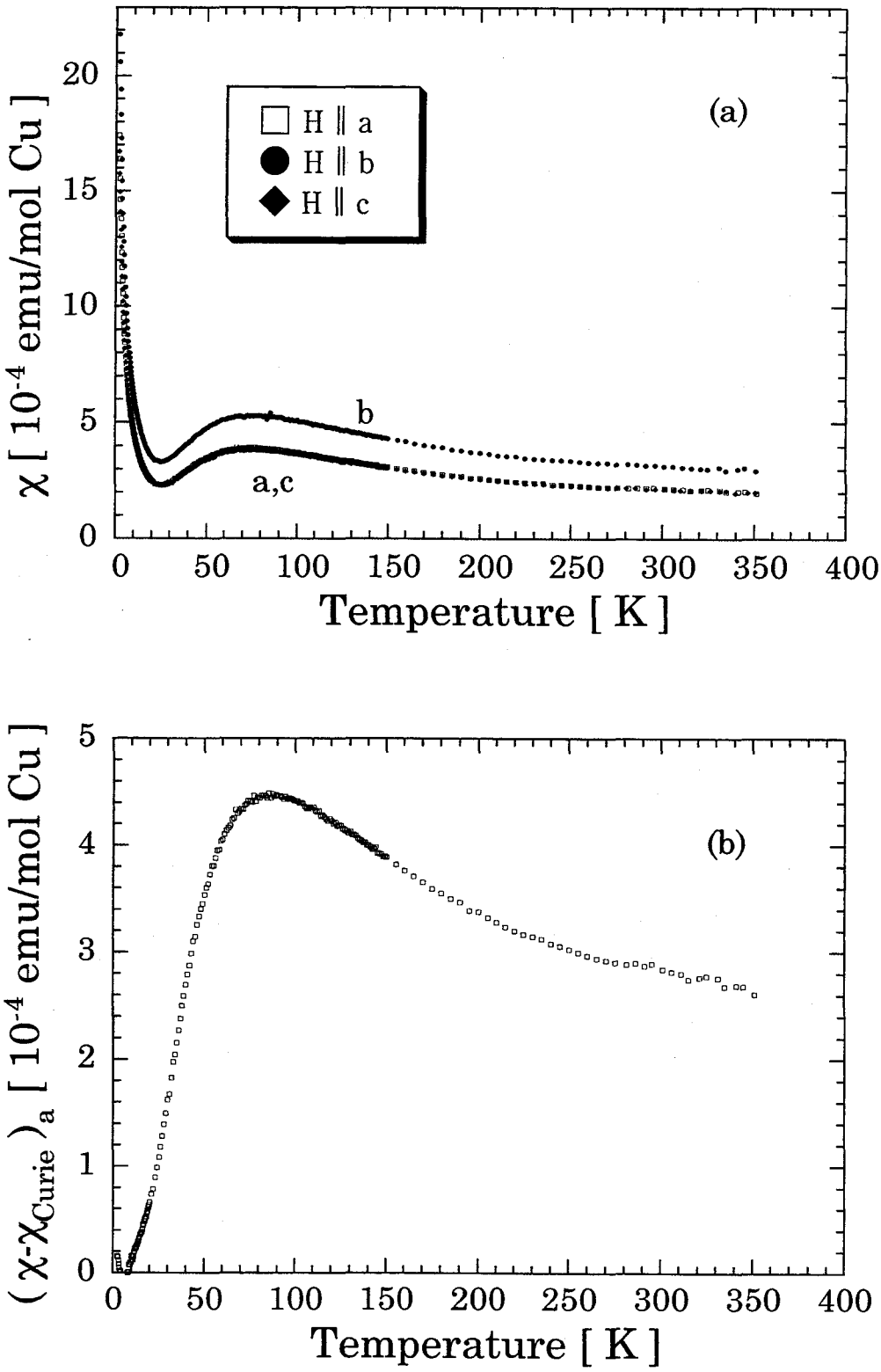

Fig.4.1.3 (a) Temperature dependence of the magnetic susceptibility, χ, in $Sr_{14}Cu_{24}O_{41}$[10]. (b)$\chi - \chi_{Curie}$ for H||a-axis.

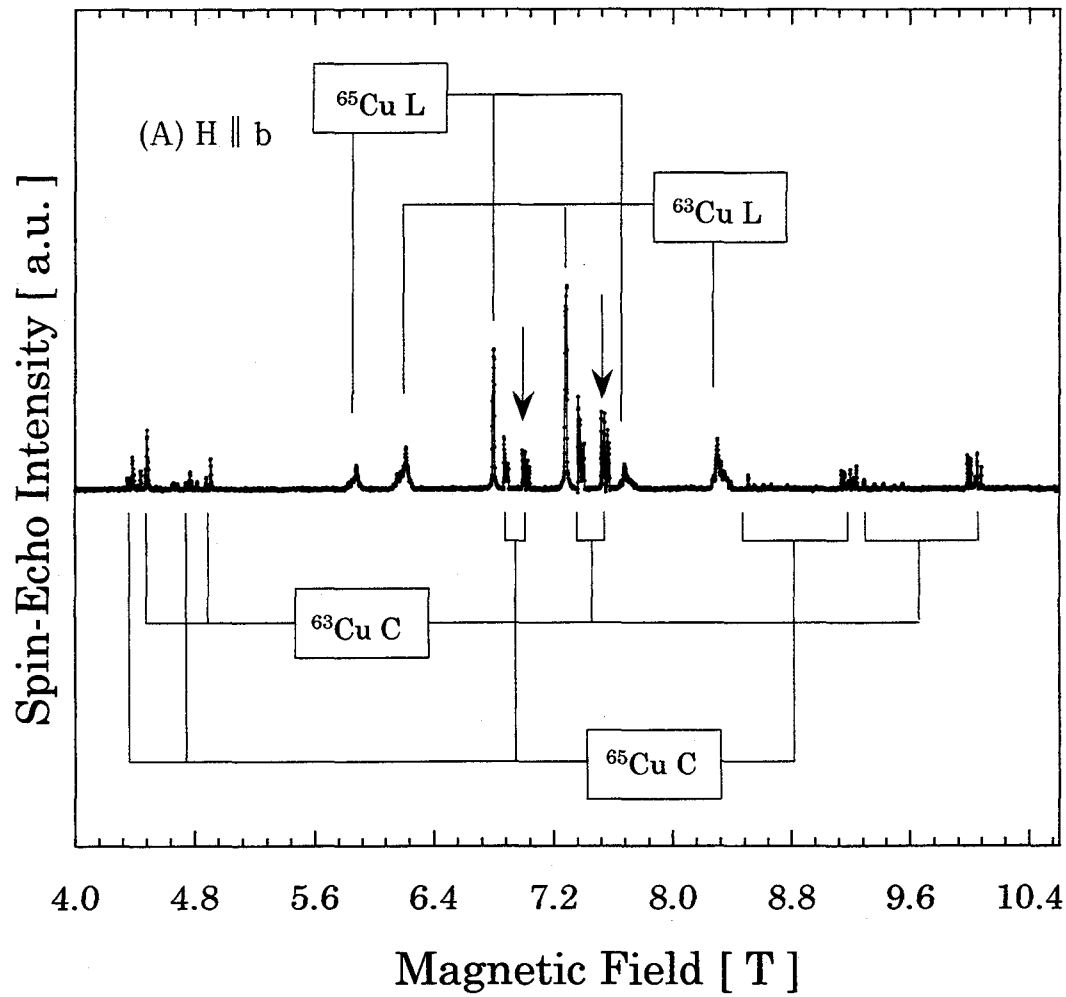

Fig.4.2.1 Ladder- and chain-Cu NMR spectra in Sr14-A and Sr14-B. (A) for H||b-axis at f=83.1MHz and T=30K in Sr14-A. (B1) for H||b-axis at f=83.1 MHz and T=60K in Sr14-B. (B2) for H||a-axis at f=125.1 MHz and T=20K in Sr14-B. (B3) for H||c-axis at f=125.1 MHz and T=60K in Sr14-B.

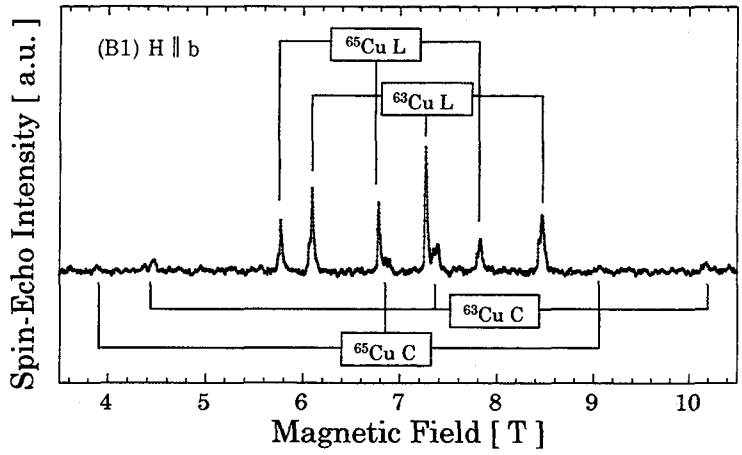

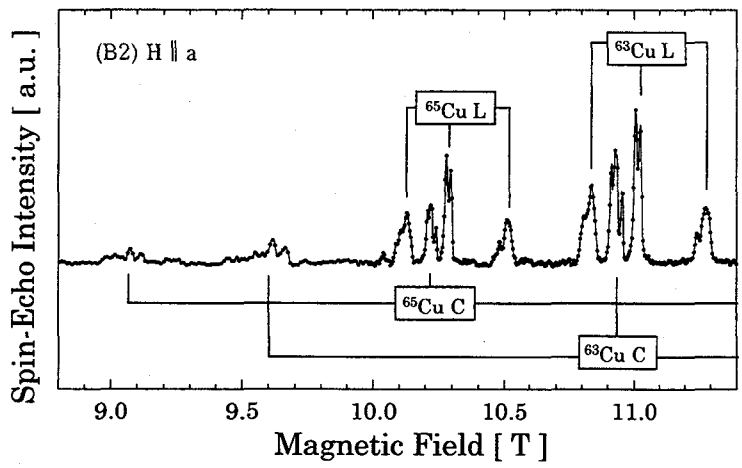

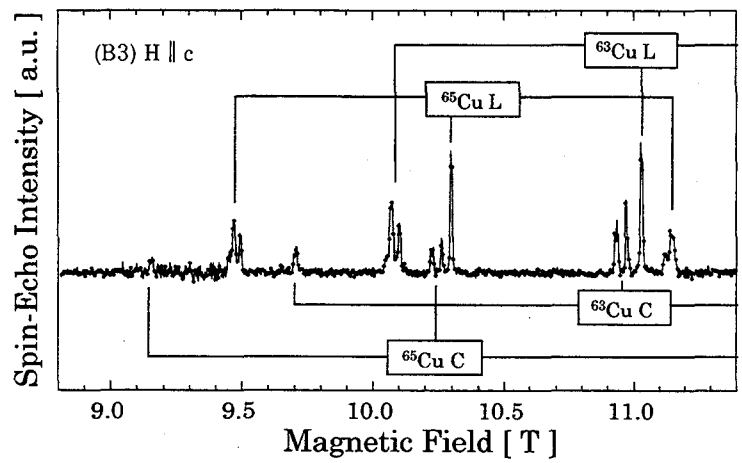

Fig.4.2.1 (B1),(B2),(B3).

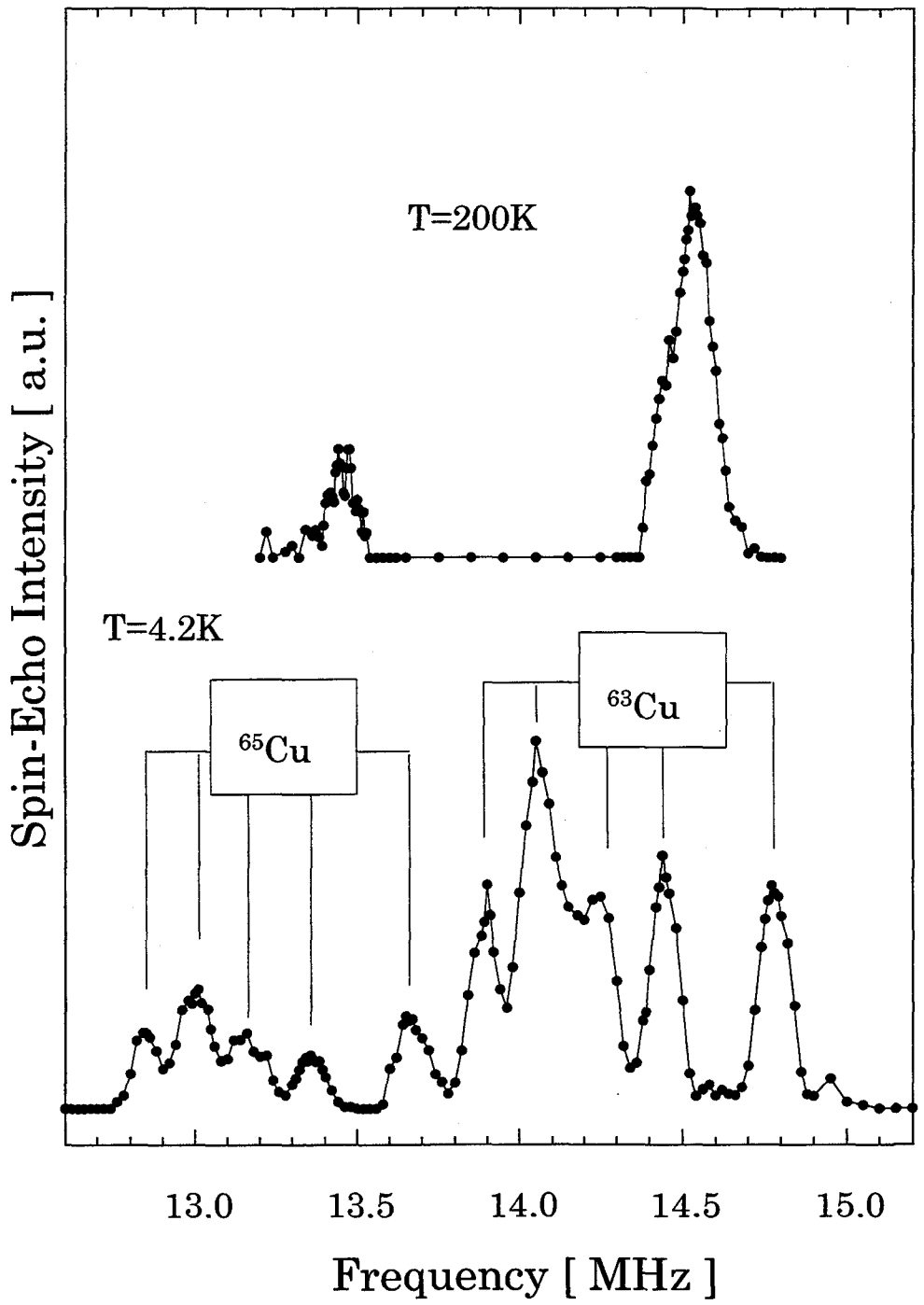

Fig.4.2.2 Temperature variation of the ladder-Cu NQR spectrum.

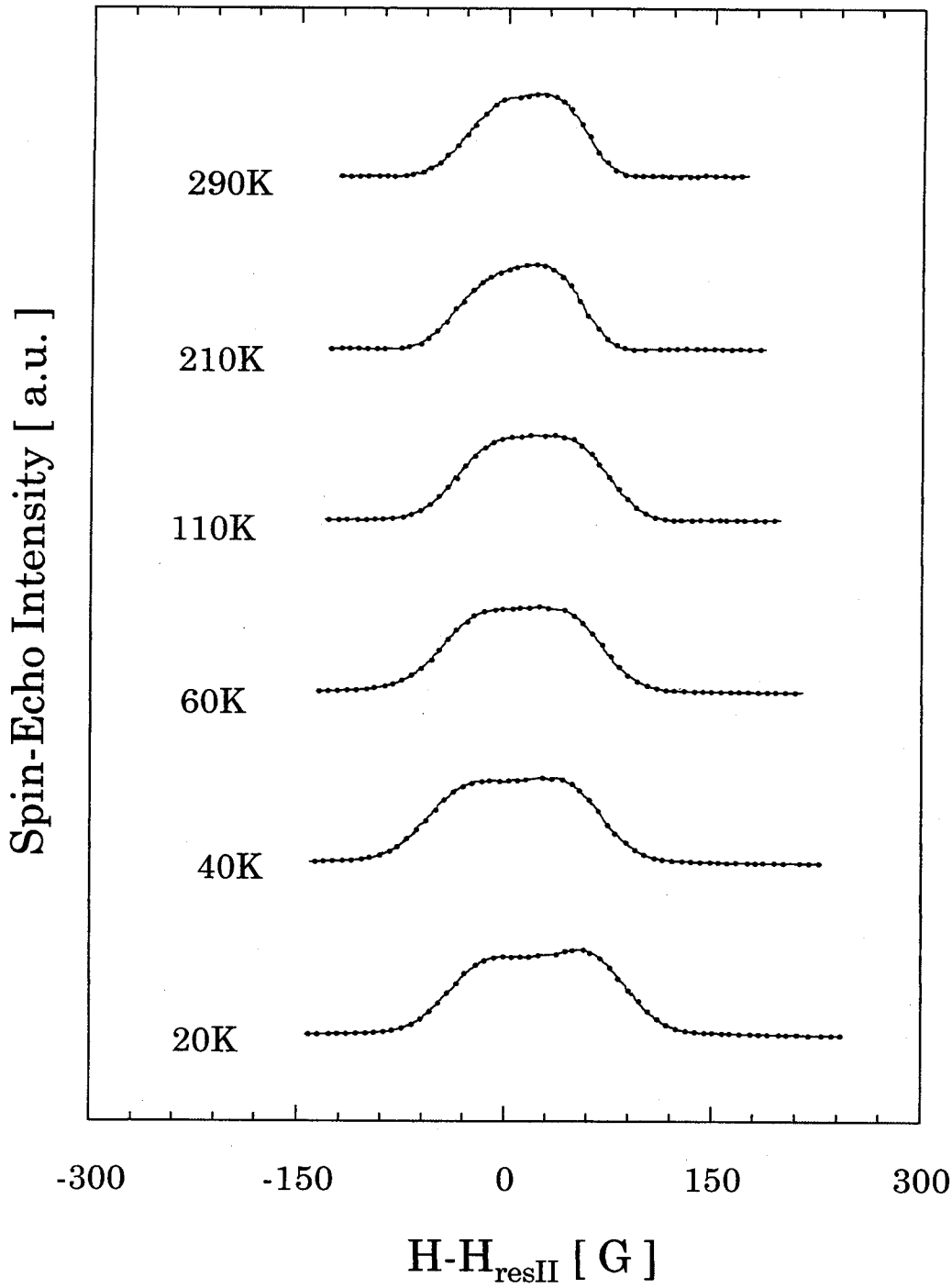

Fig.4.2.3 Temperature variation of the ladder-^{63}Cu center line NMR spectrum for H||b-axis at f=125.1MHz in Sr14-A.

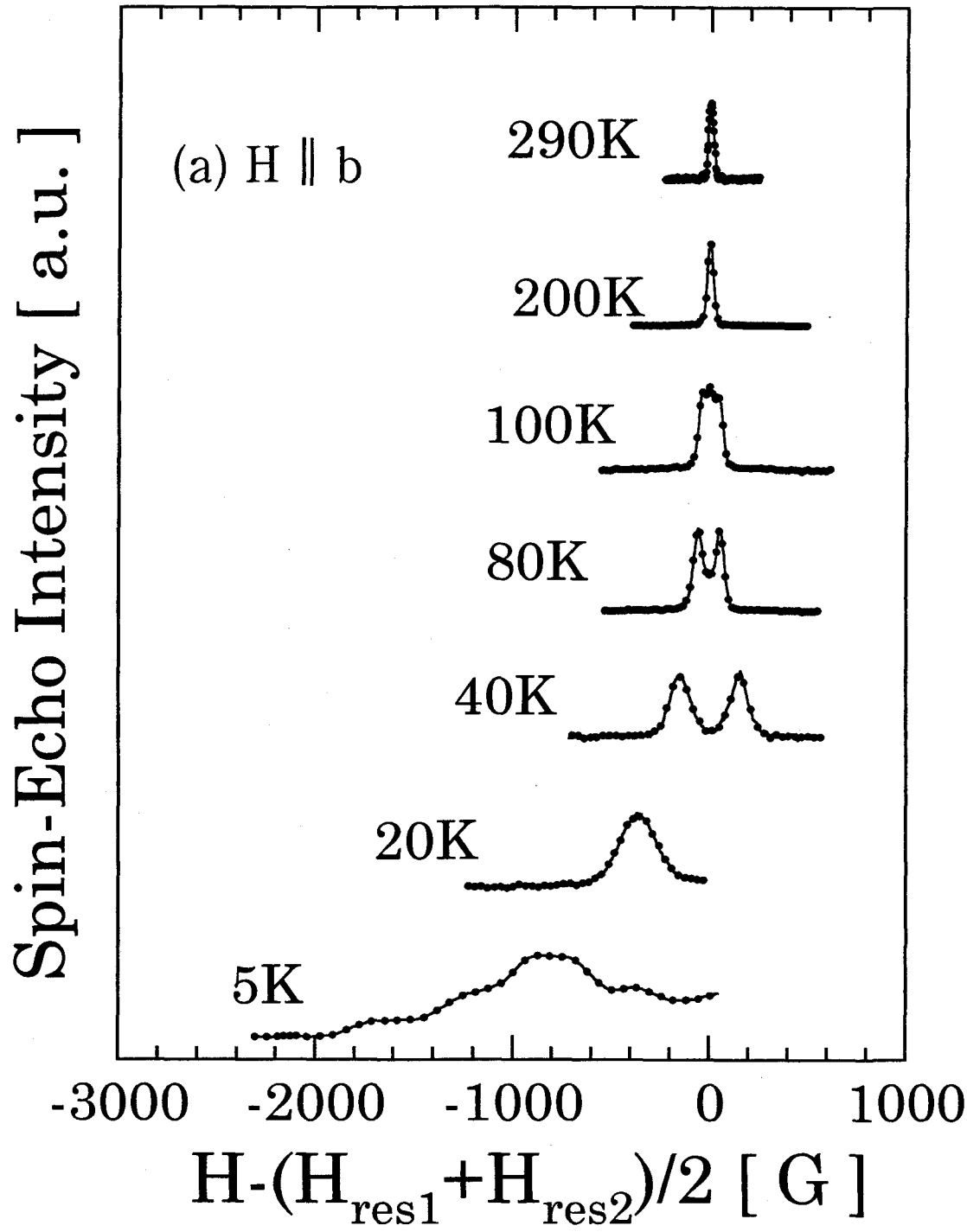

Fig.4.2.4 Temperature variation of the ladder-^{63}Cu center line NMR spectrum at f=125.1MHz in Sr14-B. (a) for H||b-axis. (b) for H||a-axis. (c) for H||c-axis.

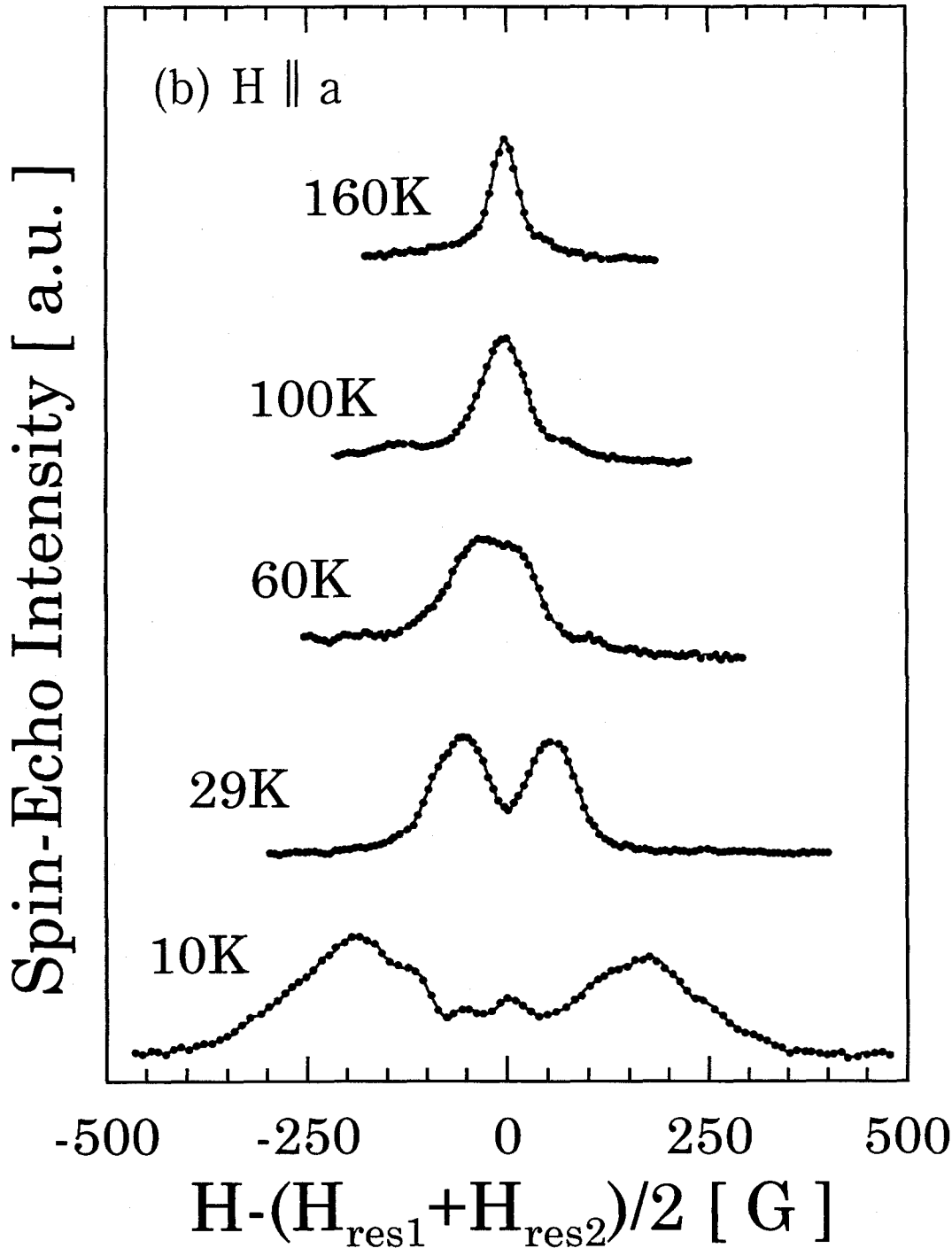

Fig.4.2.4 (b) for H||a-axis.

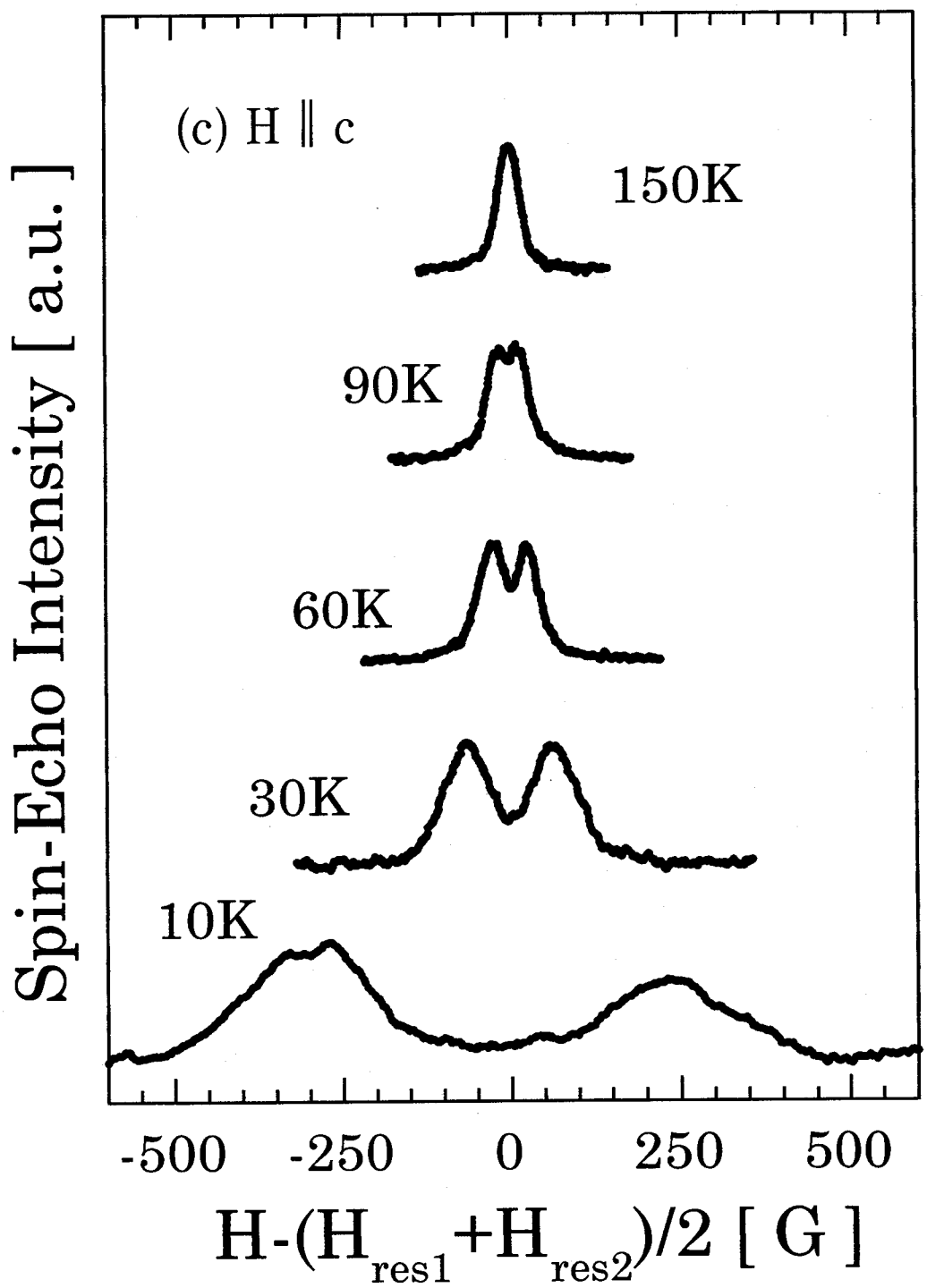

Fig.4.2.4 (c) for H∥c-axis.

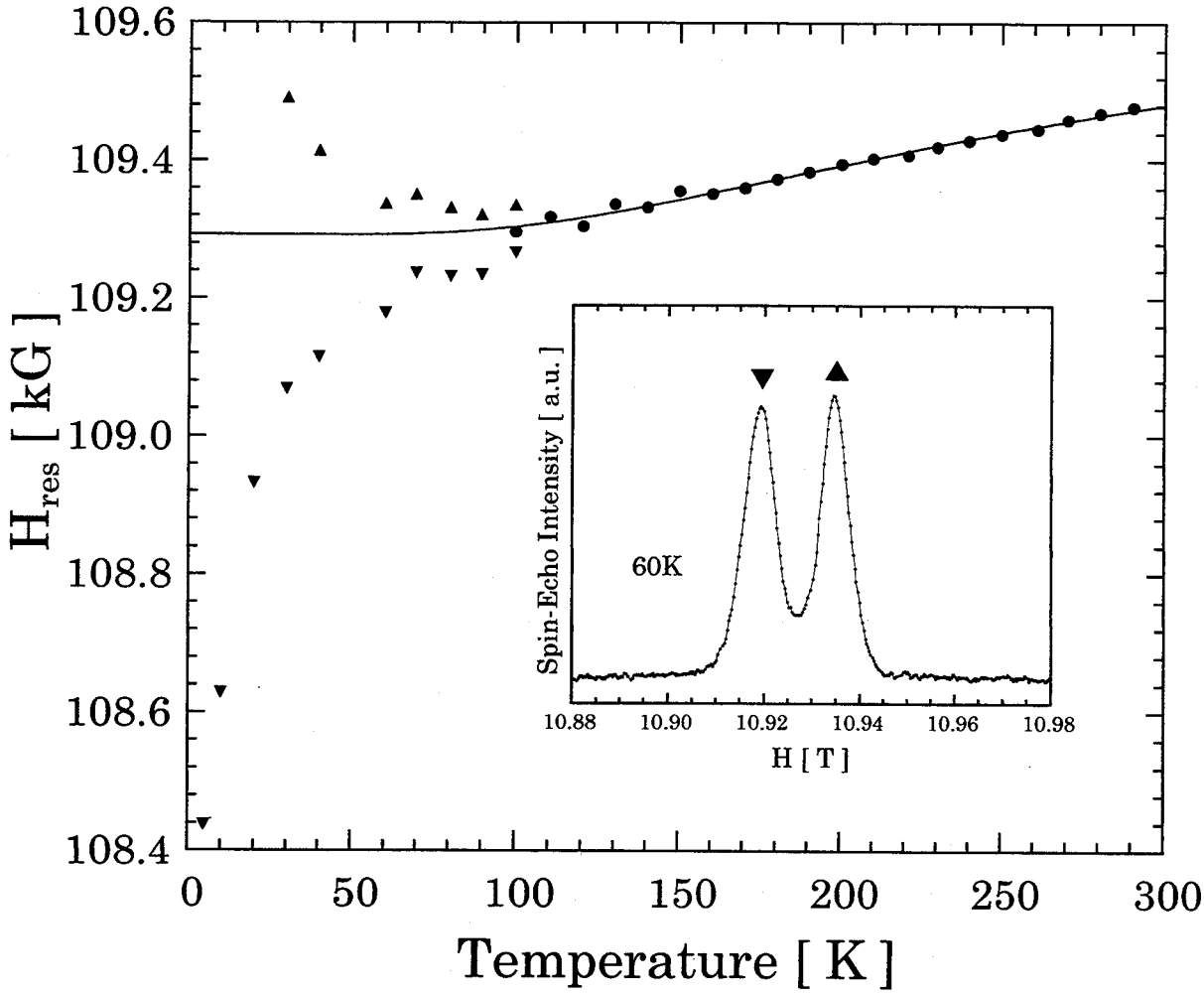

Fig.4.2.5 Temperature dependence of the ladder-^{63}Cu center line resonance magnetic field for H$\|$b-axis at f=125.1MHz in Sr14-B. The NMR spectrum at T=60K is shown in the inset where the up and the down triangle correspond to the higher(H_{res2}) and the lower resonance magnetic field(H_{res1}), respectively.

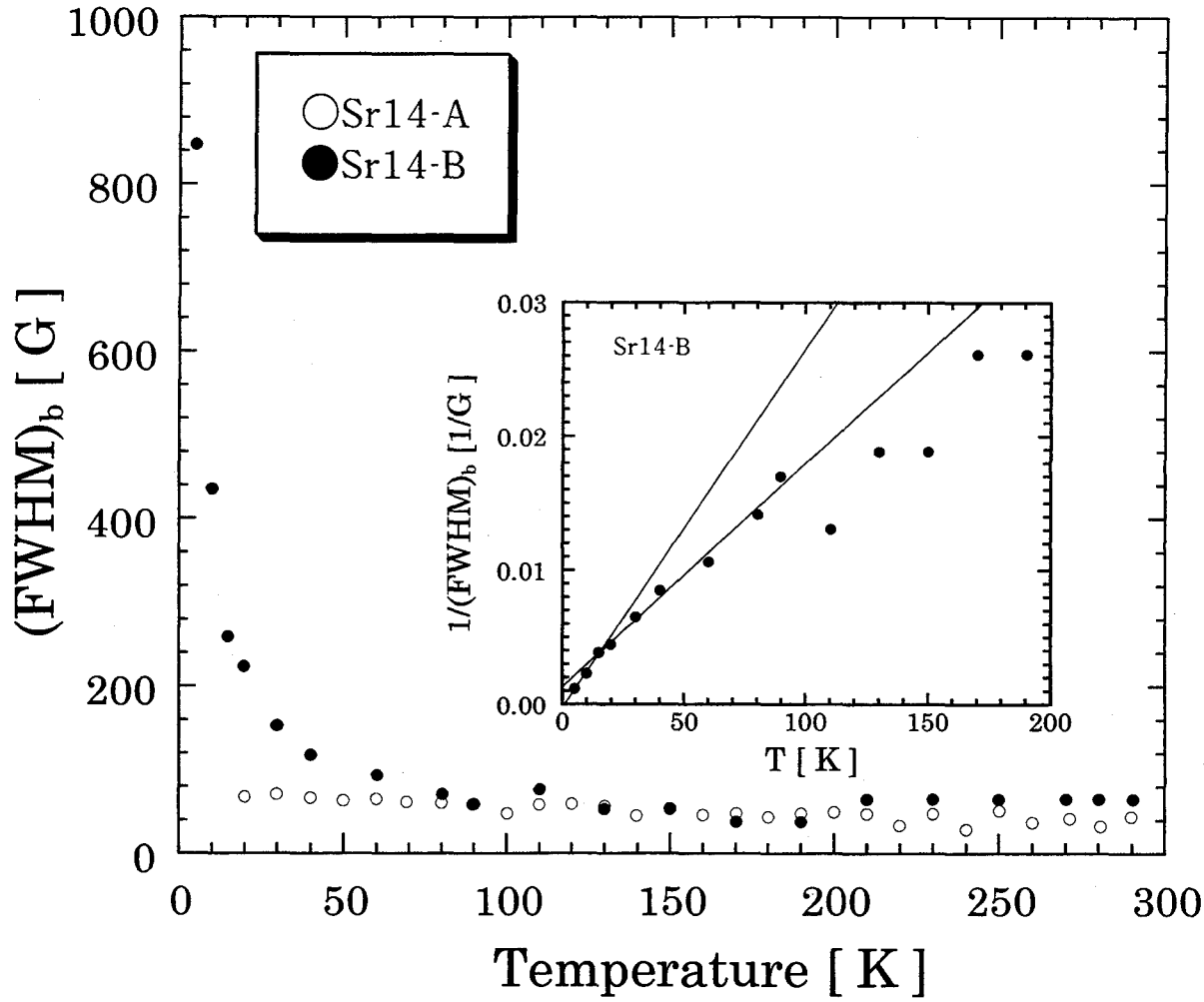

Fig.4.2.6 Temperature dependence of the FWHM for H||b-axis in Sr14-A and Sr14-B. Temperature dependence of $1/(\mathrm{FWHM})_b$ is shown in the inset.

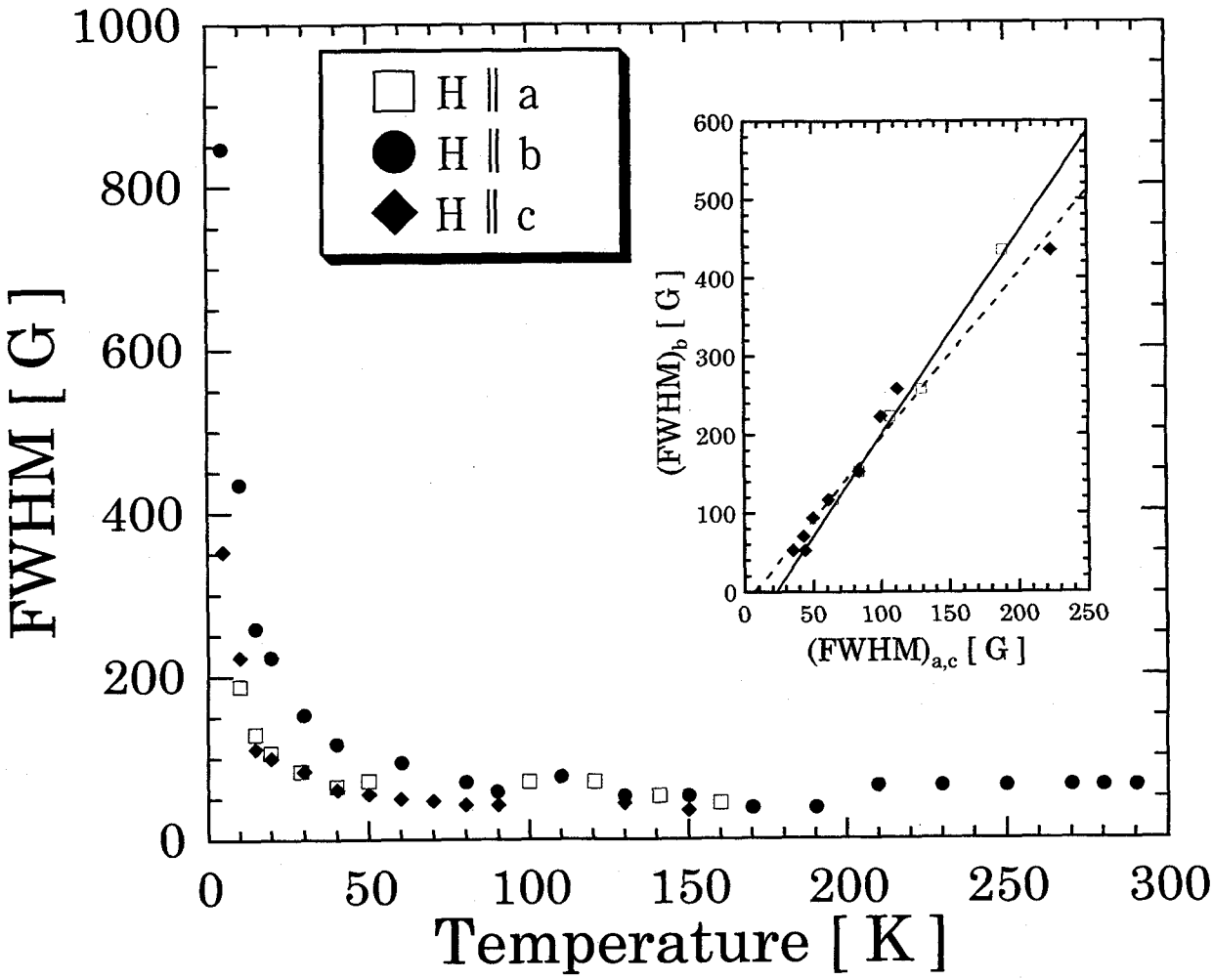

Fig.4.2.7 Temperature dependence of the ladder-^{63}Cu FWHM for H||a-,b- and c-axis at 125.1MHz in Sr14-B. $(FWHM)_{a,c}$ vs $(FWHM)_b$ with the implicit parameter of temperature at 125.1MHz in Sr14-B are shown in the inset.

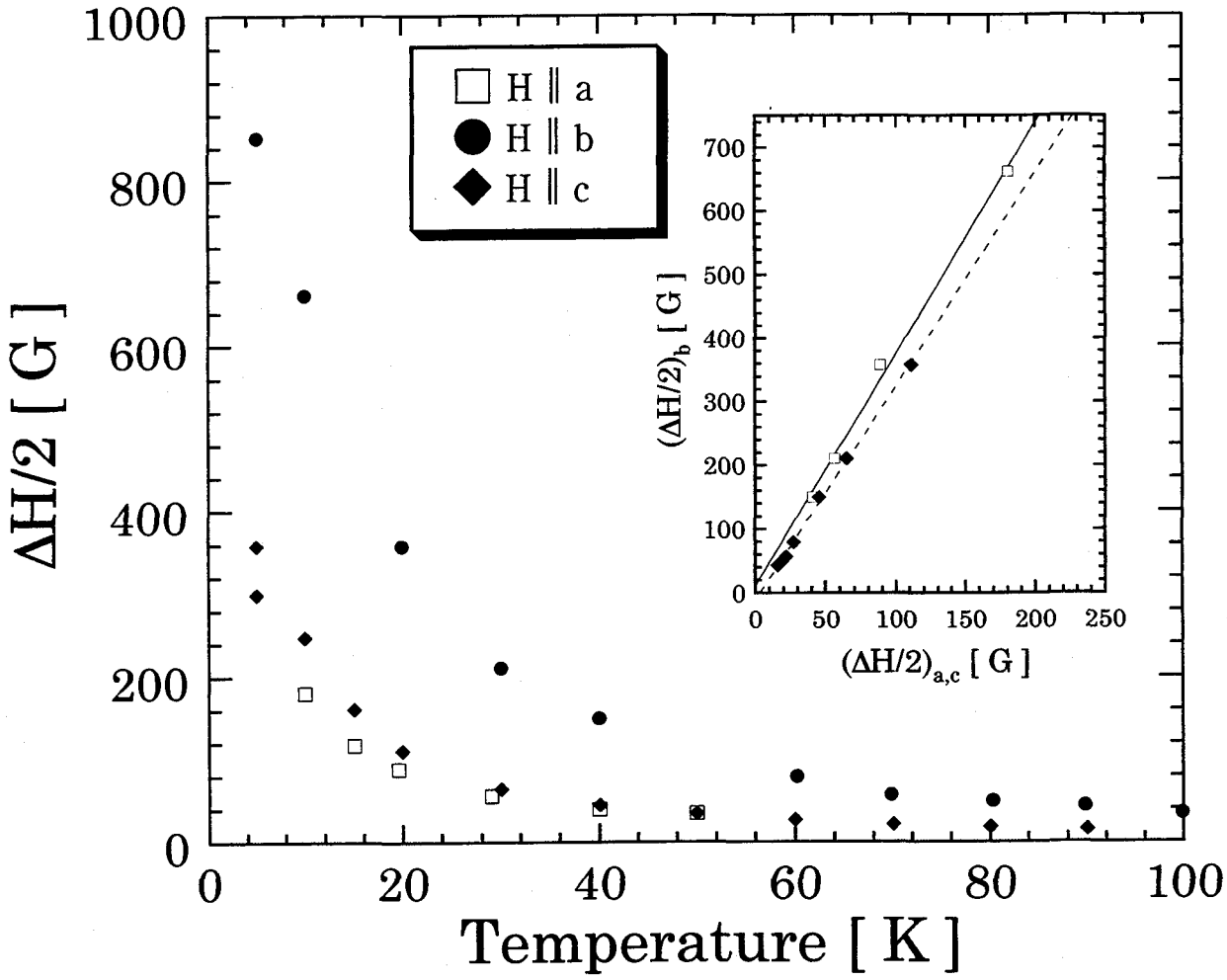

Fig.4.2.8 Temperature dependence of ΔH/2 for H||a-, b- and c-axis at 125.1MHz in Sr14-B. $(\Delta H/2)_{a,c}$ vs $(\Delta H/2)_b$ with the implicit parameter of temperature at 125.1MHz in Sr14-B are shown in the inset.

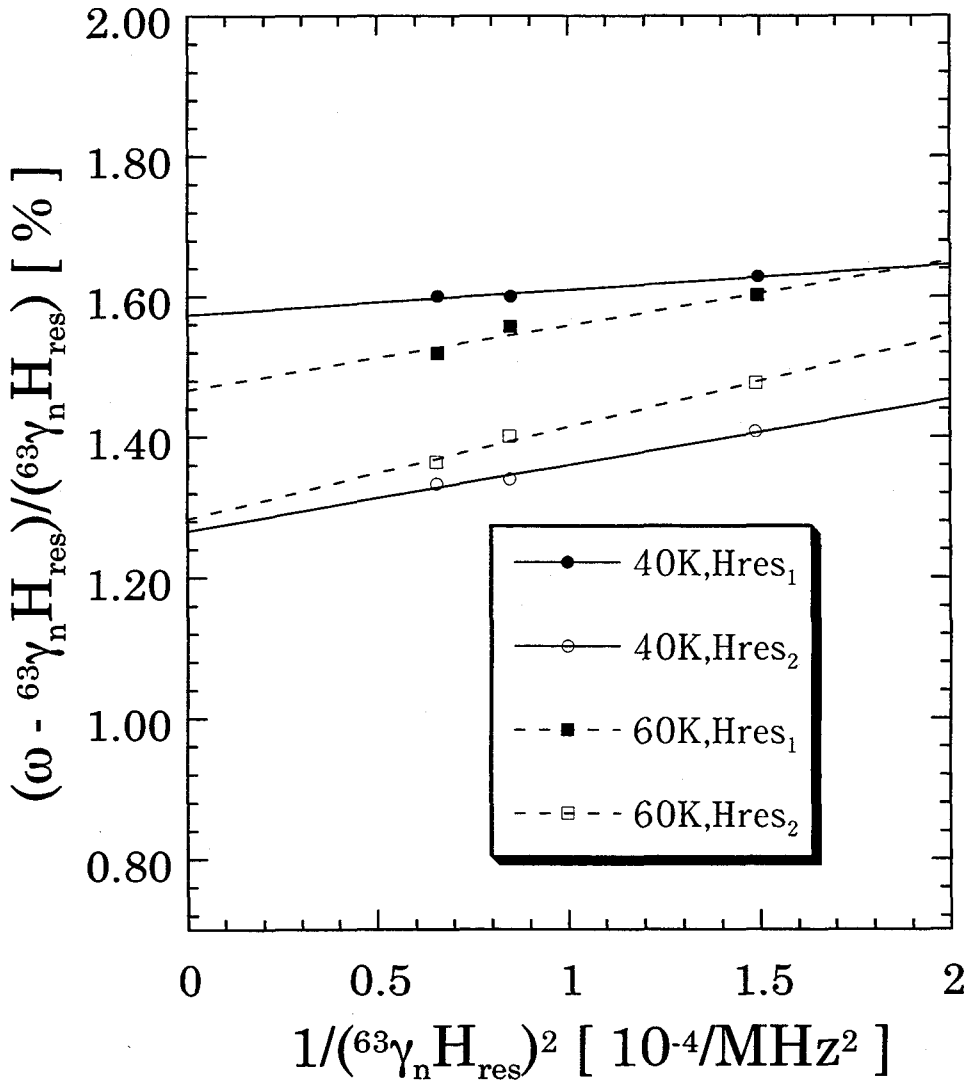

Fig.4.2.9 $(\omega - {}^{63}\gamma_n H_{res})/({}^{63}\gamma_n H_{res})$ vs $1/({}^{63}\gamma_n H_{res})^2$ at 40K and 60K in Sr14-B.

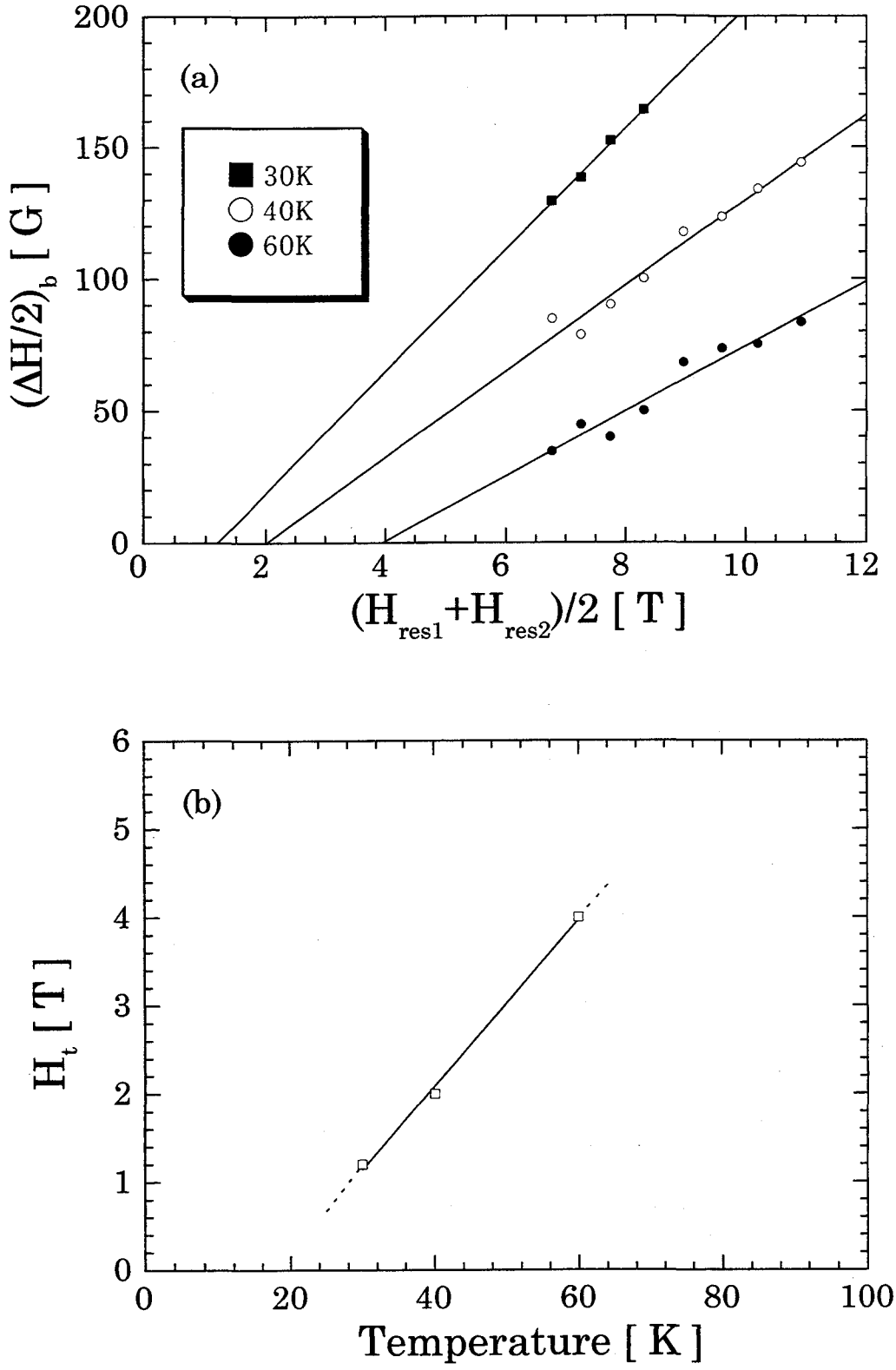

Fig.4.2.10 (a) Applied magnetic field dependence at T=30K, 40K and 60K of the ladder-Cu $\Delta H/2$ for H||b-axis at f=125.1MHz in Sr14-B. (b) Temperature dependence of the threshold magnetic field which induces the splitting of the NMR spectrum.

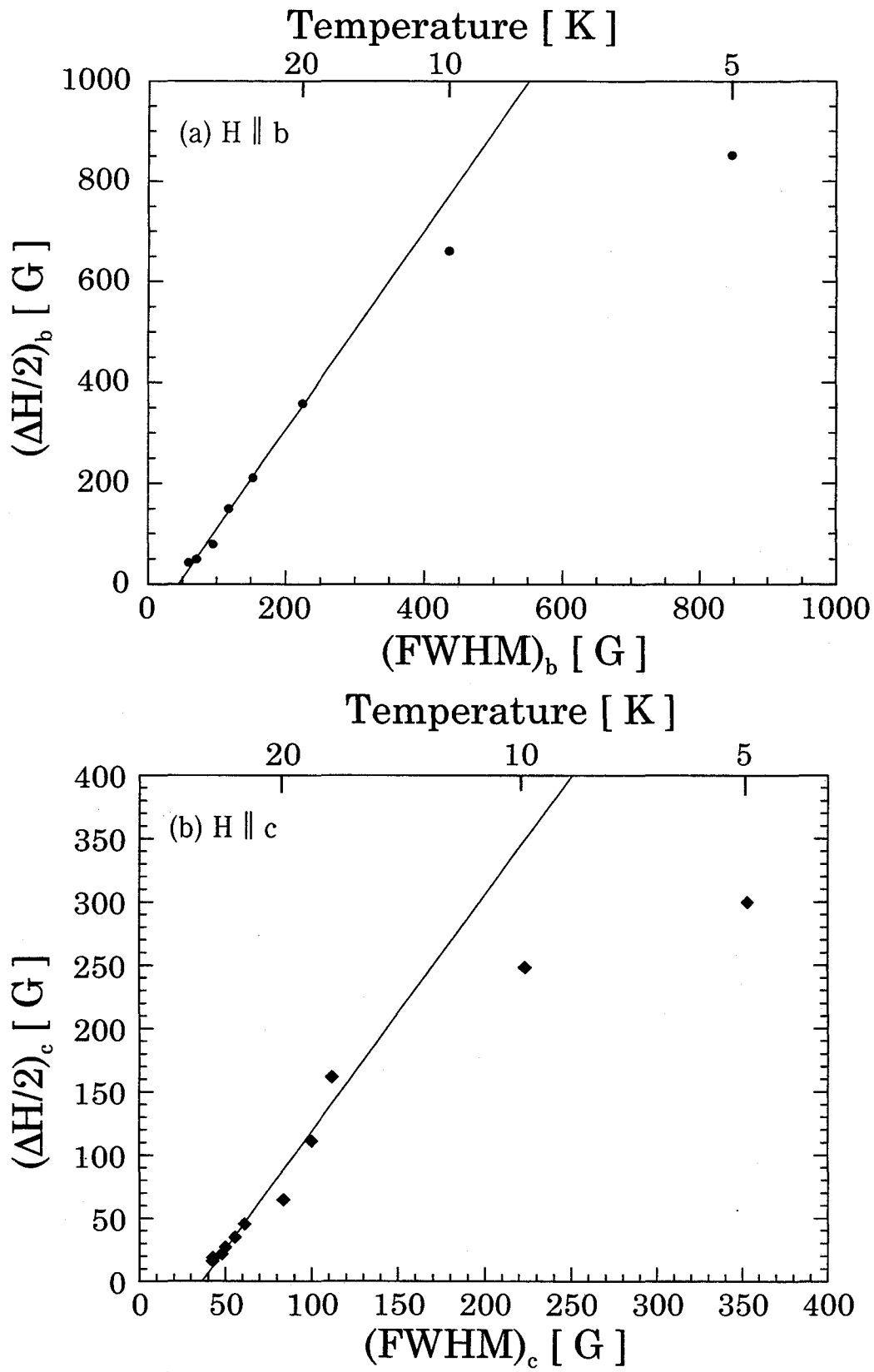

Fig.4.2.11 $\Delta H/2$ vs FWHM with the implicit parameter of temperature (a) for H||b- and (b) c-axis at 125.1MHz in Sr14-B.

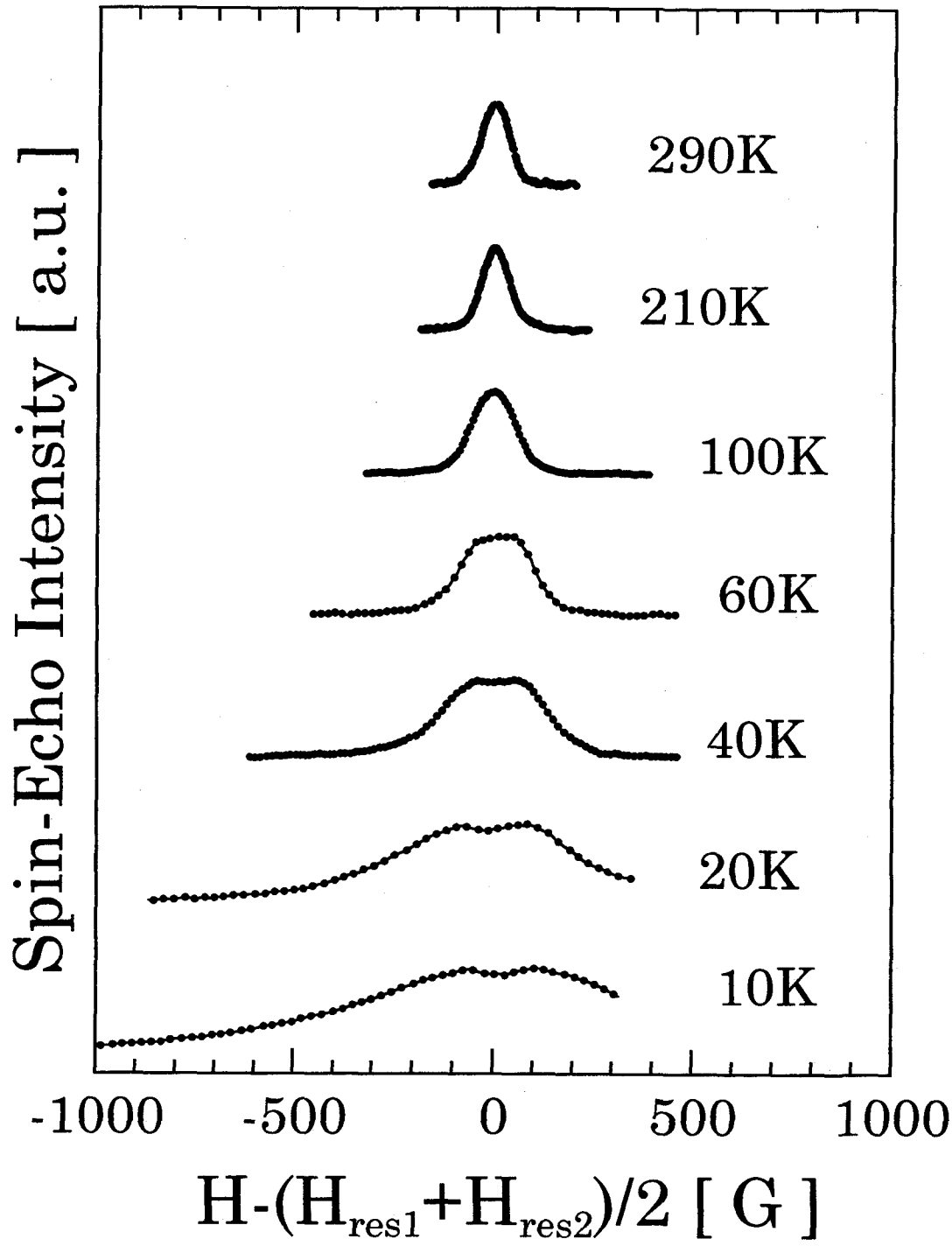

Fig.4.2.12 Temperature variation of the ladder-^{63}Cu NMR spectrum for H||b-axis at 125.1MHz in Y(0.25).

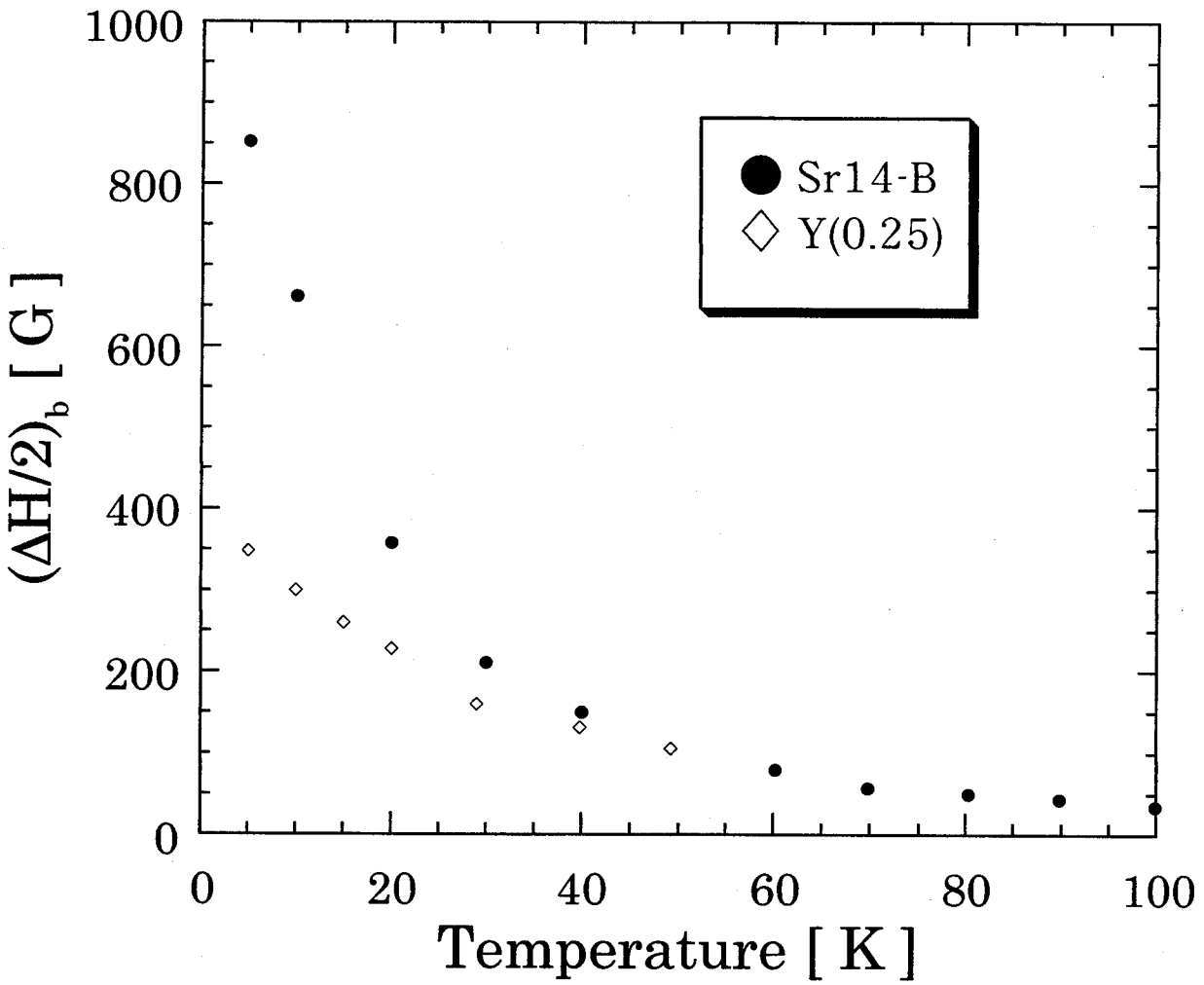

Fig.4.2.13 Temperature dependence of $\Delta H/2$ for H||b-axis at 125.1MHz in Y(0.25).

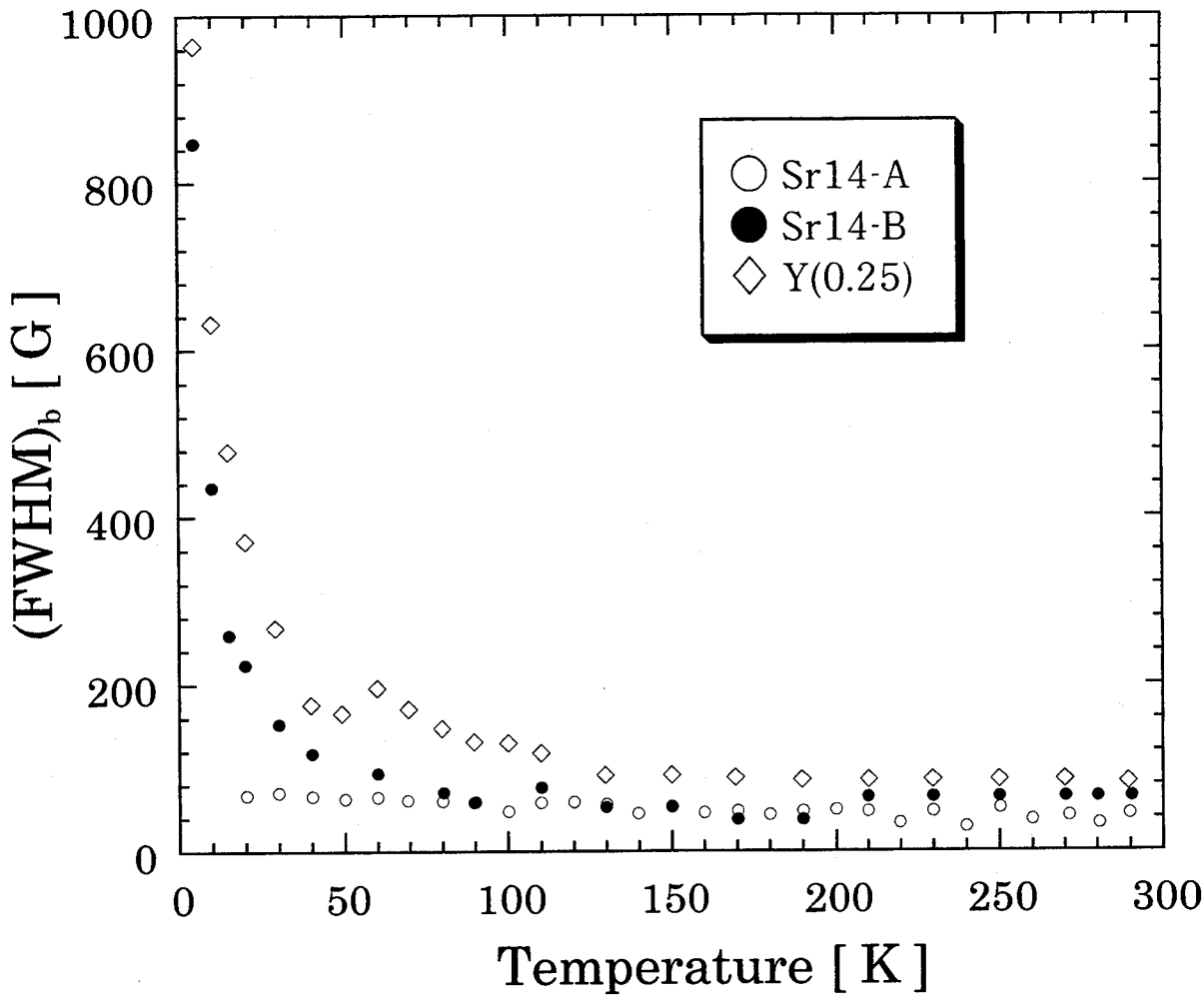

Fig.4.2.14 Temperature dependence of FWHM for H||b-axis at 125.1MHz in Y(0.25).

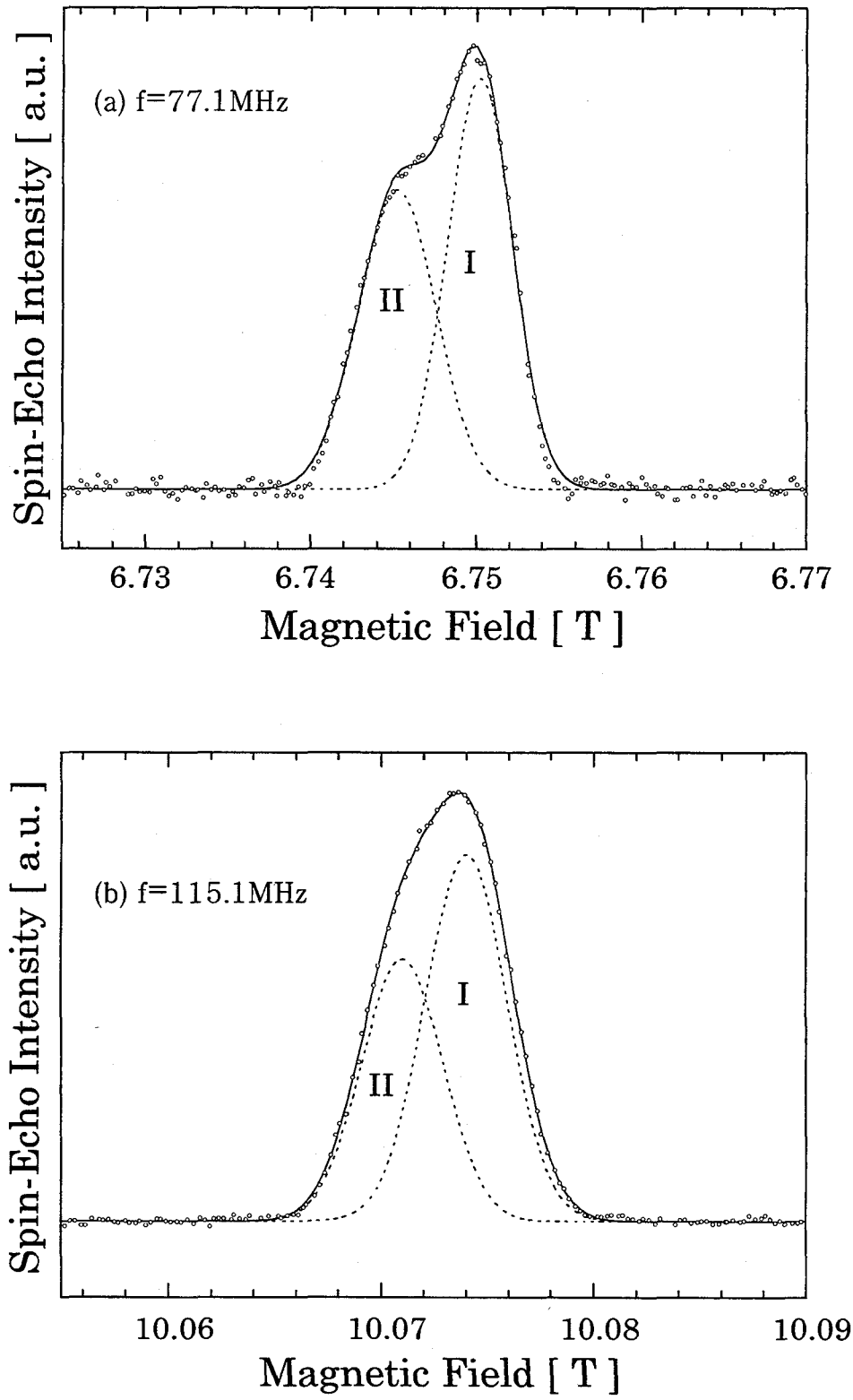

Fig.4.2.15 Frequency variation of the center line ladder-^{63}Cu NMR spectrum at T=200K for H$\|$b-axis at (a) f=77.1MHz and (b) f=115.1MHz in Sr14-A.

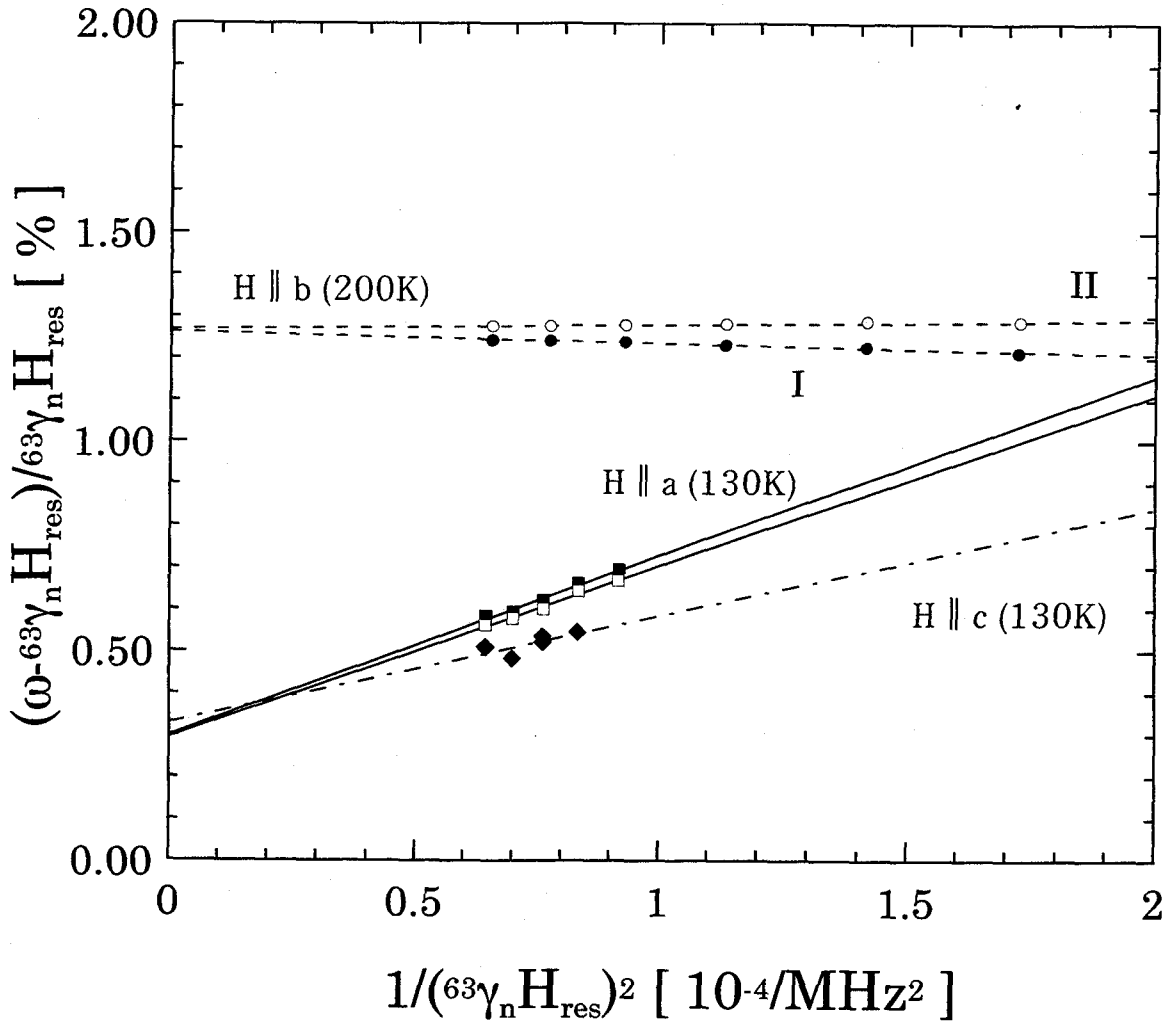

Fig.4.2.16 $(\omega - {}^{63}\gamma_n H_{res})/({}^{63}\gamma_n H_{res})$ vs $1/({}^{63}\gamma_n H_{res})^2$ for H∥a- at T=130K, b- at T=200K and c-axis at 130K in Sr14-A.

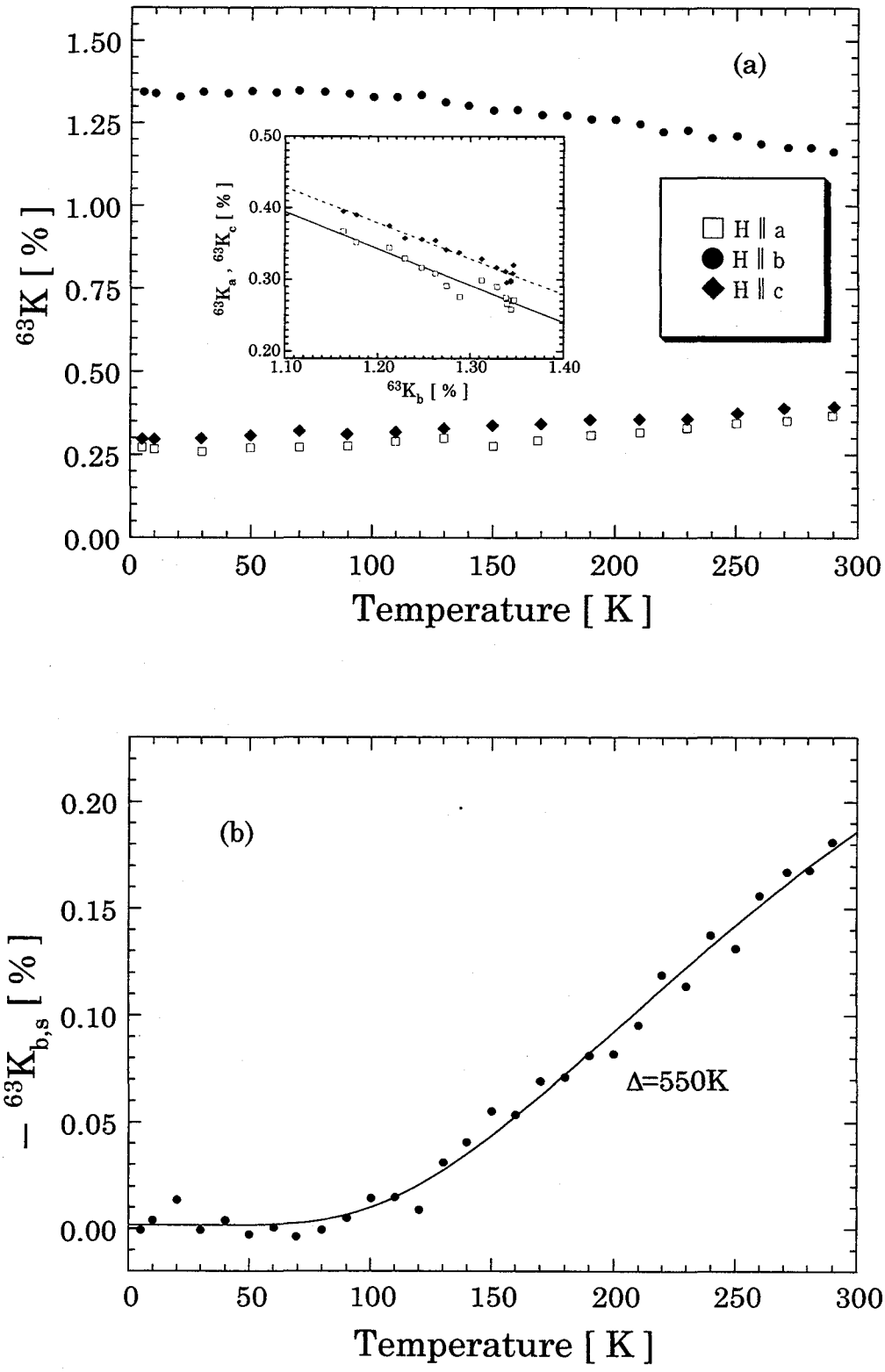

Fig.4.2.17 (a)Temperature dependence of the ladder-^{63}Cu Knight shift for each direction in Sr14-A. $^{63}K_{a,c}$ vs $^{63}K_b$ are shown in the inset. (b) Temperature dependence of the spin part of the ladder-^{63}Cu Knight Shift along the b-axis in Sr14-A.

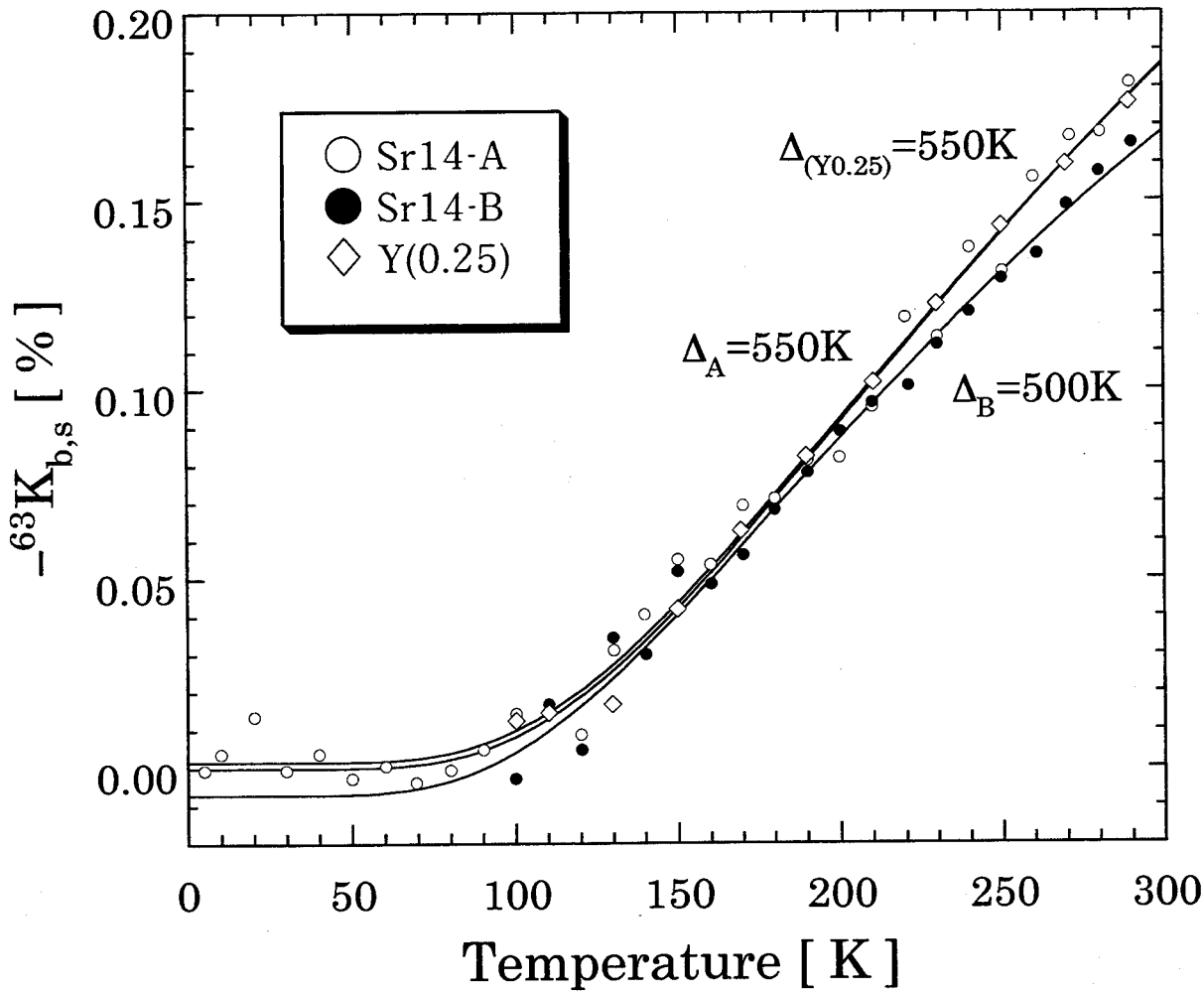

Fig.4.2.18 Temperature dependence of the spin part of the ^{63}Cu-ladder Knight shift along the b-axis in Sr14-A, Sr14-B and Y(0.25).

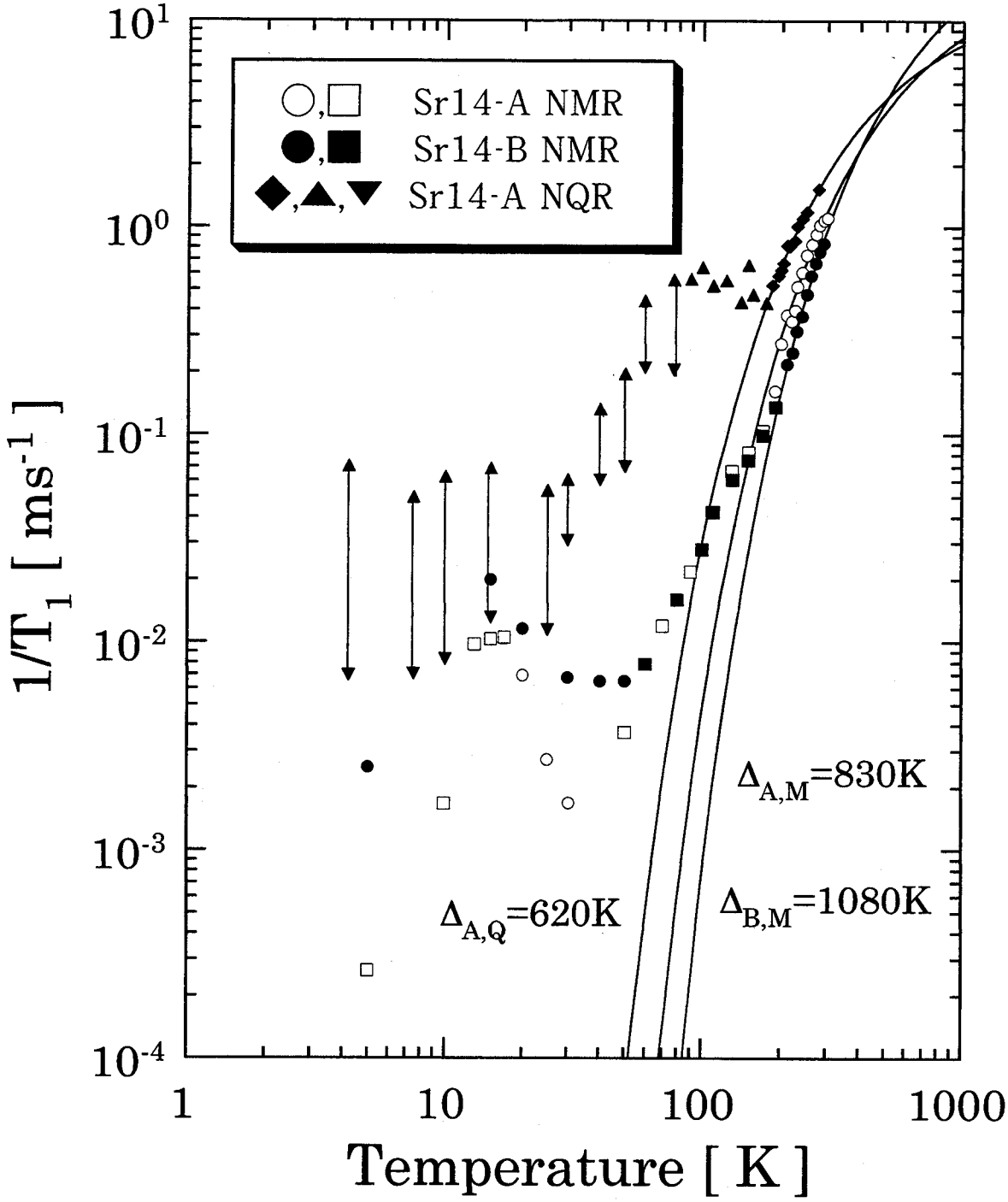

Fig.4.2.19 Temperature dependence of the ^{63}Cu spin-lattice relaxation rate in Sr14-A and Sr14-B.

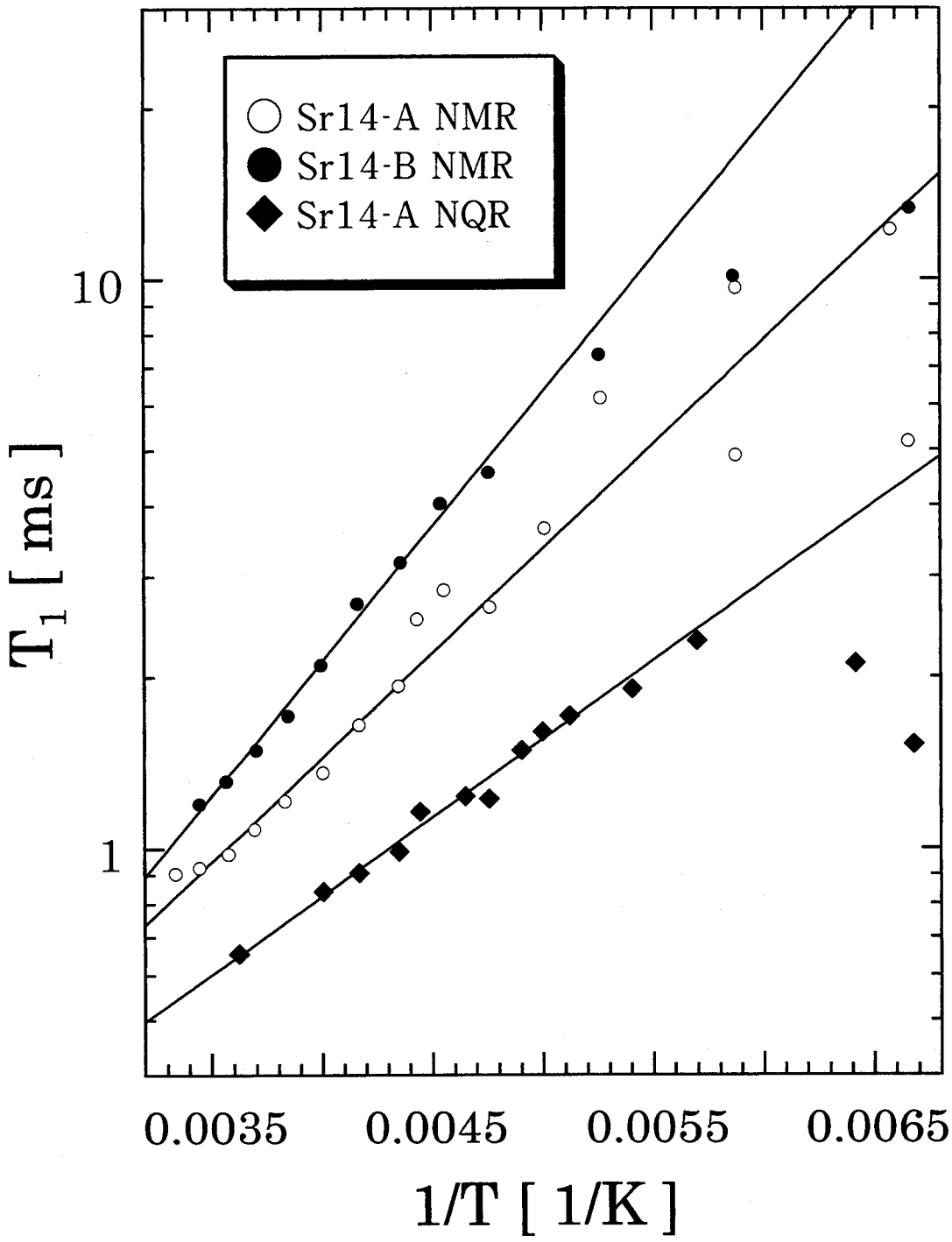

Fig.4.2.20 The Arrhenius plot of T_1 in semi-logarithmic scales in Sr14-A.

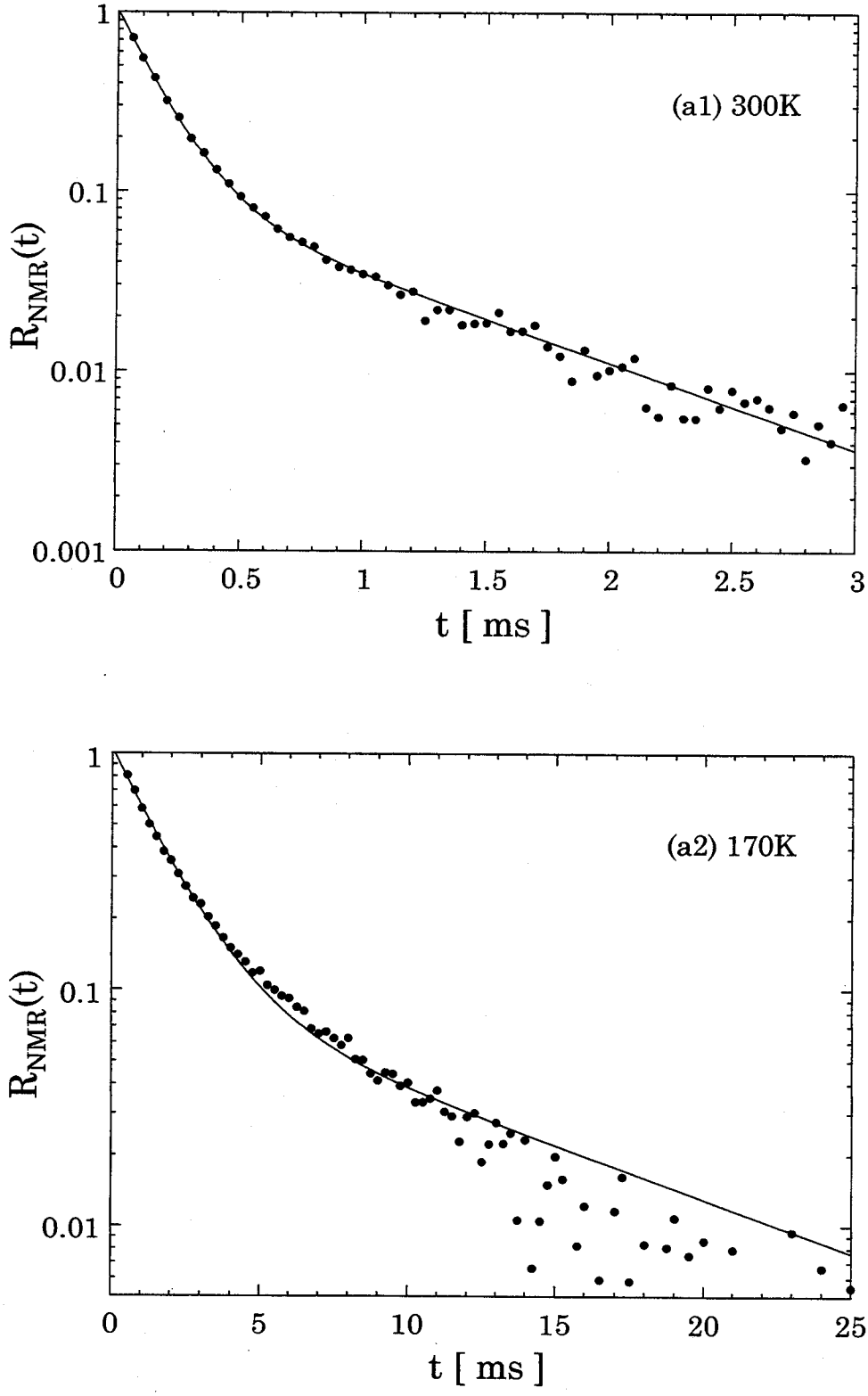

Fig.4.2.21 Temperature variation of $R(t)$ in NMR and NQR measurements. (a1) NMR at 300K. (a2) NMR at 170K. (b1) NQR at 280K. (b2) NQR at 10K.

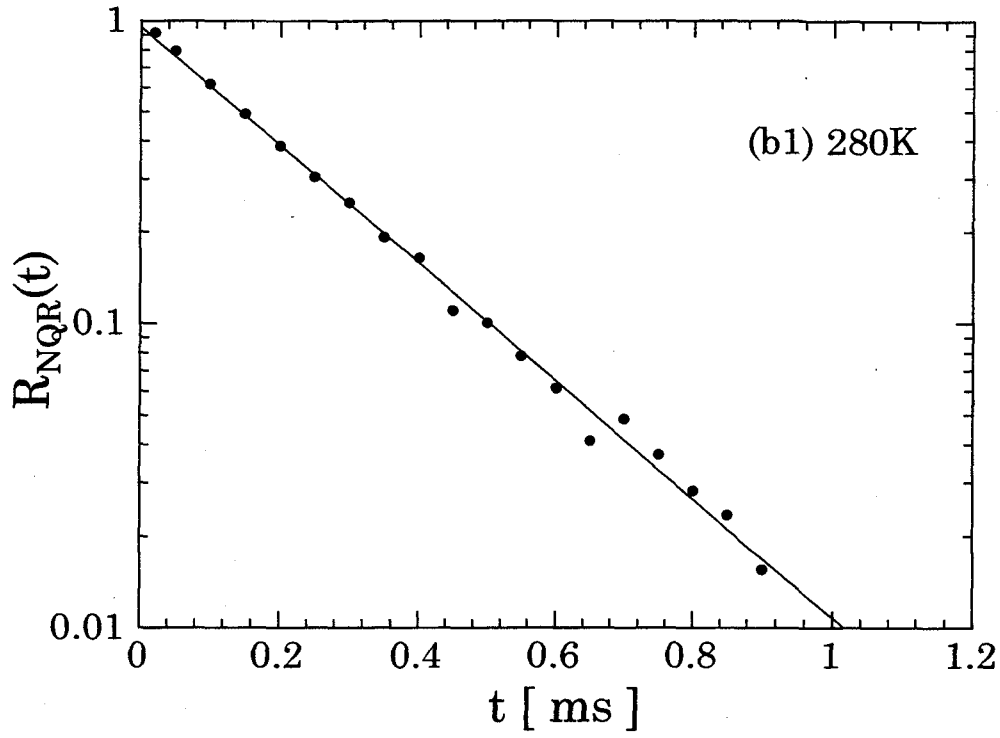

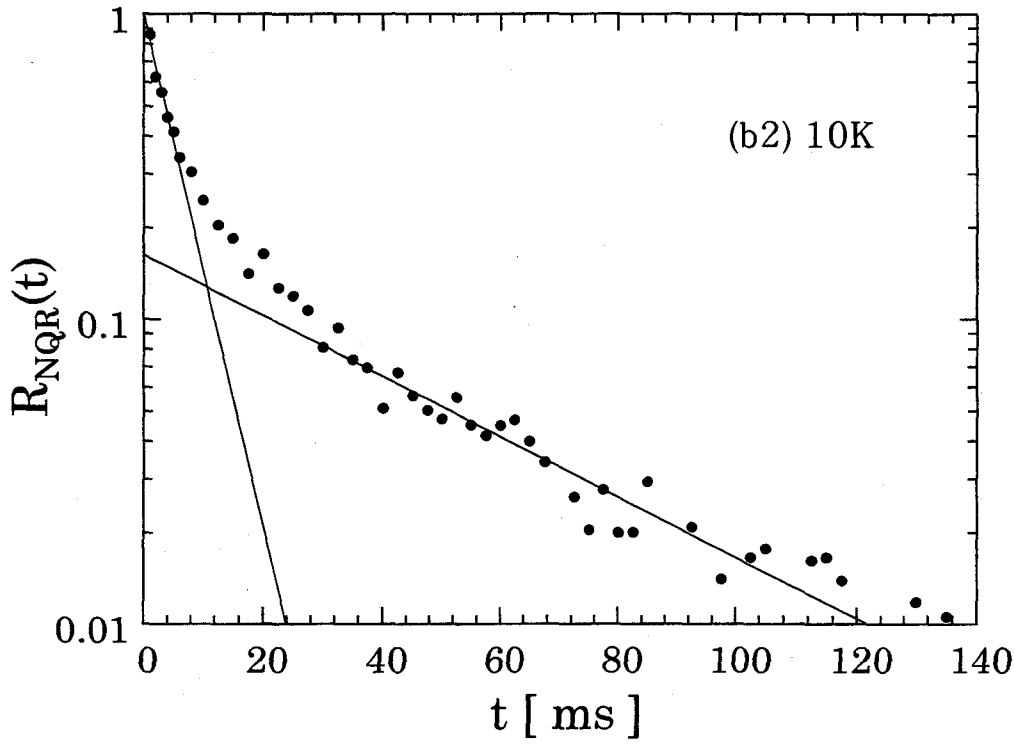

Fig.4.2.21 (b1) NQR at 280K. (b2) NQR at 10K.

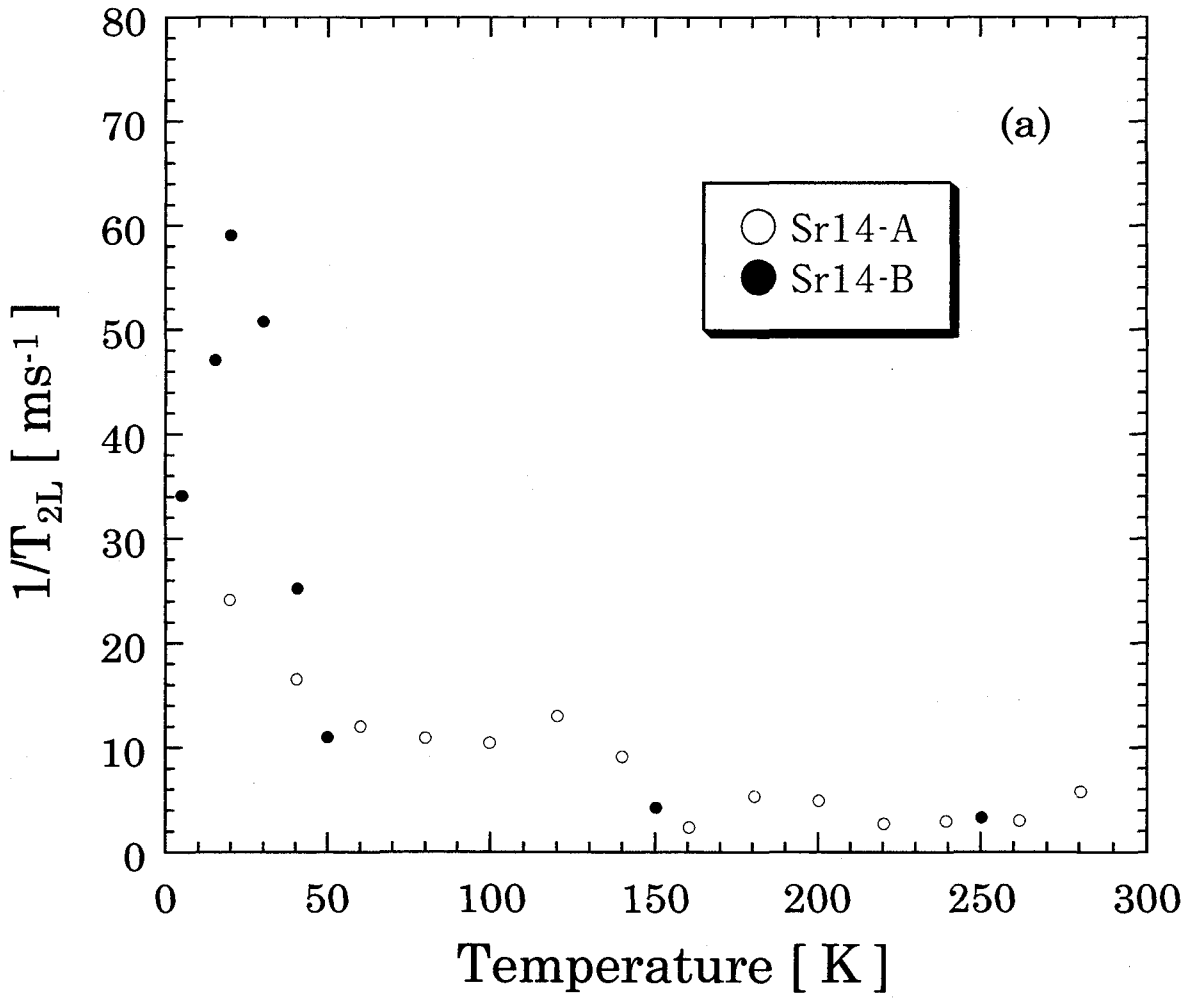

Fig.4.2.22 (a) Temperature dependence of the ladder-^{63}Cu spin-echo decay rate due to the spin-lattice relaxation process, $^{63}(1/T_{2L})$, in Sr14-A and Sr14-B. Time(τ) dependence of the intensity of the ladder-^{63}Cu nuclear spin magnetization, $I(2\tau)/I(0)$, at T=20K and f=125.1MHz in (b1) Sr14-B and (b2) Sr14-A.

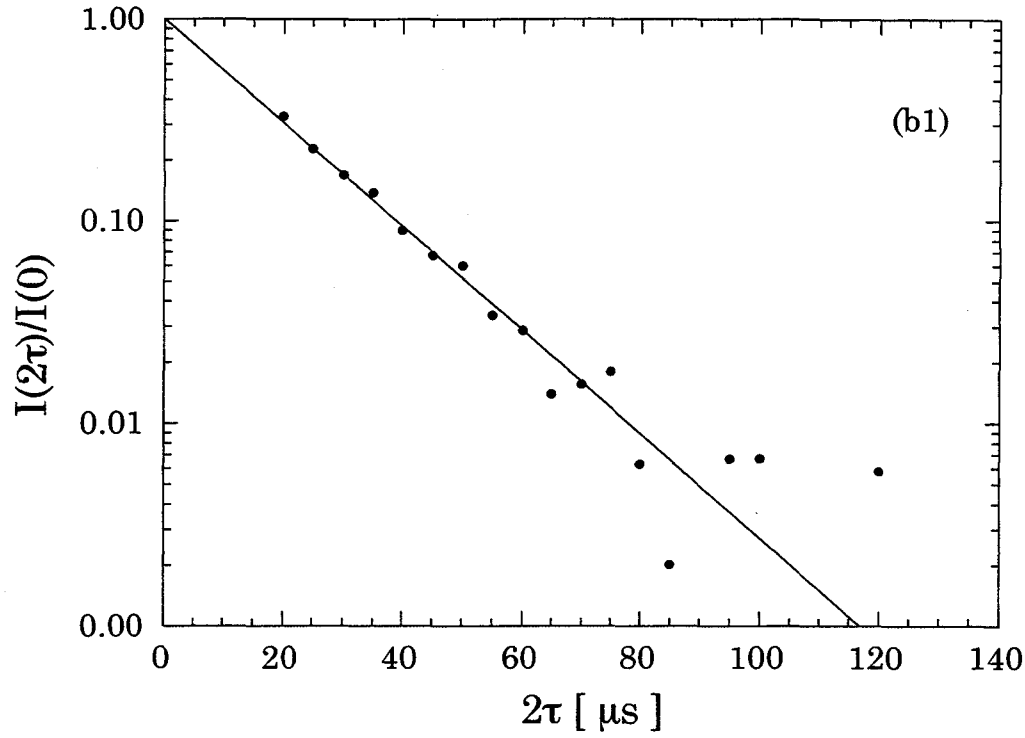

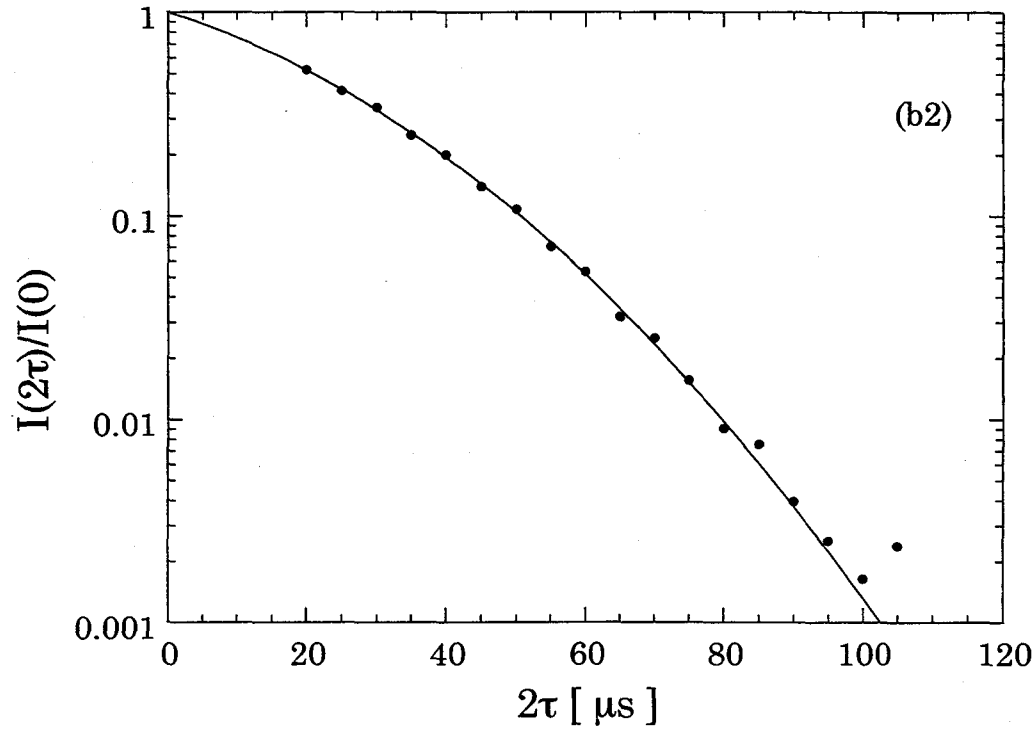

Fig.4.2.22 (b1),(b2).

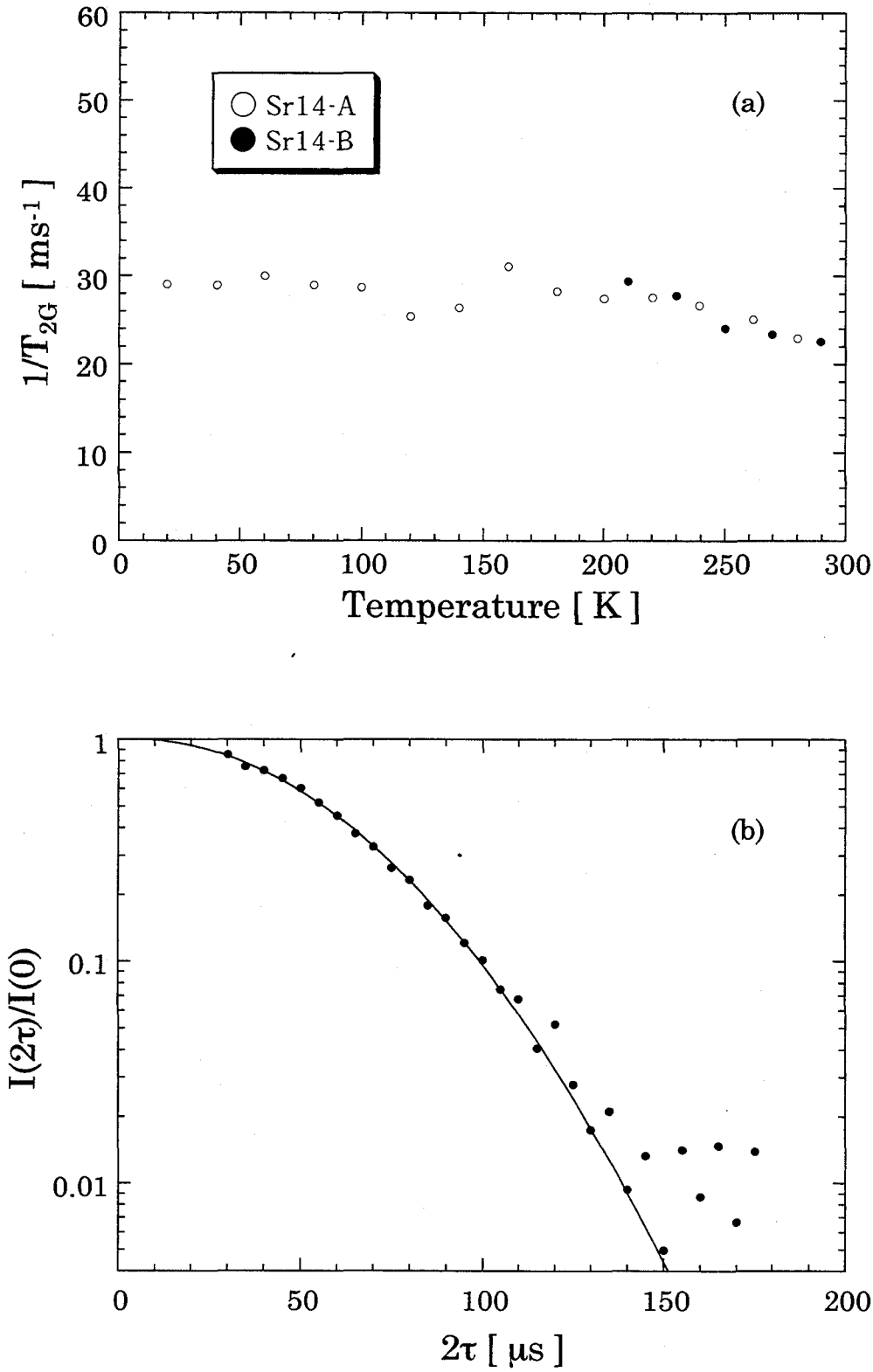

Fig.4.2.23 (a) Temperature dependence of the ladder-^{63}Cu Gaussian spin-echo decay rate for H$\|$b-axis, $^{63}(1/T_{2G})$, in Sr14-A and Sr14-B. (b) Time(τ) dependence of the intensity of the ladder-^{63}Cu nuclear spin magnetization, $I(2\tau)/I(0)$, for H$\|$b-axis at T=290K and f=125.1MHz in Sr14-B

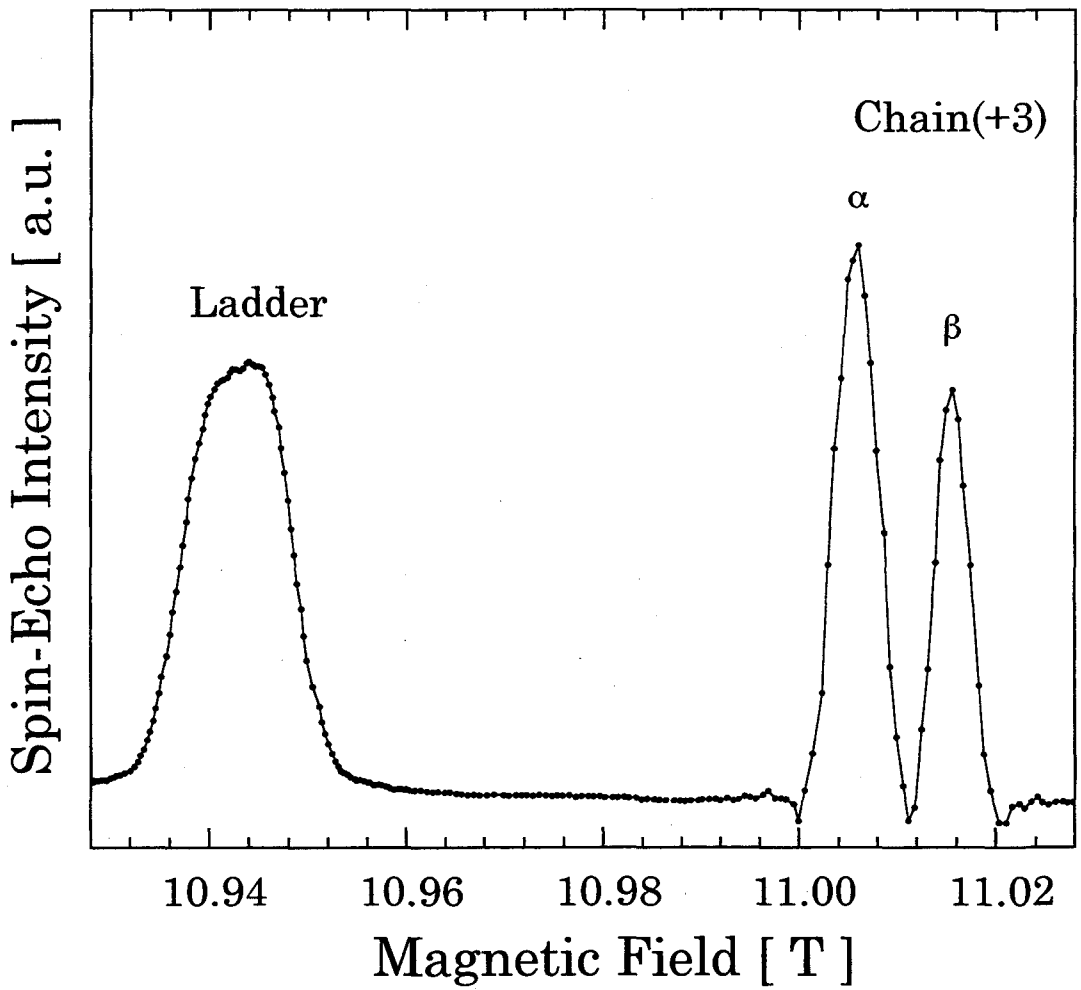

Fig.4.3.1 Chain(+3)-^{63}Cu center line NMR spectrum for H||b-axis at T=30K in f=125.1MHz in Sr14-A.

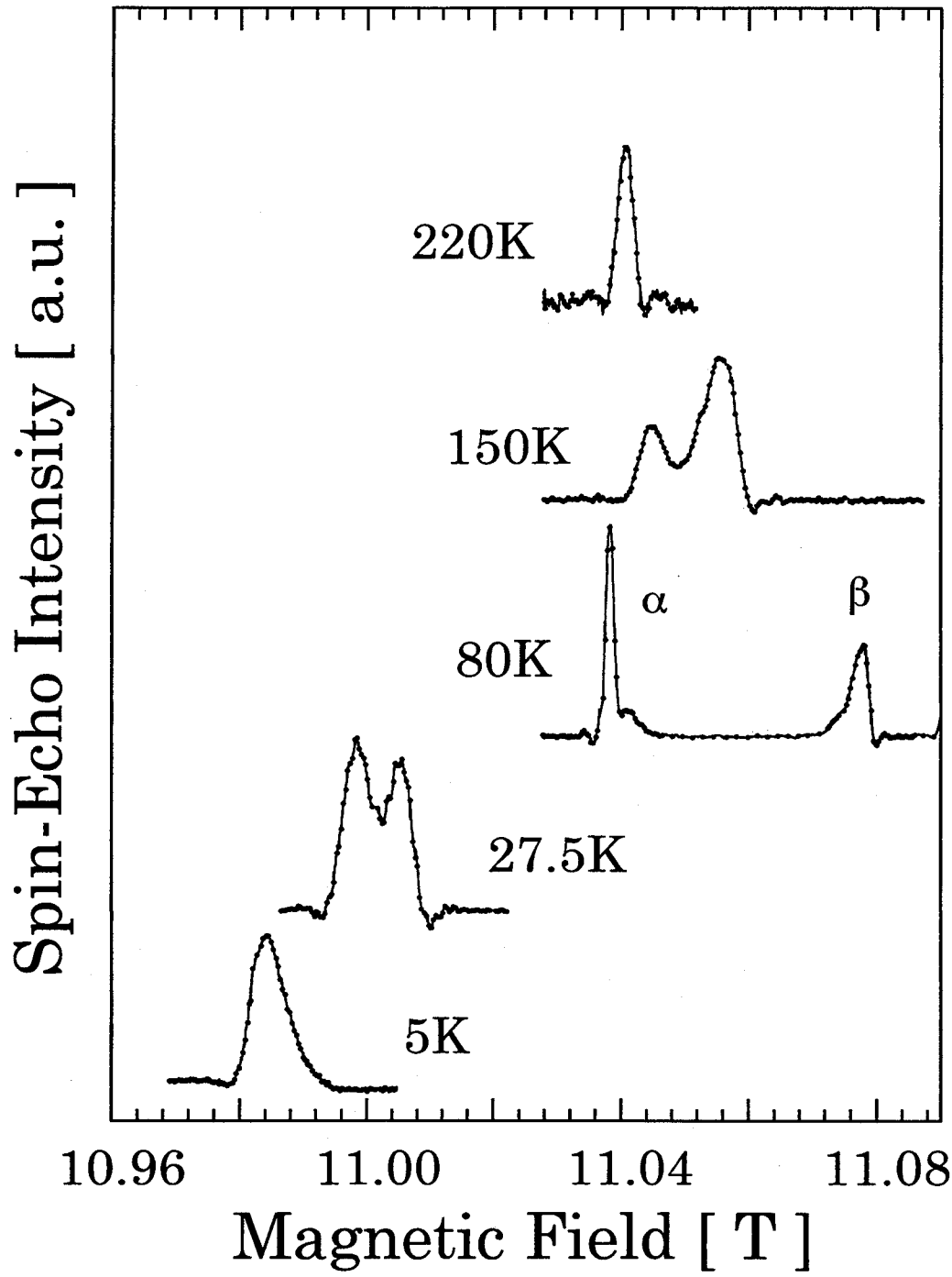

Fig.4.3.2 Temperature variation of the chain(+3)-^{63}Cu center line NMR spectrum for H||b-axis in Sr14-A.

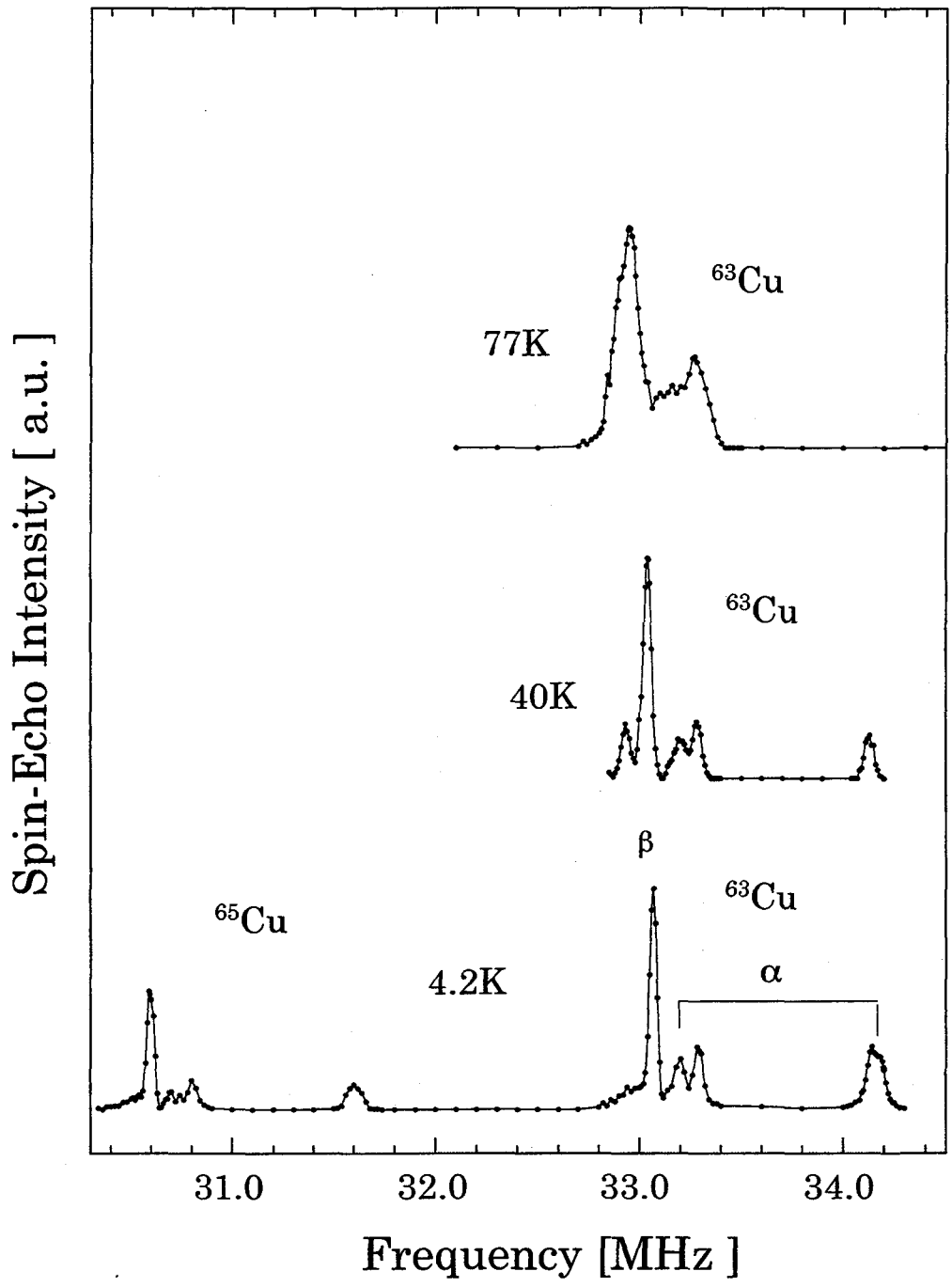

Fig.4.3.3 Temperature variation of the chain(+3)-Cu NQR spectrum in Sr14-A.

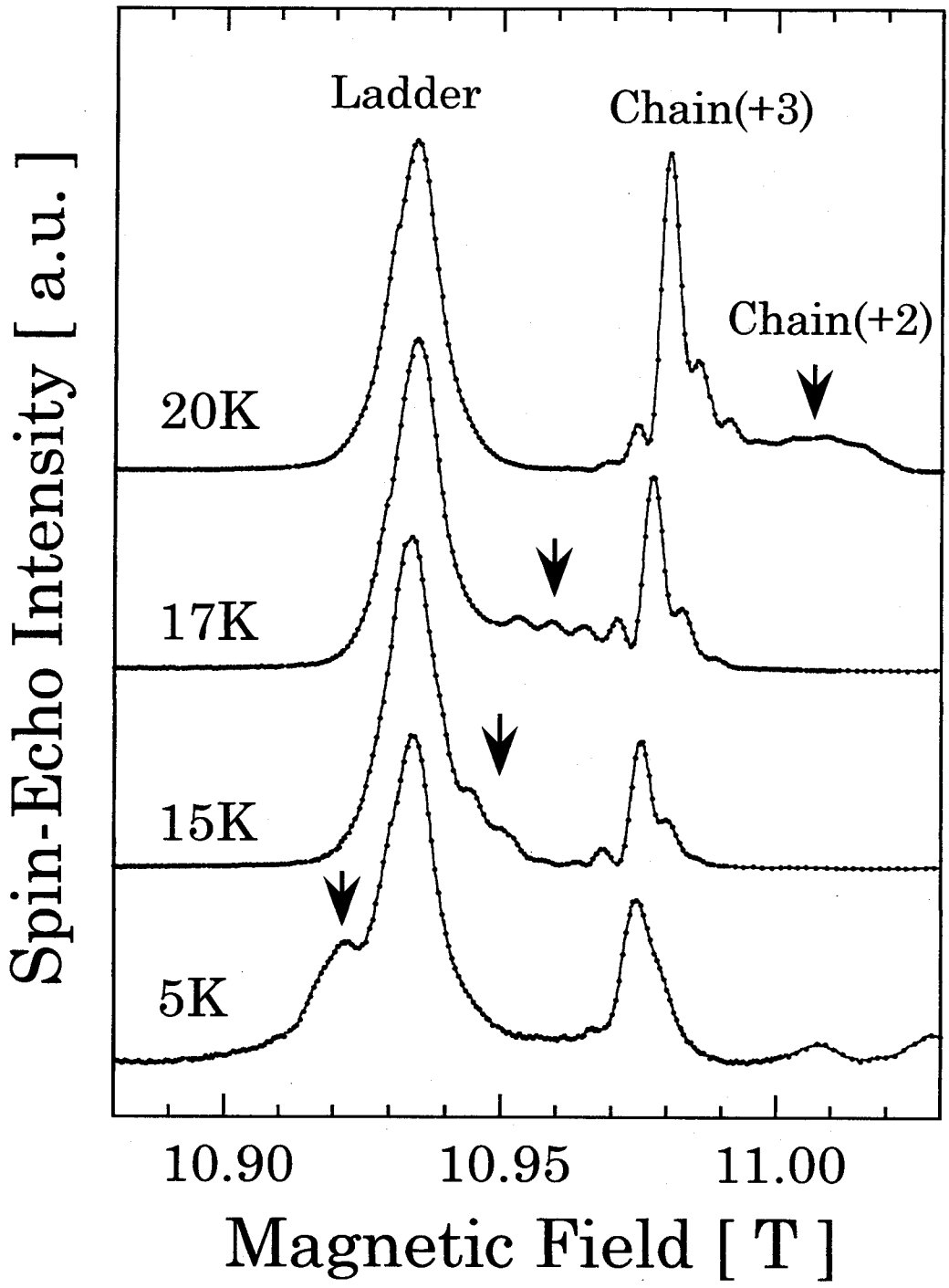

Fig.4.3.4 Temperature variation of the chain(+2)-^{63}Cu center line NMR spectrum for H||b-axis in Sr14-A.

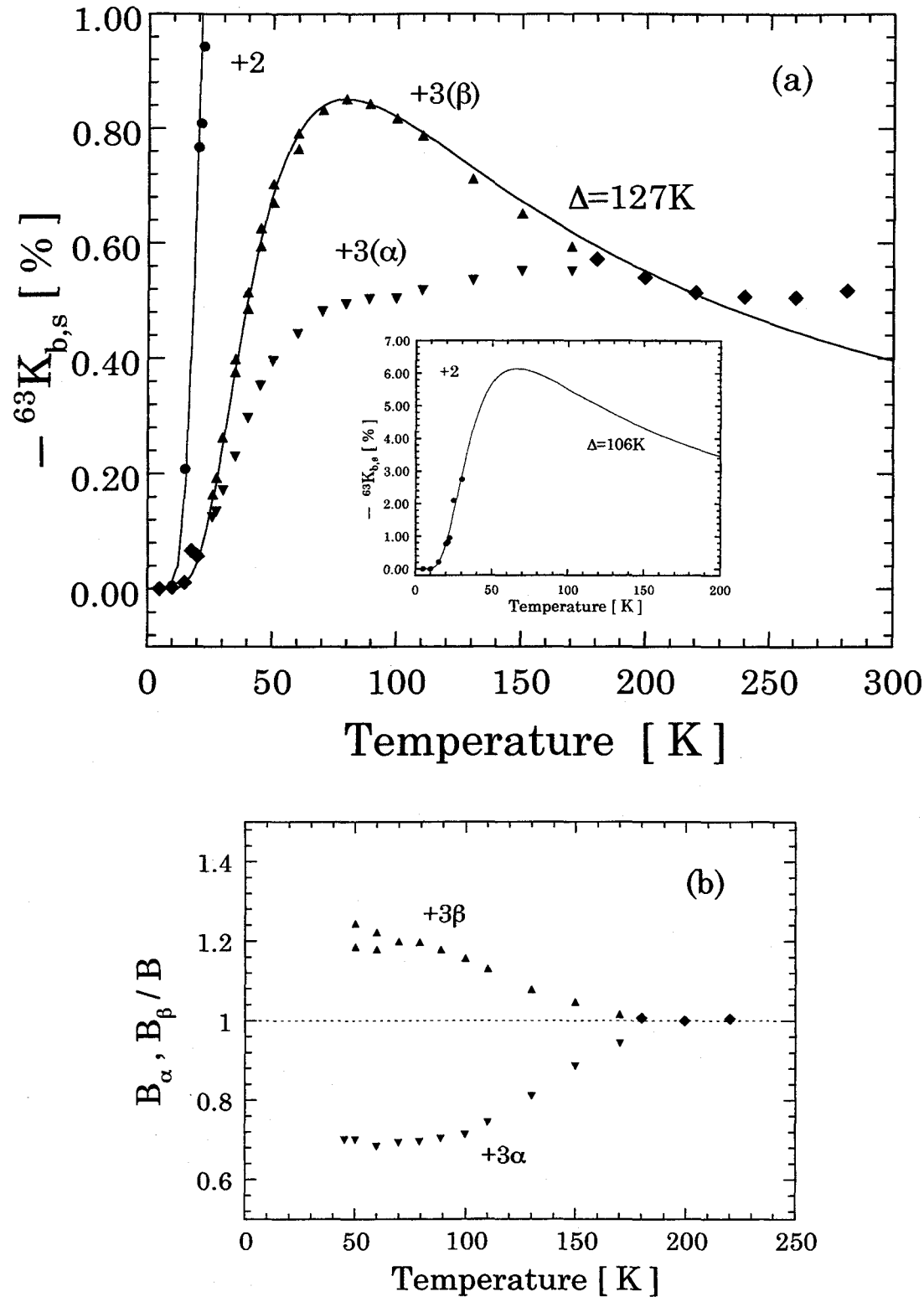

Fig.4.3.5 (a)Temperature dependenc of the spin part of the chain-^{63}Cu Knight shift for H||b-axis, $^{63}K_{b,s}$ in Sr14-A. Temperature dependence of $^{63}K_{b,s}(+2)$ is featured in the inset. (b) Temperature dependence of the transferred hyperfine coupling constants divided by B at T=200K.

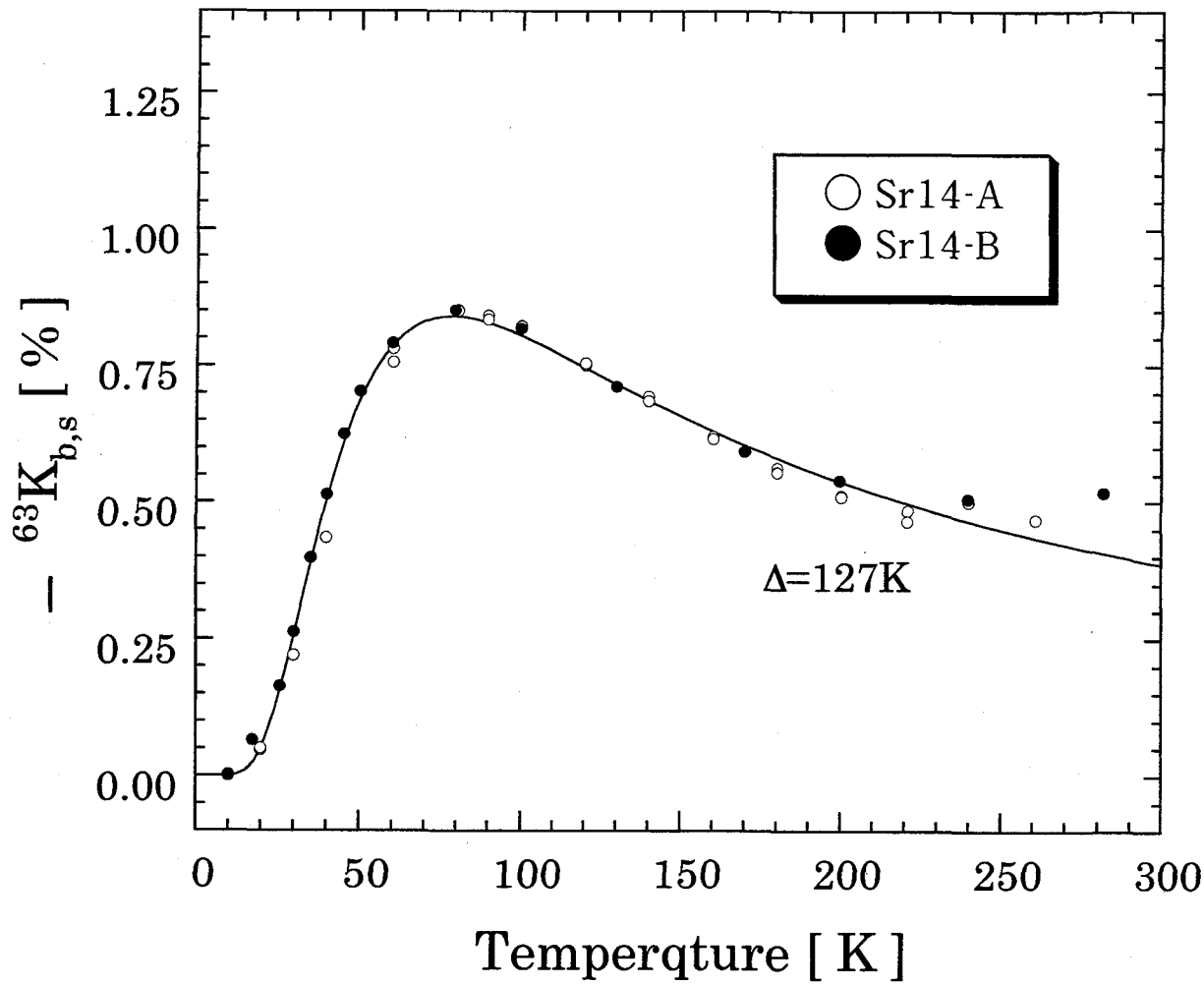

Fig.4.3.6 Temperature dependence of ${}^{63}K_{b,s}(+3,\beta)$ for H||b-axis in Sr14-A and Sr14-B.

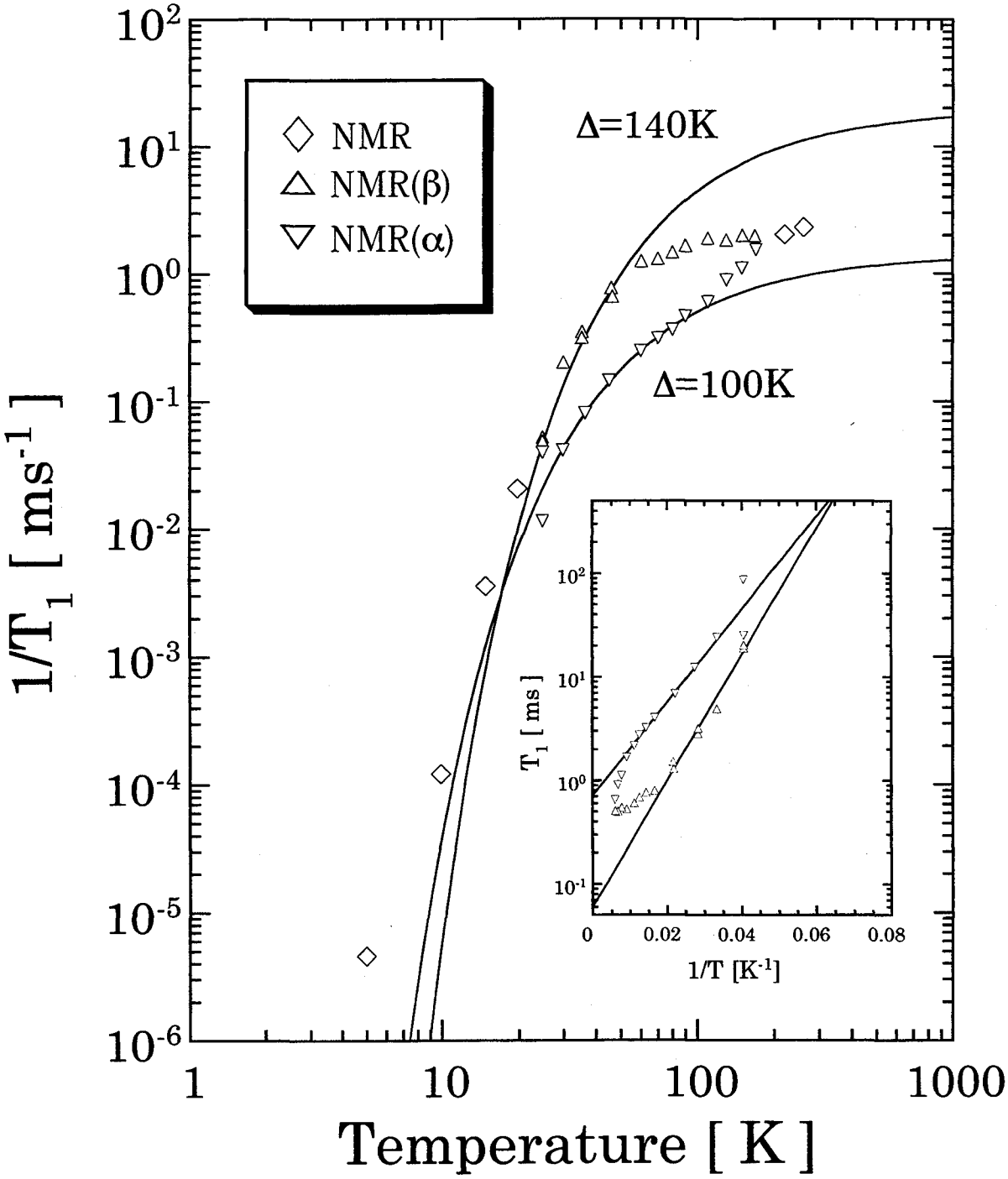

Fig.4.3.7 Temperature dependence of the chain-^{63}Cu NMR spin-lattice relaxation rate for H||b-axis in Sr14-A. The Arrhenius plot of T_1 in semi-logarithmic scales in Sr14-A is shown in the inset.

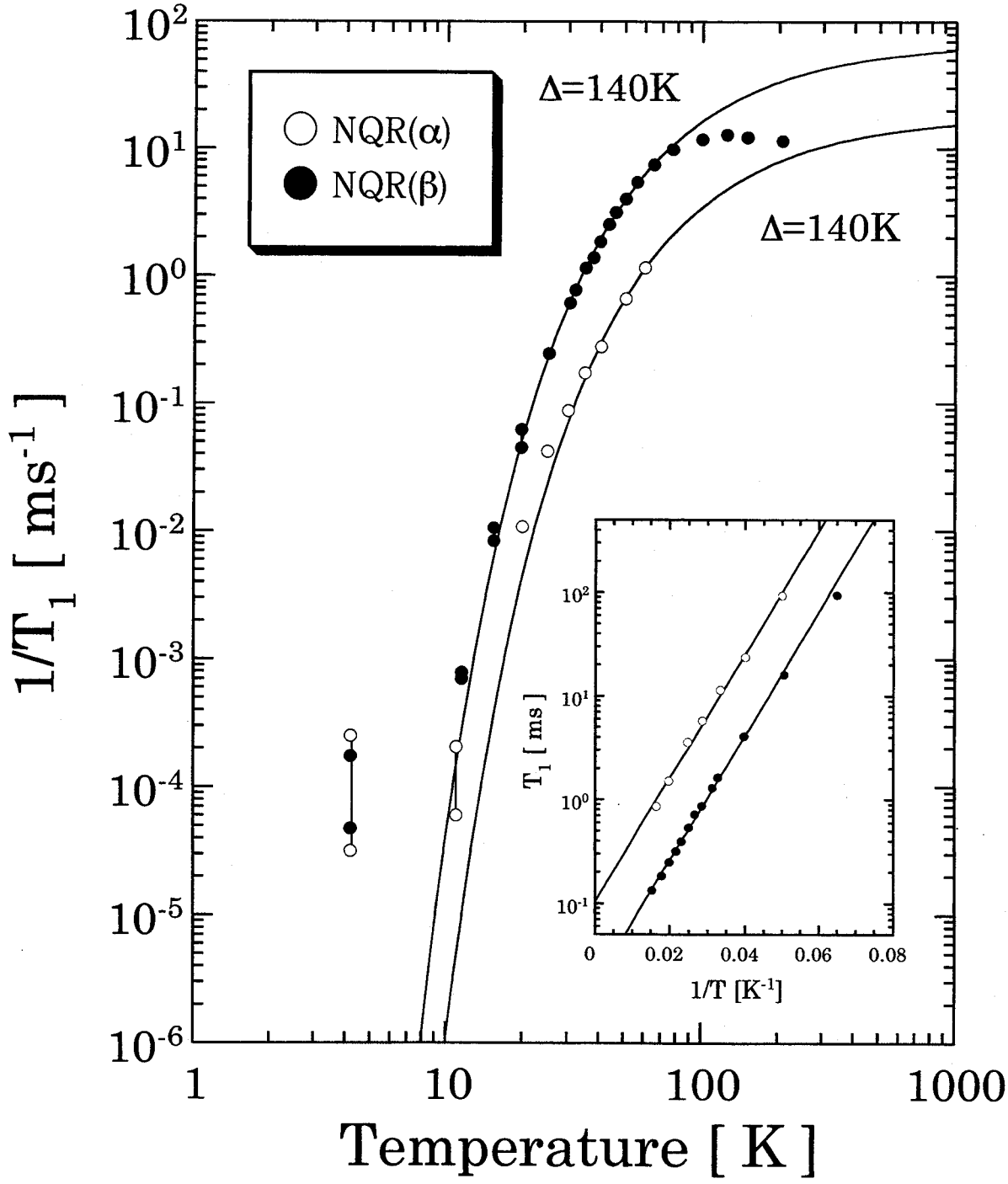

Fig.4.3.8 Temperature dependence of the chain-^{63}Cu(+3) NQR spin-lattice relaxation rate in Sr14-A. The Arrhenius plot of T_1 in semi-logarithmic scales in Sr14-A is shown in the inset.

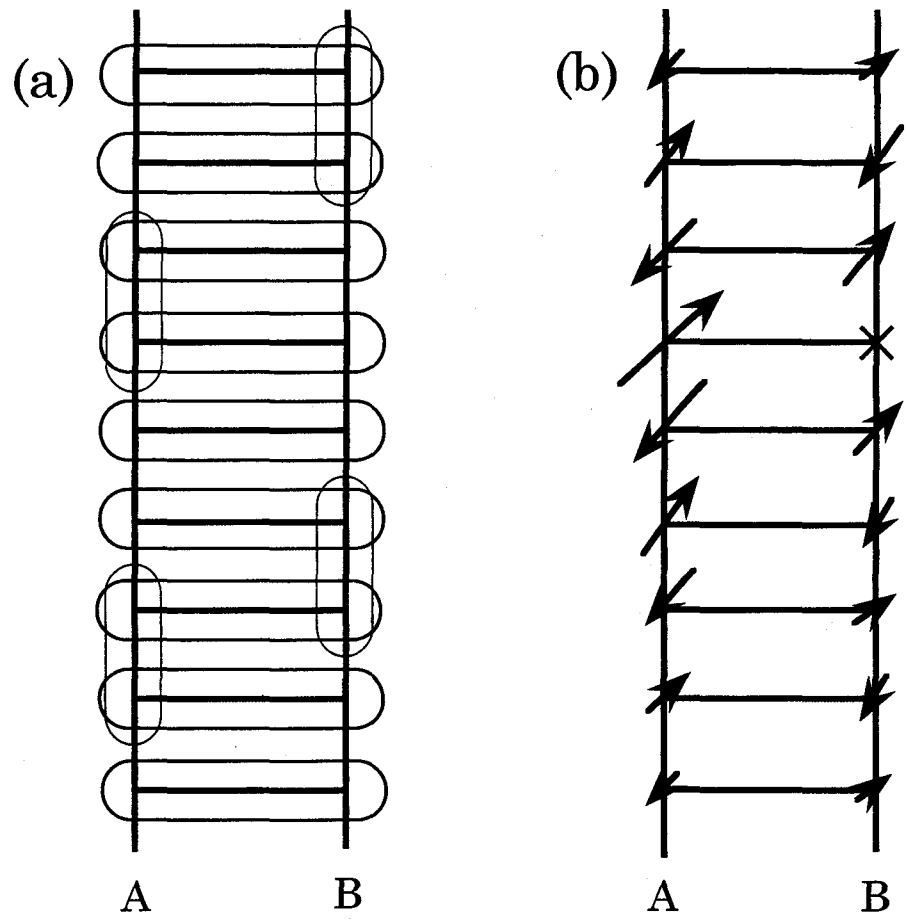

Fig.4.4.1 (a) Singlet ground stste in the two-leg ladder system. (b) Staggered moments induced by spin defects.

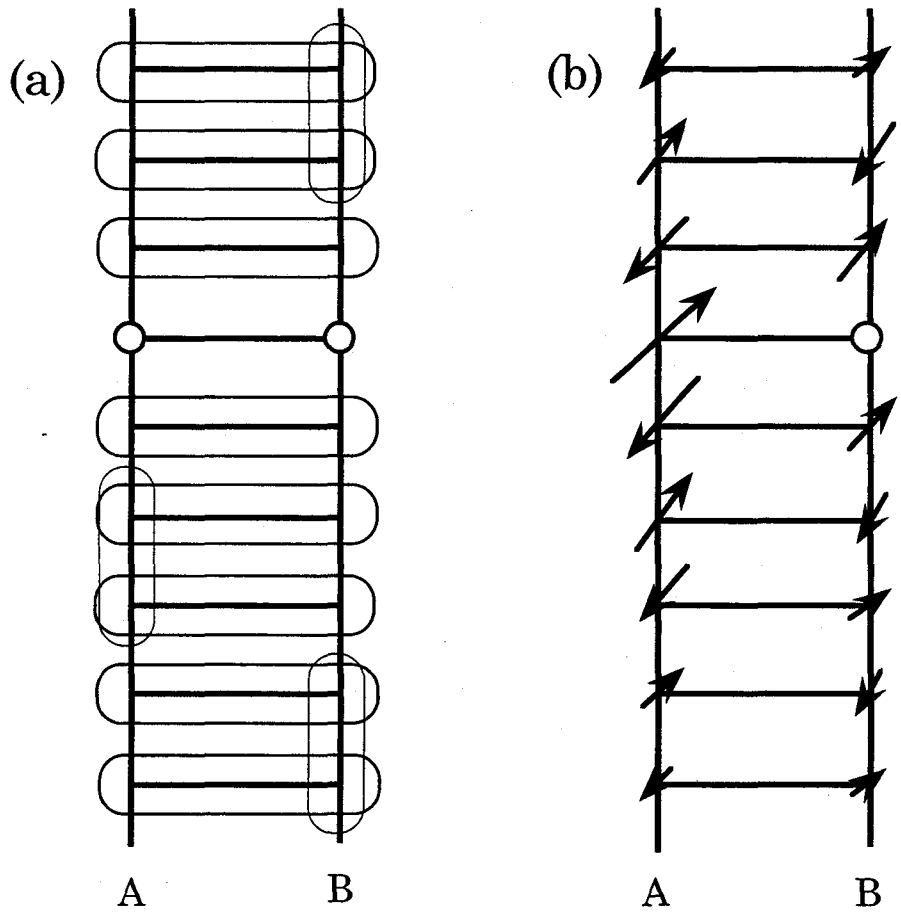

Fig.4.4.2 (a) Pairing of holes. (b) Staggered moments induced by the unpaired hole.

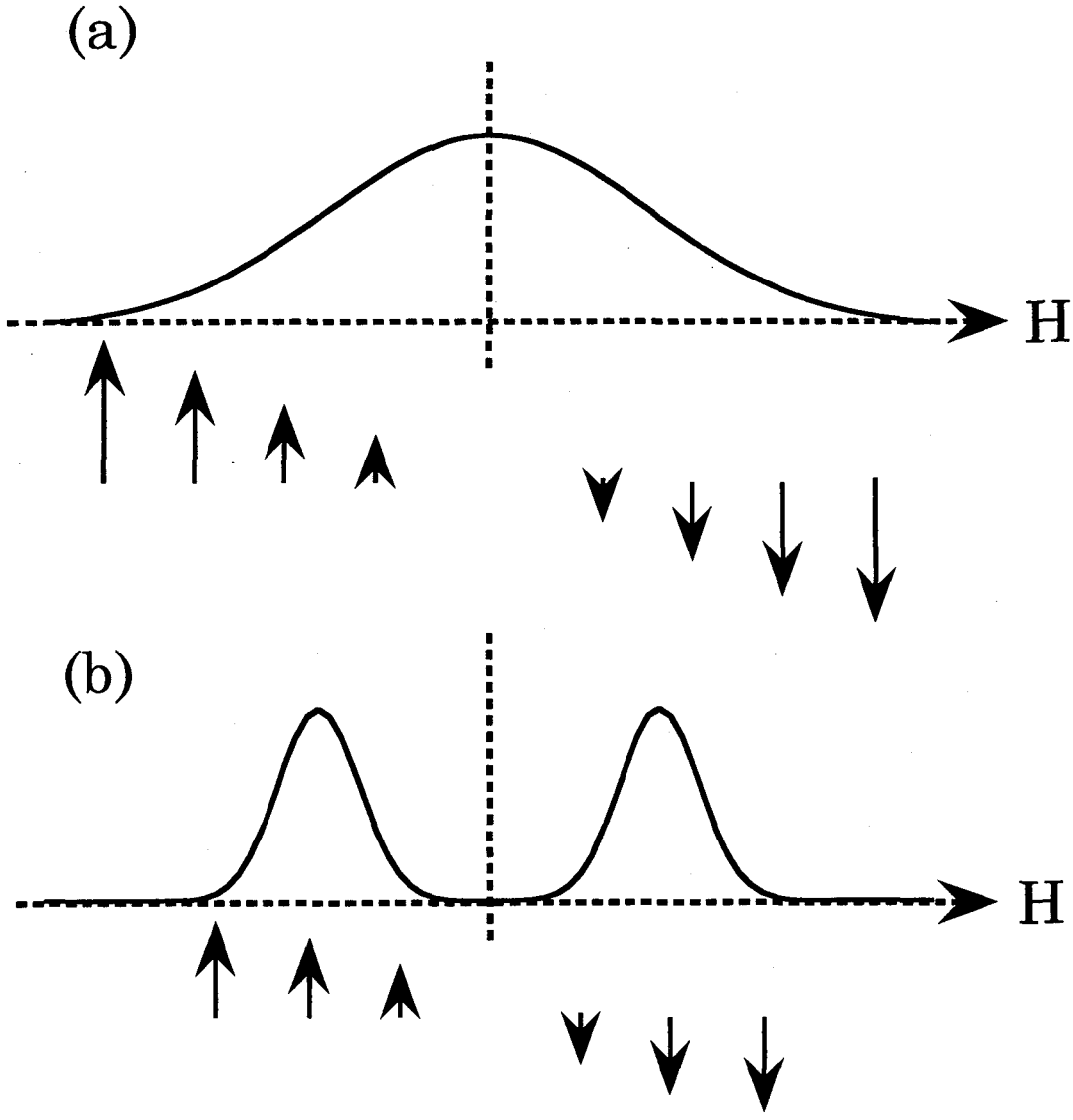

Fig.4.4.3 Schematic explanations (a) for the broadening of a NMR spectrum and (b) for the splitting and broadening where arrows correspond to K_{alt}. Up and down arrows indicate the positive shift and the negative one, respectively.

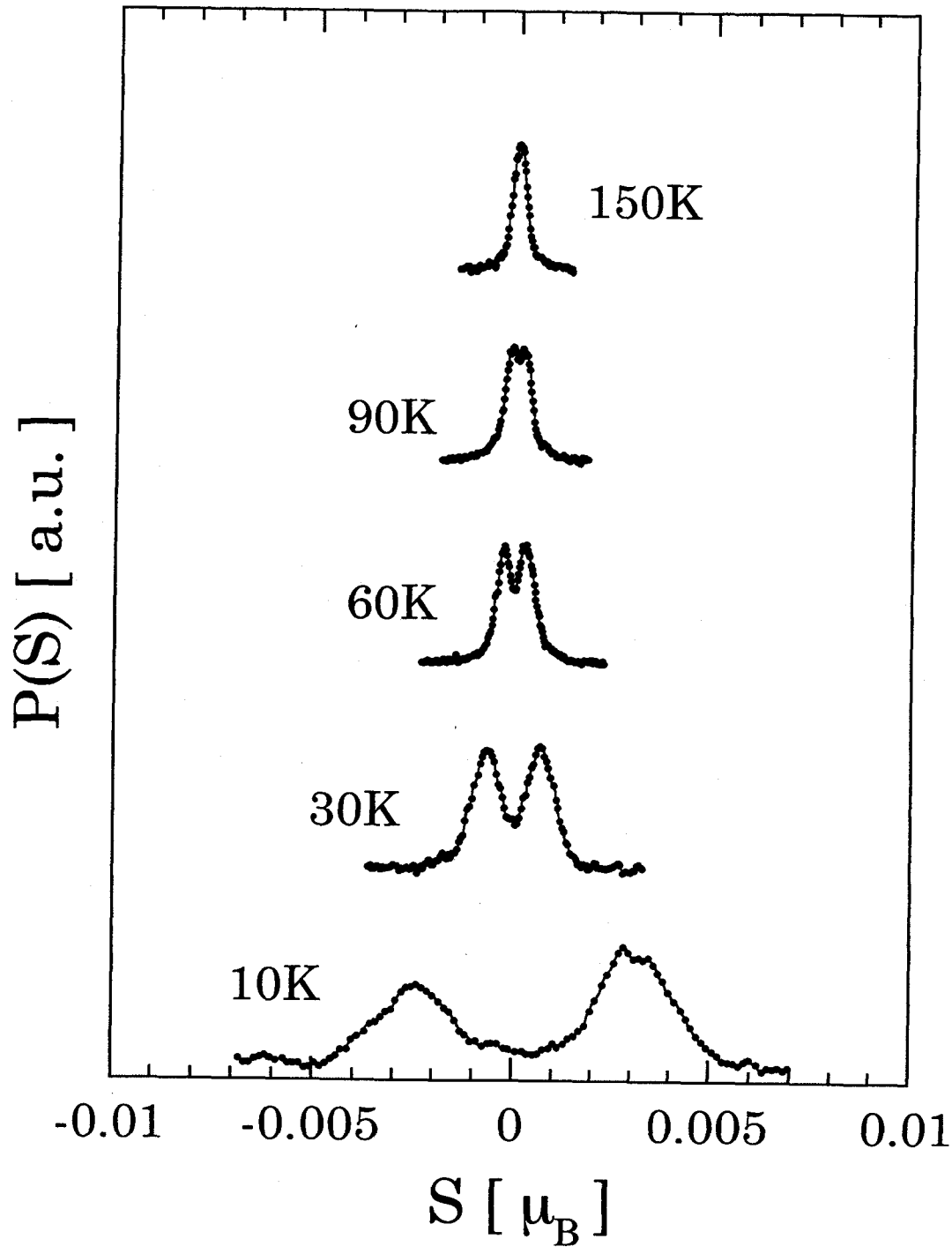

Fig.4.4.4 Temperature variation of the distribution of staggered moments in Sr14-B.

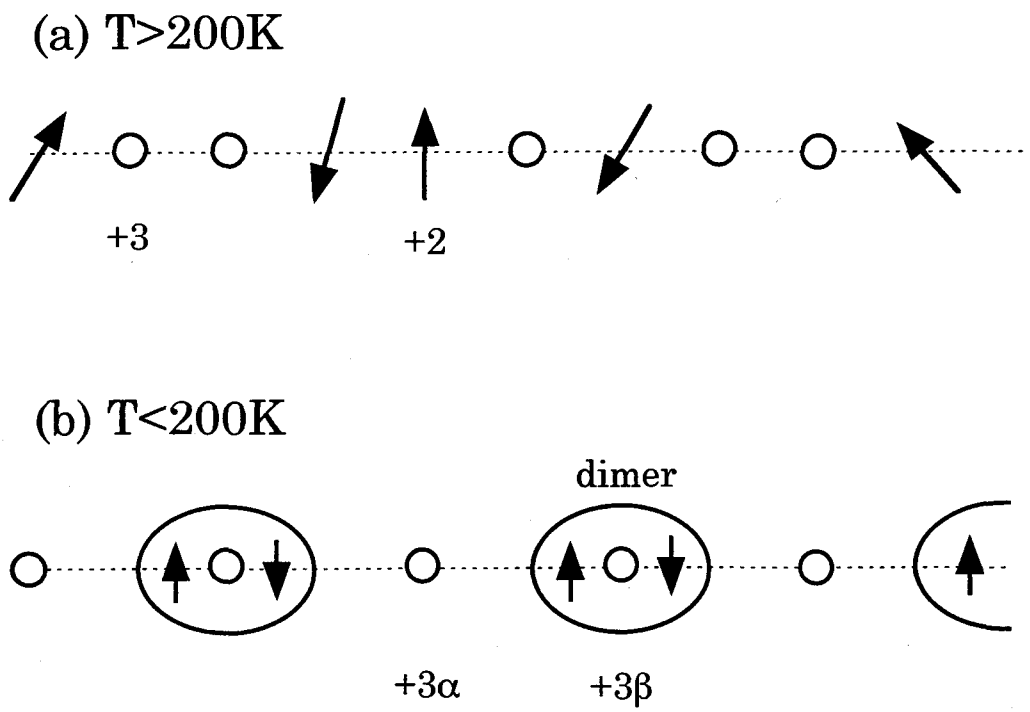

Fig.4.4.5 Dimerization model in CuO_2 chain. (a) T>200K. (b) T<200K.

Chapter 5

SUMMARY

NMR/NQR measurements on hole-doped two-leg ladder systems of $La_{1-x}Sr_xCuO_{2.5}$ and $Sr_{14}Cu_{24}O_{41}$ have clarified the magnetic properties and the effects of the carrier-doping.

Cu NMR experiments have revealed that the ground state of $LaCuO_{2.5}$ is not in the spin liquid state with the spin gap in disagreement with the previous suggestion from the susceptibility measurement. Alternatively, it has been shown that a magnetic ordering takes place below T_N ~110 K as evidenced by the large increase of $1/T_1$ and the divergent behavior of $1/T_2$ leading to the disappearance of the Cu-NMR signal. Furthermore, it has been found that T_N is strongly reduced upon doping and the paramagnetic state is stabilized by substituting Sr for La by 5%. The present NMR experiments have found a contrast of the ground state between the two-leg ladder compounds, $SrCu_2O_3$ and $LaCuO_{2.5}$. The magnetic interaction among the ladders in $LaCuO_{2.5}$, which is not frustrated, has been pointed out to lead to the magnetically ordered state. No signature of superconductivity in the Sr-doped $LaCuO_{2.5}$ compound may be partially responsible for the lack of a spin gap in the parent compound $LaCuO_{2.5}$.

On the other hand, comprehensive Cu NMR/NQR measurements have been performed on the single crystals of $Sr_{14}Cu_{24}O_{41}$ and $Sr_{13.75}Y_{0.25}Cu_{24}O_{41}$, which contain the CuO_2 chain and the Cu_2O_3 two-leg ladder, by discriminating between both Cu sites with Cu NMR/NQR spectra. In these compounds, inherently doped holes play an important role to disturb the quantum coherent in the singlet ground state in the two-leg ladder and to form dimers in the chain. In the two-leg ladder, there exists the spin gap of about 500K which is larger than in $SrCu_2O_3$. It was found that the magnetic field induces a staggered magnetization (SM) in Sr14-B below ~100K. The origin of the SM is suggested to be attributed to unpaired holes. Although the antiferromagnetic long range ordering due to spin defects in the two-leg ladder system has been studied experimentally and theoretically, it has been shown in this study that the SM is induced by unpaired holes. It is suggested that holes do not localize to average out the SM. The long-range magnetic ordering at low temperature is not evident. The SM is reduced due to the spin singlet correlations. The 3D magnetic interaction between the ladder planes may be weak because non magnetic CuO_2 chain layers break off it due to the dimerization and ZR-singlet. NMR/NQR measurements revealed the existence of the spin gap of 100~140K in the CuO_2 chain which had been suggested by the magnetic susceptibility measurement. In the CuO_2 chain, the unique dimerization model, which is consistent with the result of the inelastic neutron scattering measurement, was proposed in this work.

A C K N O W L E D G M E N T

I would like to express sincere thanks to Prof.Kunisuke Asayama and Prof.Yoshio Kitaoka for giving the opportunity to study the low-dimensional quantum spin system, pertinent guidance, enlightening discussion, and warmhearted encouragement through this work.

I would like to express my special thanks to Prof.Zenji Hiroi, Dr.Nariya Kobayashi and Prof.Mikio Takano (Kyoto Univ.) for supplying $La_{1-x}Sr_xCuO_{2.5}$ samples.

I would like to express my special thanks to Dr.Masatomo Uehara, Mr.Takashi Nagata and Prof.Jun Akimitsu (Aoyama Univ.) for supplying $Sr_{14}Cu_{24}O_{41}$ ones.

I would like to express my special thanks to Dr.Masaaki Matsuda and Prof.Ko-ichi Katsumata (RIKEN) for $Sr_{14}Cu_{24}O_{41}$ ones.

I would like to thank to Dr.Guo-qing Zheng and Dr.Kenji Ishida for their useful discussions and helpful supports.

I would like to thank to Dr.Ko-ichi Magishi, Mr.Takeshi Mito and Dr.Shigeki Ohsugi for their useful discussion in this work.

I would like to thank to all the colleagues in Asayama laboratory for their cooperation.

January 1998 Shinji MATSUMOTO